https://doi.org/10.15388/vu.thesis.73
https://orcid.org/0000-0002-8531-9744

VILNIUS UNIVERSITY
CENTER FOR PHYSICAL SCIENCES AND TECHNOLOGY

Mažena
MACKOIT-SINKEVIČIENĖ

Point defects as single-photon emitters in hexagonal boron nitride: theoretical study

DOCTORAL DISSERTATION
Natural sciences
Physics N 002

VILNIUS 2020

This dissertation was written between 2016 and 2020 at the Center for Physical Sciences and Technology. The research was supported by the Research Council of Lithuania.

Scientific supervisor:
Prof. dr. Audrius Alkauskas (Center for Physical Sciences and Technology, Lithuania, Natural Sciences, Physics – N 002).

https://doi.org/10.15388/vu.thesis.73
https://orcid.org/0000-0002-8531-9744

VILNIAUS UNIVERSITETAS
FIZINIŲ IR TECHNOLOGIJOS MOKSLŲ CENTRAS

Mažena
MACKOIT-SINKEVIČIENĖ

Taškiniai defektai kaip pavienių fotonų šaltiniai heksagoniniame boro nitride: teorinis tyrimas

DAKTARO DISERTACIJA
Gamtos mokslai
Fizika N 002

VILNIUS 2020

Disertacija rengta 2016 - 2020 metais Fizinių ir technologijos mokslų centre. Mokslinius tyrimus rėmė Lietuvos mokslo taryba.

Mokslinis vadovas:
Prof. dr. Audrius Alkauskas (Fizinių ir technologijos mokslų centras, gamtos mokslai, fizika – N 002).

Acknowledgment

Every morning at the valley of Sunrise,
Eternally young and tireless
curiosity of scientists is being revived.
Then the light from the star clusters
with the highest luminosity
shines directly on their Beautiful Minds.
Perennially keeps telling them the same story
that when scientific path gets tough
the desire in seeking right answers
over and over, indeed has no limits,
because there is never enough.

I would like to express my deepest gratitude, first and foremost, to my *scientific advisor*, Professor Audrius Alkauskas, for accepting me into his group Puntukas (from August 2015 as my master advisor and from October 2016 as my PhD advisor) and teaching me so much about materials physics, computational quantum-mechanical modeling and elegant scientific writing. I am thankful for being given an opportunity to participate in M-ERA.NET project *Metrology at the Nanoscale with Diamonds*. He believed in me and made these years an extraordinary journey through the unexplored vastness of complex hexagonal boron nitride physical problems, and supported me all this time.

Immense gratitude goes to Professor Gintaras Valušis, who brought me to the Center for Physical Sciences and Technology, supported and encouraged me to attend international conferences and workshops.

I am grateful for the opportunity I had to collaborate and discuss research results with Professor Chris G. Van de Walle, dr. Darshana Wickramaratne, dr. Leigh Weston (University of California, Santa Barbara, USA), dr. Marcus William Doherty and Prithvi Reddy (Australian National University, Australia). Dr. Darshana Wickramaratne helped me out with various questions.

My very first research paper in building bridges between theory and experiment was published together with inspiring scientists Professor Carlos A. Meriles and Professor Vinod Menon (City University of New York, USA). I am also thankful to Professor Algirdas Matulis for his kind assistance with the electrostatics problem.

I would like to thank dr. Marek Maciaszek for numerous fruitful discussions and a marvelous collaboration during our joint adventure with carbon impurities. The *ultraviolet puzzle* was solved together.

I would also like to thank dr. Vytautas Karpus and dr. Tadas Malinauskas for their feedback during the dissertation process and for their help to improve this Thesis.

I would also like to thank *my scientific brother and dear friend* PhD student Lukas Razinkovas for the excellent collaborations in several projects, for great ideas, and never-ending scientific discussions in the Electronic Structure Theory laboratory since the beginning of my scientific career. I also wish to thank the other members of *Puntukas family* - Vytautas Žalandauskas and Rokas Silkinis, with whom I have worked together during my time as a PhD student.

Great appreciation goes to dr. Ramūnas Aleksiejūnas for helping me further professional development and *fulfill my academic dream.* Over three years, I had a unique opportunity to work as a lecturer at Vilnius University, Faculty of Physics. I am also thankful to all of my students for asking hard questions and testing the limits of my knowledge.

Through all these years, thanks to the European Physical Society and EPS Young Minds Project, I had a powerful tool to help with the organization of many important scientific events, seminars, and international conferences in Sunrise Valley. I am grateful for the opportunity to be in the organizing committee of "Sauletekis semiconductor physics seminars", "Open Readings" conference, "Controlling quantum matter" Humboldt Kolleg, "Lasers: Science and Technology" conference and "Lithuanian National Conference of Physics".

Lithuanian Physical Society gave me an opportunity to visit scientific conferences in Dresden and Cracow. Karl Mey Scholarship of the German Physical Society allowed me to attend the DPG Spring meeting in Dresden, Germany, which was my first scientific conference abroad. The Research Council of Lithuania was also very generous in awarding me travel scholarships that enabled me to attend a number of conferences throughout my PhD years, for which I am very grateful.

I owe a great debt of gratitude to the many people from the Center for Physical Sciences and Technology. A special thanks to the members of the THz Atelier team: dr. Linas Minkevičius, dr. Rimvydas Venckevičius, dr. Vytautas Jakštas, Domas Jokubauskis, dr. Mindaugas Karaliūnas, dr. Ignas Grigelionis, dr. Liudvikas Subačius, and Rusnė Povilauskienė for their advice, support and many informal discussions during my PhD path.

For my *dear friends* dr. Nail Garejev, dr. Andrius Gelžinis, dr. Akvilė Zabiliūtė-Karaliūnė, dr. Julius Ruseckas, PhD student Monika Kirsnytė, dr. Ieva Žičkienė, dr. Kristina Plauškaitė-Šukienė, Monika Venčkauskaitė and Greta Vyšniauskienė, Živilė Razinkovienė.

For my *dear colleagues* prof. dr. Gediminas Juzeliūnas, dr. Vytautas Butkus, doc. Renata Butkutė, dr. Renata Karpič, dr. Voitech Stankevič, dr. Rasuolė Lukošė, dr. Simona Strazdaitė, PhD student Mantas Račiūnas, Linas Galkauskas, inspiring dr. Linas Vilčiauskas and dr. Shannon Stauffer, Kotryna Šiškauskaitė, PhD student Jonas Berzinš.

On the personal side, I would like to acknowledge my family, mother Janina and father Tadeuš, my grandmother Stanislava and my one and only twin sister, Agnieška, for all of their support over the past 29 years, great encouragement writing this Thesis, they were always there for me.

Finally, last but not least, my *lovely husband* Jurgis Sinkevičius. He taught me to never stop learning and asking questions. I would mostly like to acknowledge him for tireless support, patience, and unprecedented Love for Me and STEM sciences in general.

Contents

List of abbreviations

APD	avalanche photon diode
ADF	annular dark field imaging
B_i	boron interstitial
B_N	boron antisite
BZ	Brillouin zone
C_B	carbon substitution at boron site
CBM	conduction-band minimum
CC	configurational coordinate diagram
C_BC_N	carbon dimer
$C_B - V_N$	nitrogen vacancy-carbon complex
CDFT	constrained density functional theory
C_i	carbon interstitial
CL	cathodoluminescence
C_N	carbon substitution at nitrogen site
$C_N - V_B$	boron vacancy-carbon complex
2D	two-dimensional
DAP	donor-acceptor pair
DBs	dangling bonds
DFT	density functional theory
DW	Debye-Waller factor
FRET	Förster resonant energy transfer
GGA	generalized gradient approximation
hBN	hexagonal boron nitride
HBT	Hanbury Brown-Twiss interferometer
HF	Hartree-Fock
HK	Hohenberg-Kohn
HS	high-spin state
HSE	screened hybrid functional of Heyd, Scuseria and Ernzerhof
ISC	inter-system crossing
KS	Kohn-Sham
LDA	local density approximation
LS	low-spin state
N_B	nitrogen antisite
N_i	nitrogen interstitial

O_B	oxygen substitution at boron site
O_i	oxygen interstitial
O_N	oxygen substitution at nitrogen site
PAW	projector augmented wave method
PSPW	pseudopotential plane-wave method
PW	plane-wave method
PBE	generalized gradient approximation of Perdew, Burke and Ernzerhof
PL	photoluminescence
PLE	photoluminescence excitation spectroscopy
QD(s)	quantum dot(s)
RT	room-temperature
ΔSCF	delta self-consistent field approximation
SPE(s)	single-photon emitter(s)
STEM	scanning transmission electron microscope
TEM	transmission electron microscopy
VASP	Vienna *ab-initio* simulation package
V_B	boron vacancy
$V_B - H$	boron vacancy-hydrogen complex
VBM	valence-band maximum
$V_B - O_N$	boron vacancy-oxygen complex
$V_B - V_N$	divacancy
V_N	nitrogen vacancy
XANES	x-ray absorption near-edge structure
ZPL	zero phonon line

Introduction

Future light-based quantum technologies will depend on generation and manipulation of single photons, thus any quantum device will contain one crucial component within – single-photon emitter (SPE). So far, among the frontrunners are solid-state SPEs [1], and they are expected to play an essential role in a plethora of *quantum tasks* like enhanced precision measurements and sub-diffraction imaging systems [2], ultrasensitive sensing [3] or optical quantum computing [4] – all these applications have already become quantum roadmap targets for the next decade. A good example of quantum technologies is quantum cryptography [5] or, more precisely, quantum key distribution, that has already reached commercial availability [6]. Furthermore, the importance of the mentioned technologies motivated the European Commission to launch European Quantum Technologies Flagship [7]. This large-scale, long-term research initiative will foster the development of a competitive quantum industry, making the results of quantum research available for commercial applications and disruptive technologies.

One of the most studied solid-state SPE systems are atom-like defects providing quantum states that can be addressed via optical excitation [1]. A starting point in the evolution of solid-state SPEs was the detection of the negatively charged nitrogen-vacancy center in diamond by Jörg Wrachtrup and colleagues [8]. However, despite unique properties of this color center [1,9], cost and the difficulty of integrating diamond components into devices using traditional lithographic approaches motivated the exploration of defect states in other material systems as well [10]. As such, several materials hosting fluorescent defects have been explored, and, with time, the playground of solid-state SPEs has expanded beyond wide-bandgap semiconductors, such as zinc oxide, silicon carbide, gallium nitride, and aluminum nitride [11–14], to include two-dimensional (2D) materials that offer structural *openness* [1, 15, 16]. However, each technical solution has different pros and cons.

Hexagonal boron nitride (hBN) stands out as one of the most alluring 2D materials because of its uniquely wide bandgap of 6 eV and exceptionally excellent chemical and thermal stability [17, 18]. This insulating analog of graphite,

due to the excellent lattice match, is an ideal substrate for graphene and an essential building block in van der Waals heterostructures [19,20]. The growth of high-quality hBN crystals also triggered an increasing interest in deep ultraviolet applications because of the bright luminescent emission of hBN single crystals [17,21,22]. The recent discovery that hBN can host bright and stable SPEs has sparked interest in this material as another compelling host for SPEs [23]. In the past few years, the activity in this field has flourished, and SPEs have been discovered in monolayer, multi-layer, as well as bulk-grown hBN, and synthesized by a variety of methods [24–30]. SPEs in hBN come into play as an attractive system due to robust, narrow-linewidth, bright, photostable, and indistinguishable single-photon sources operating at room temperature and above [31]. Ultimately, the optically detected magnetic resonance response from SPEs in hBN was obtained, indicating that there are spin-dependent transitions [32]. All properties of SPEs in hBN mentioned above, in combination, can become a rich platform to support the 2^{nd} quantum revolution that relies on manipulating and reading quantum states [33].

So, what exactly is the *microscopic origin* of the SPEs in hBN? Despite active investigations, there is a considerable controversy in the literature and prior observations. Even though theoretical calculations have given rise to several candidate defect structures [34–38], direct comparisons with experiments remain inconclusive. The atomic structures of the point defects, to which light emission in hBN has been attributed, is still under dispute, and the effect of the annealing on optical activation of SPEs, that emit light in the visible range, is unresolved. Thus more in-depth analysis and further investigations to shine a light on the origin of SPEs are necessary.

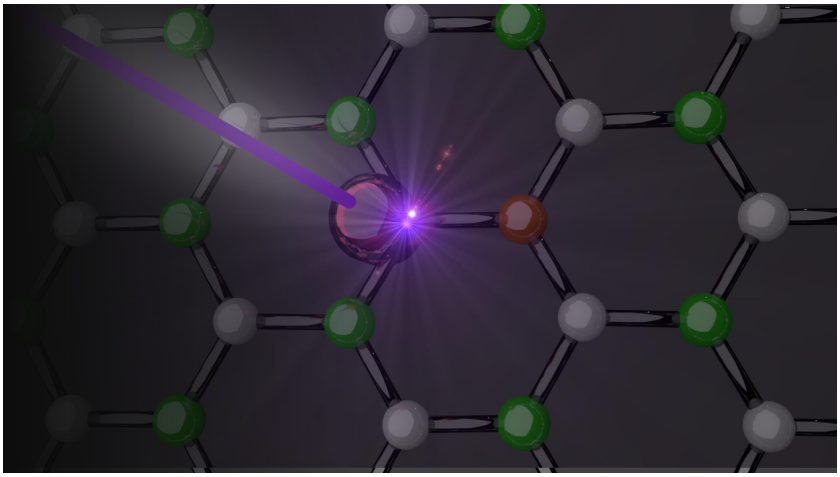

Illustration of highly efficient ultraviolet SPE in hBN that was investigated in this Thesis.

Fortunately, as it turns out, direct identification and characterization of defects can sometimes elude experimental efforts. First-principles methods have emerged as a powerful approach to complement experiments and gain valuable insights about materials at the atomic level. In particular, the density functional theory (DFT) has become an integral part of materials research, and is practiced by a considerable and ever-growing number of research groups around the world. Furthermore, in recent years, advanced calculations based on hybrid DFT have provided essential insights into the defect properties of III-nitrides [39–41]. Thus similar calculations open up a path to obtain more detailed insights into the defect physics.

Goal of the Thesis

The main goal of this Thesis is to uncover the physics and the role of point defects in hBN, in particular for the observed single-photon emission, by performing first-principles calculations.

Tasks of the Thesis

In order to reach the goal of this Thesis, the following tasks were set:

1. Disclose the role of point defects and most common impurities in hBN by providing accurate information about their structural, electronic, thermodynamic, and kinetic properties.
2. Ivestigate optical properties of boron vacancy complexes with oxygen and hydrogen in hBN.
3. Develop a quenching model of 2 eV single-photon emission in hBN.
4. Assign the origin of the defect responsible for the observed single-photon emission in the ultraviolet spectral range in hBN by deducing defect-phonon coupling, the radiative lifetime of internal optical transitions, quantum efficiency, and other key parameters.

Novelty and importance of the work

This Thesis employs extensive hybrid DFT calculations in order to produce accurate results for the characterization of point defects as SPEs in hBN. Results obtained in this Thesis are essential for several reasons.

1. A significant step forward in the study of hBN defects was provided by giving a broad and comprehensive picture of the defect chemistry in hBN: uncovered dominant defect structures and their physical properties.

2. The author of this Thesis ensured a correct treatment of defect physics, and thereby illustrated ability to predict and assign microscopic identity of SPEs in hBN, using a purely first-principles approach.

3. Physical model for quenching of 2 eV single-photon emission in hBN was proposed.

4. The author of this Thesis unpretentiously believes that the study covered herein has also made its small contribution towards a more in-depth understanding of ultraviolet emission in hBN by giving convincing explanations for obtained results.

Key statements for defence

1. Impurities rather than native defects dominate the defect chemistry of hBN. Due to higher formation energies and migration barriers, bare vacancy defects could be present in nonequilibrium conditions only. The common attribution of the 4.1 eV luminescence to C_N defect is ruled out.

2. Quenching of 2 eV single-photon emission can be explained through Förster resonant energy transfer from red SPEs to boron vacancy complexes with hydrogen and oxygen. The proposed 2 eV SPE luminescence quenching model can be expanded for two perfectly isolated nitrogen dangling bond systems in hBN.

3. Ultraviolet single-photon emission in hBN at 4.1 eV originates in carbon dimer defect. The internal optical transition occurs between two localized p_z-type defect states, with a short radiative lifetime. The calculated key parameters for optical transition are in excellent agreement with experimental data.

Contribution of the author

The author of the Thesis performed theoretical calculations, analyzed the obtained data and prepared publications I, II, III and IV together with co-authors. The author performed all first-principles calculations for this Thesis at the High Performance Computing Center "HPC Saulėtekis" in the Faculty of Physics, Vilnius University. Dr. L. Weston and dr. D. Wickramaratne together with the author investigated electronic, thermodynamic, and kinetic properties of native point defects and impurities in hBN. The author has contributed to the investigation of electronic and optical properties of vacancy-impurity complexes in hBN and performed some independent calculations for defect energetic, electronic structure, and migration properties. The author has performed all of

the calculations and theoretical work according to boron vacancy complexes in hBN. The author wrote the manuscript related to the second paper II, i.e., investigation of SPE luminescence quenching through Förster resonant energy transfer. The author proposed to extend the 2 eV SPE luminescence quenching model for two perfectly isolated nitrogen dangling bond systems in hBN. Group of Prof. dr. C. A. Meriles performed all the measurements in order to investigate the photo-induced modification of SPEs in hBN in paper III. The author and dr. M. Maciaszek have equally contributed performing the first-principles calculations of the carbon dimer in hBN. Additionally, the author calculated dipole moment, radiative lifetime for the carbon dimer in hBN, and prepared manuscript of the IV paper. The author prepared an illustration that appeared on the cover of Applied Physics Letters journal.

Approbation of the research results

This section presents the lists of papers and conferences related to the Thesis. In the doctoral Thesis, the following papers are referred to by Roman numbers.

List of papers related to the Thesis

I L. Weston. D. Wickramaratne, **M. Mackoit**, A. Alkauskas, C. G. Van de Walle, Native point defects and impurities in hexagonal boron nitride, Physical Review B **97**, 214104 (2018).

II **M. Mackoit-Sinkevičienė**, L. Razinkovas, A. Alkauskas, The role of boron vacancy complexes in hexagonal boron nitride, in preparation (2020).

III Z. Shotan, H. Jayakumar, C. R. Considine, **M. Mackoit**, H. Fedder, J. Wrachtrup, A. Alkauskas, M. W. Doherty, V. M. Menon, and C. A. Meriles, Photo-induced modification of single-photon emitters in hexagonal boron nitride, ACS Photonics **3**, 2490-2496 (2016).

IV **M. Mackoit-Sinkevičienė**, M. Maciaszek, C. G. Van de Walle, A. Alkauskas, Carbon dimer defect as a source of the 4.1 eV luminescence in hexagonal boron nitride, Applied Physics Letters **115**, 212101 (2019). Graphic of work printed on the cover of APL journal.

List of papers unrelated to the Thesis

1 L. Skuja, K. Smits, A. Trukhin, F. Gahbauer, R. Ferber, M. Auzins, L. Busaite, L. Razinkovas, **M. Mackoit-Sinkevičienė**, A. Alkauskas, Dynamics

of singlet oxygen molecule trapped in silica glass, studied by luminescence polarization anisotropy and density functional theory, The Journal of Physical Chemistry C **124**, 7244 (2020).

List of conference contributions related to the Thesis

1 **M. Mackoit-Sinkevičienė** (presented), M. Maciaszek, C. G. Van de Walle, A. Alkauskas, Anglies dimeras heksagoniniame boro nitride kaip 4 eV liuminescencijos šaltinis, VIII-oji Fizinių ir Technologijos Mokslų centro doktorantų ir jaunųjų mokslininkų konferencija, Fizinių ir technologijos mokslų centras, 2019-10-24, Vilnius, Lithuania. Oral presentation.

2 **M. Mackoit-Sinkevičienė** (presented), M. Maciaszek, C. G. Van de Walle, A. Alkauskas, Anglies dimeras heksagoniniame boro nitride kaip 4 eV liuminescencijos šaltinis, 43-oji Lietuvos Nacionalinė Fizikos konferencija, 2019-10-05, Kaunas, Lithuania. Oral presentation.

3 **M. Mackoit-Sinkevičienė** (presented), M. Maciaszek, C. G. Van de Walle, A. Alkauskas, Carbon dimer defect as a source of 4.1 eV luminescence in hexagonal boron nitride, Lithuania-Poland Workshop on Physics and Technology, 2019-09-27, FTMC, Lithuania. Oral presentation.

4 **M. Mackoit-Sinkevičienė** (presented), M. Maciaszek, C. G. Van de Walle, A. Alkauskas, Carbon dimer defect as a source of 4.1 eV luminescence in hexagonal boron nitride, Conference XLV Meeting of Polish Physicists and IPSEC XII, 2019-09-13, Cracow, Poland. Poster presentation.

5 M. Maciaszek (presented), **M. Mackoit-Sinkevičienė**, C. G. Van de Walle, A. Alkauskas, Carbon dimer defect as the origin of the 4 eV luminescence in hexagonal boron nitride, ICDS 30, 2019-07-21, Washington, USA. Oral presentation.

6 C. G. Van de Walle (presented), L. Weston, D. Wickramaratne, M. E. Turiansky, **M. Mackoit**, A. Alkauskas, Point defects, impurities, and single-photon emitters in hexagonal boron nitride, APS March Meeting 2019, 2019-03-04, Boston, USA. Oral presentation.

7 **M. Mackoit-Sinkevičienė** (presented), L. Weston. D. Wickramaratne, C. G. Van de Walle, A. Alkauskas, Taškiniai defektai boro nitride kaip pavienių fotonų šaltinis, VII-oji Fizinių ir Technologijos Mokslų centro doktorantų ir jaunųjų mokslininkų konferencija, 2018-10-17, FTMC, Lithuania, Oral presentation.

8 **M. Mackoit** (presented), L. Weston, D. Wickramaratne, L. Razinkovas, M. W. Doherty, C. G. Van de Walle, A. Alkauskas, Optical properties of boron vacancy-related defects in hexagonal boron nitride, International conference

Advanced Properties and Processes in Optoelectronic Materials and Systems APROPOS-16, 2018-10-10, Vilnius, Lithuania. Oral presentation.

9 **M. Mackoit** (presented), L. Weston, D. Wickramaratne, L. Razinkovas, M. W. Doherty, C. G. Van de Walle, A. Alkauskas, Optical properties of boron vacancy-related defects in hexagonal boron nitride, E-MRS Fall Meeting, 2018-09-16, Warsaw, Poland. Oral presentation.

10 **M. Mackoit** (presented), L. Weston, D. Wickramaratne, C. G. Van de Walle, A. Alkauskas, Native point defects and impurities in hBN, Humboldt Kolleg Controlling quantum matter: From ultracold atoms to solids, 2018-07-29, Vilnius, Lithuania. Poster presentation.

11 **M. Mackoit** (presented), L. Weston, D. Wickramaratne, M. W. Doherty, C. G. Van de Walle, A. Alkauskas, Optical properties of single photon sources in hBN, 7th European Physical Society Young Minds EPS-YM Meeting, Czech Technical University, 2018-05-03, Prague, Czech Republic. Oral presentation.

12 **M. Mackoit** (presented), L. Weston, D. Wickramaratne, A. Alkauskas, C. G. Van de Walle, Native point defects in hexagonal boron nitride, 61st Scientific Conference of Physics and Natural Sciences Open Readings, 2018-03-17, Vilnius, Lithuania. Oral presentation.

13 **M. Mackoit** (presented), L. Weston, D. Wickramaratne, M. W. Doherty, C. G. Van de Walle, A. Alkauskas, Optical properties of point defects in hBN, Infobalt contest for Young Scientists, 2018-02-22, Vilnius, Lithuania. Oral presentation.

14 **M. Mackoit** (presented), L. Weston, D. Wickramaratne, M. W. Doherty, C. G. Van de Walle, A. Alkauskas, Point defects as single photon sources in h-BN, Lithuanian Academy of Sciences 8th Conference of Young Scientists Physical and Technological Sciences Interdisciplinary Research, Lithuanian Academy of Sciences, 2018-02-08, Vilnius, Lithuania. Oral presentation.

15 **M. Mackoit** (presented), Photo-induced modification of single-photon emitters in hexagonal boron nitride, Project Metrology at the Nanoscale with Diamonds (MyND) Workshop, 2017-12-16, Ryga, Latvia. Oral presentation.

16 **M. Mackoit** (presented), A. Alkauskas, L. Weston, D. Wickramaratne, M. W. Doherty, C. G. Van de Walle, Boro vakansijų ir boro vakansijų kompleksų hBN optinės savybės, 42-oji Lietuvos Nacionalinė Fizikos konferencija, 2017-10-04, FTMC, Vilnius, Lithuania. Oral presentation.

17 **M. Mackoit** (presented), L. Weston, D. Wickramaratne, A. Alkauskas, C. G. Van de Walle, Native point defects and impurities in hexagonal boron nitride, E-MRS Fall Meeting, 2017-09-21, Warsaw, Poland. Oral presentation.

18 **M. Mackoit** (presented), A. Alkauskas, Optical properties of boron vacancies and boron vacancy complexes in hexagonal boron nitride, Deutsche Physikalische Gesellschaft DPG conference, Spring Meeting of the Condensed Matter Section, 2017-03-20, Dresden, Germany. Oral presentation.

19 H. Jayakumar (presented), Z. Shotan, C. Considine, **M. Mackoit**, H. Fedder, J. Wrachtrup, A. Alkauskas, M. Doherty, V. Menon, C. Meriles, Optical spectroscopy and photo modification of individual single-photon emitters in hexagonal boron nitride, APS March Meeting 2017, 2017-03-13, New Orlean, Louisiana, USA. Oral presentation.

20 **M. Mackoit** (presented), A. Alkauskas, Optical properties of boron vacancies and boron vacancy complexes in hexagonal boron nitride, Open Readings 2017, 2017-03-14, FTMC, Lithuania. Oral presentation.

21 **M. Mackoit** (presented), Z. Shotan, H. Yayakumar, C. R. Considine, H. Fedder, J. Wrachtrup, A. Alkauskas, M. W. Doherty, V. Menon, C. A. Meriles, Šviesos indukuota pavienių fotonų šaltinių modifikacija, Lithuanian Academy of Sciences 7th Conference of Young Scientists Physical and Technological Sciences Interdisciplinary Research, Lithuanian Academy of Sciences, 2017-02-09, Vilnius, Lithuania. Oral presentation.

22 **M. Mackoit** (presented), A. Alkauskas Šviesos indukuota pavienių fotonų šaltinių modifikacija hBN, VI-oji Fizinių ir Technologijos Mokslų centro doktorantų ir jaunųjų mokslininkų konferencija, Fizinių ir technologijos mokslų centras, 2016-10-26, FTMC, Lithuania. Oral presentation.

Curriculum Vitae

Name: Mažena
Surname: Mackoit-Sinkevičienė
Date of birth: 1991-05-22, Vilnius, Lithuania
E-mail: mazena.mackoit@ftmc.lt

Education

2003 – 2010	Juzefo Ignacijaus Kraševskio Middle school, Vilnius *Certificate with Honors.*
2010 – 2014	Vilnius University, Faculty of Physics Bachelor degree, *Cum Laude.*
2014 – 2016	Vilnius University, Faculty of Physics Master degree, *Magna Cum Laude.*
2016 – 2020	Center for Physical Sciences and Technology Ph.D. studies.

Work experience

2018 – now	Solid State Physics course Assistant/Lecturer, Vilnius university, Faculty of Physics
2016 – now	Junior Researcher, Electronic Structure Theory Group, FTMC
2015 – 2016	Engineer, Department of Optoelectronics, FTMC
2012 – 2015	Technician, Vilnius University, Institute of Applied Research

Awards

2020	Scholarship of the Research Council of Lithuania
2019	Scholarship of the Research Council of Lithuania
2018	Talent of the year Award, Faculty of Physics
2018	Graduate Student Award, European Materials Research Society
2018	Scholarship of the Research Council of Lithuania
2018	3rd place and Young Scientist's award, Infobalt Scholarship
2018	Young Scientist's Award, Lithuanian Academy of Sciences
2017	European Physical Society Best Activity Award for leading EPS YM
2017	International Dr. Karl Mey Scholarship
2016	Vilnius University Rector's acknowledgement

Power of Walter Kohn's education

Undoubtedly power of Walter Kohn's education
was a new many-body problem's approach creation,
which reduced amount of variables and problem's size,
it is thus unsurprising that Kohn received for this a Nobel Prize[1].
Two Hohenberg-Kohn theorems are at its heart,
telling that electron density and energy can be mapped one-to-one.
Proposed method's prediction of structure properties ability
revolutionized experimental field and has proved its utility.
Density functional theory presents an incredible success story,
through obtained accuracy and low computational cost
it has earned its full glory.

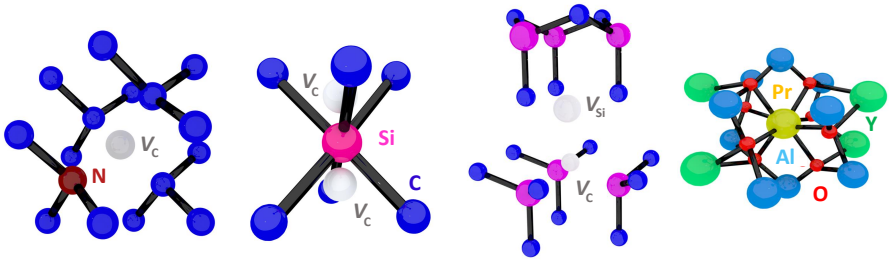

Illustration of some prominent quantum point defects in diamond, silicon carbide and complex oxides.

[1]Walter Kohn, the founding father of DFT, received a Nobel Prize in Chemistry in 1998. DFT is currently one of the most powerful tools for studying defects properties in various materials.

Chapter 1

Theoretical Background

When a theoretical physicist wants to model a material — be it a quantum dot or a slab of semiconductor — he often uses software to calculate the behavior of electrons within the material. Most of the software is built on density functional theory (DFT), one of the most popular approaches in the physical and chemical sciences [42, 43]. DFT methodology is especially essential for the discovery of novel quantum point defects in various materials. Furthermore, obtained results allow us to calculate parameters that can be used in modeling various phenomena such as defect formation energies or luminescence lineshapes, etc. [44, 45]. The first 1.1, and second 1.2 parts of this chapter cover the basic theoretical concepts that build the foundation of density functional theory. Starting from the time-independent Schrödinger equation, the relevant formalism for Hartree-Fock method and DFT used throughout this work will be reviewed. Furthermore, the theoretical background for periodic systems in the context of exact exchange will be discussed. In the 1.3 part, we will focus on the practical implementation of DFT for electronic structure calculations of solids.

1.1. Many-particle Schrödinger equation

Ninety-four years have already passed since Erwin Schrödinger formulated the fundamental equation of quantum mechanics [46], the solution of which is the key to determine any observable physical quantity of the system. All information we could possibly have about a given system is contained in the system's wave function. An *ab-initio* study of condensed matter aims to solve the many-particle Schrödinger equation for the system being studied, for example, a perfect hBN crystal. The time-independent, nonrelativistic many-particle

Schrödinger equation is given by

$$\hat{H}\Psi(\mathbf{r},\mathbf{R}) = E\Psi(\mathbf{r},\ \mathbf{R}). \tag{1.1}$$

Here $\mathbf{r}$ are the coordinates of electrons and $\mathbf{R}$ are the coordinates of nuclei. The many-particle Hamiltonian consists of the five terms

$$\hat{H} = \hat{T}_e + \hat{T}_\alpha + \hat{V}_{\alpha e} + \hat{V}_{\alpha\alpha} + \hat{V}_{ee}. \tag{1.2}$$

The first two terms, $\hat{T}_e$ and $\hat{T}_\alpha$ are the electronic and nuclei kinetic energy, respectively. The other three operators describe the nuclear-electron $\hat{V}_{\alpha e}$, nuclear-nuclear $\hat{V}_{\alpha\alpha}$ and electron-electron $\hat{V}_{ee}$ interactions.

This electron-nuclear many-particle problem is one of the most intractable problems of quantum physics. The main obstacle is that the motions of the electrons in atoms correlate because of the strong Coulomb repulsion between them. This second-order partial differential equation 1.1 is extremely difficult to solve analytically in all but the simplest of cases considering that the computational resources required to solve it scale exponentially with both the number of electronic coordinates $3n$ and number of nuclear $3N$ coordinates in the system. To understand the problem's difficulty, consider that 1 gram of any material contains on the order of 10^{23} electrons[2]. Solving the Schrödinger equation for this system using a computer would require approximately 1 billion petabytes of computing space to represent the $3n$ coordinates of each electron [42]. Nonetheless, during decades of struggling, many powerful methods for solving Schrödinger's equation have been developed, and this problem has been solved numerically for a wide range of atoms and molecules [47]. We will next summarize some widely used approximations that computationally simplify this problem.

1.1.1. The Born-Oppenheimer approximation

The Born-Oppenheimer approximation takes into account the significant difference between electronic and nuclear masses, and correspondingly the time scales of their motion, i.e., the nuclei can be assumed to be *stationary*. This enables simplification of the Hamiltonian operator $\hat{H}$ (in equation 1.2) by decoupling the ionic and electronic motion, so that the two decoupled systems can be solved more efficiently. This approximation is valid as long as the ratio of vibrational to electronic energies is small [48].

For the first step the nuclear kinetic energy operator $\hat{T}_\alpha$ is neglected and

[2]For instance, one gram of hexagonal boron nitride contains $3.99 \cdot 10^{23}$ electrons. However, in *ab-initio* calculations, the macroscopic quantity of hBN can be well approximated by a primitive unit cell containing only 4 atoms, i.e., 16 electrons. The resulting perfect crystal is an excellent approximation of a real bulk hBN; the electronic band structure of bulk hBN in chapter 3.3.1 was calculated with akin primitive cell.

nuclear-nuclear repulsion $\hat{V}_{\alpha\alpha}$ is reduced to a constant, which can be neglected from the electronic part of Hamiltonian

$$\hat{H}_e = \hat{T}_e + \hat{V}_{\alpha e} + \hat{V}_{ee}. \tag{1.3}$$

The electronic Schrödinger equation is solved approximately with a fixed nuclear geometry. Next, the so-called potential energy surface (or *adiabatic surface*) is obtained by varying the nuclei positions $\boldsymbol{R}$. In the second step, the nuclear kinetic energy $\hat{T}_\alpha$ is reintroduced, and the Schrödinger equation for the nuclear motion is solved. The nuclear coordinates still enter the electronic Schrödinger equation as an external potential in which the electrons move, but not as independent variables. This approximation is not feasible for any realistic material and can only analytically be solved for the simplest cases. Therefore, further approximations are needed to take advantage of numerical methods.

1.1.2. The Hartree-Fock method

The Hartree–Fock (HF) method (or *self-consistent field method*) was the first practically useful approach to solve the many-particle problem [49] [50]. In this method, the many-particle wave function of the system can be approximated by a single Slater determinant, that is, an antisymmetrized product of single-particle wave functions

$$\Psi_{\mathrm{HF}} = \frac{1}{\sqrt{N!}} \begin{vmatrix} \psi_1(x_1) & \psi_2(x_2) & ... & \psi_1(x_N) \\ \psi_2(x_1) & \psi_2(x_2) & ... & \psi_2(x_N) \\ ... & ... & ... & ... \\ \psi_N(x_1) & \psi_N(x_2) & ... & \psi_N(x_N) \end{vmatrix}. \tag{1.4}$$

Here each single particle N wave function is the product of a spatial $\varphi(r)$ and spin $\eta(\sigma)$ component, $\psi_i(x_i) = \varphi_i(r_i)\eta_i(\sigma_i)$. This many-particle wave function ansatz satisfies the Pauli exclusion principle.

In HF method, a series of single-particle Schrödinger equations are solved in which electron-electron interaction is determined in an average way i.e., every particle is exposed to the mean field created by other particles. The expectation value of the energy is the sum of the energies of the one-electron HF orbitals

$$E_{\mathrm{HF}} = \langle \Psi_{\mathrm{HF}} | \hat{H} | \Psi_{\mathrm{HF}} \rangle = \sum_{i=1}^{N} E_i + \frac{1}{2} \sum_{i=1}^{N} \sum_{j=1}^{N} (C_{ij} - K_{ij}), \tag{1.5}$$

where

$$E_i = \langle \psi_i | h | \psi_i \rangle, \quad C_{ij} = \langle \psi_i \psi_j | V_{\mathrm{int}} | \psi_i \psi_j \rangle, \quad K_{ij} = \langle \psi_i \psi_j | V_{\mathrm{int}} | \psi_j \psi_i \rangle. \tag{1.6}$$

The subscripts i and j denote the summation over orbitals, $V_{\text{int}} = \frac{e^2}{r_{ij}}$. The first term E_i is the *one electron* contribution to the total energy, containing electron's kinetic energy and potential energy due to the electron-nuclear interaction. The second term C_{ij} is usually called the Coulomb integral and the third term K_{ij} is called the exchange integral. These integrals describe *two electrons* contribution of electron-electron interaction. The Coulomb integral contains a spurious self-interaction error that is canceled by the exchange integral when $C_{ii} = K_{ii}$. However, in general, to describe all possible orbital occupations (i.e., including excited states), an infinite number of weighted Slater determinants is needed. For this reason, the HF method only provides an approximation to electron-electron interaction and it neglects electron correlation.

There are no analytic solutions for many-electron systems, therefore the problem is solved numerically by applying the variational method

$$E_0 \leq \frac{\langle \Psi_{\text{HF}} | \hat{H} | \Psi_{\text{HF}} \rangle}{\langle \Psi_{\text{HF}} | \Psi_{\text{HF}} \rangle}. \tag{1.7}$$

The HF method determines the set of spin orbitals which minimize the energy. One-electron orbitals are used to make an initial guess, that is subsequently employed to work out the HF equations. Based on one-electron orbitals, a new charge density is constructed. This process is repeated until the total energy is minimized self-consistently. However, due to the size of the crystalline systems, the traditional high-accuracy wave function-based quantum chemical methods are too expensive. Furthermore, it appears inefficient to retain all information contained in the wave function if, in the end, one is interested in averaged quantities, like, e.g., the ground state energy. Next, we discuss a different approach that can be employed by recognizing that the electron density contains the same information as the corresponding wave function.

1.2. Density Functional Theory

Density functional theory (DFT) allows this many-electron wave function problem to be solved *ab-initio* in practice for up to several hundred atoms with thousands of electrons [51]. The central idea of DFT is to make use of an exact reformulation of the problem that features the three-dimensional electronic charge density as the fundamental variable[3]

$$n(\mathbf{r}) = n \int d^3\mathbf{r}_2 \int d^3\mathbf{r}_3 ... \int d^3\mathbf{r}_n \Psi^*(\mathbf{r}, \mathbf{r}_2, ..., \mathbf{r}_n)\Psi(\mathbf{r}, \mathbf{r}_2, ..., \mathbf{r}_n) \tag{1.8}$$

instead of the $3n$-dimensional many-electron wave function, thus greatly reducing its complexity. This approach offers a good balance between accuracy,

[3]It is worth mentioning that the Thomas-Fermi model using electronic density as a basic variable contained the seeds for the development of the DFT for the definition of functional.

predictiveness, and computational cost. Furthermore, among notable recent successes of DFT are the prediction of new catalysts and new Li battery materials in the Materials Genome Project [42,52]; thus, it is hardly surprising that DFT formulations are among two of the top-ten cited papers of all time [43].

1.2.1. The Hohenberg-Kohn Theorems

Formally, we start with Hohenberg-Kohn (HK) theorems, which are at the heart of the DFT [51].

Theorem I. *For any system of interacting particles in an external potential*[4] $v_{ext}(\boldsymbol{r})$*, there is a one-to-one correspondence between the potential and the ground-state particle density* $n_0(\boldsymbol{r})$*. Any ground-state observable is a unique functional of the ground-state particle density* $n_0(\boldsymbol{r})$*.*

The first HK theorem states that $v_{ext}(\mathbf{r})$ is to within an additive constant a unique functional of $n(\mathbf{r})$[5]. Hence the ground state properties of a many-electron system are uniquely determined by an electron density i.e., for a given ground state density $n_0(\mathbf{r})$, it is possible to calculate the corresponding wave function. This means that wave function is a functional of electron density.

Theorem II *It is possible to define an energy functional* $E[n]$ *of the electron density for a given* $v_{ext}(\boldsymbol{r})$*, which is minimized and equal to the ground-state energy when* $n(\boldsymbol{r}) = n_0(\boldsymbol{r})$*.*

The second HK theorem states that the ground state density $n_0(\mathbf{r})$ can be determined from the ground state energy functional $E[n_0]$ via the variational principle by variation only of the density

$$E[n_0] = \int v_{ext}(\mathbf{r}) n_0(\mathbf{r}) d^3\mathbf{r} + F[n_0] < \int v_{ext}(\mathbf{r}) n(\mathbf{r}) d^3\mathbf{r} + F[n] = E[n]. \quad (1.9)$$

Functional $F[n] = T_e[n] + V_{ee}[n]$ is defined in terms of the density. DFT is made possible by the existence of these two ingeniously simple[6] HK theorems [51]. Thus, if $F[n]$ was known, the task of evaluating all of the properties of a system with a given external potential $v_{ext}(\mathbf{r})$ should be reduced to minimizing the energy functional of the 3-dimensional electron density. However, HK theorems do not offer a way of calculating the ground-state density $n_0(\mathbf{r})$ of a system in practice because the exact form of the functional $F[n]$ is unknown. About one year after HK published a paper [51], Kohn and Sham derived a simple formalism for carrying out DFT calculations, that retains the essence of DFT [55].

[4]External potential in DFT is the ionic potential from the atomic cores acting on the electrons in the system, as in 1.2 equation i.e., $v_{ext} \sim V_{\alpha e}$.

[5]Bright-Wilson gave an elegant explanation of why $n(\mathbf{r})$ determines $v_{ext}(\mathbf{r})$. He stated that the peaks of the electron density give us the positions of the nuclei $\mathbf{R}$, and their slopes allow us to determine their atomic numbers [53].

[6]The full proof of HK theorems is given in V. Sahni's book, chapter 4 [54].

1.2.2. The Kohn-Sham Formalism

Introducing orbitals into the HK picture, as was done in the Kohn-Sham (KS) formalism, paved the way to a computational breakthrough [55]. In the KS approach, the real interacting electron system is mapped onto a virtual system of non-interacting independent electrons. In this virtual system of non-interacting electrons, the overall ground-state density is identical to the density of a real system. Considering that the main flaw in initial DFT formalisms was the difficulty in representing the kinetic energy of the system, the central idea in KS approach is to split the kinetic energy functional into two parts: one that considers electrons as non-interacting particles and can be calculated exactly, and a small correction term accounting for electron-electron interaction [56]. Following the Kohn-Sham formalism, within an orbital formulation, the electronic energy of the ground state of a system can be written as [55]

$$E[n] = T_e[n] + V_{ee}^{\text{Hartree}}[n] + \int v_{ext}(\mathbf{r})n(\mathbf{r})d^3\mathbf{r} + E_{xc}[n]. \tag{1.10}$$

The Kohn-Sham kinetic energy functional $T_e[n]$ represents the kinetic energy of the non-interacting electrons

$$T_e[n] = \sum_{i=1}^{N} \int \psi_i^{\text{KS}*}(\mathbf{r}) \frac{-\hbar^2\nabla^2}{2m_e} \psi_i^{\text{KS}}(\mathbf{r})d\mathbf{r}. \tag{1.11}$$

In this formalism, the set of one-electron Kohn-Sham orbitals ψ_i^{KS} is used to construct the density $n(\mathbf{r}) = \sum_{i=1}^{N} |\psi_i^{\text{KS}}(\mathbf{r})|^2$. The second term in equation 1.10 is the Hartree term V_{ee}^{Hartree}, or the classical Coulombic repulsion of an electron density with itself,

$$V_{ee}^{\text{Hartree}}[n] = \frac{e^2}{2} \int \int \frac{n(\mathbf{r})n(\mathbf{r}')}{|\mathbf{r} - \mathbf{r}'|} d\mathbf{r}d\mathbf{r}'. \tag{1.12}$$

The third term in equation 1.10 is external potential acting on the electrons due to the nuclei, and the fourth term, known as the exchange-correlation term $E_{xc}[n]$, represents the correction to the kinetic energy arising from the interacting nature of the electrons, and all non-classical corrections to the electron-electron repulsion energy.

In the KS formalism, each one-electron wave function ${\psi_i}^{\text{KS}}$ has a corresponding Kohn-Sham equation, which is a single-particle Schrödinger equation with an effective potential chosen so that the sum of solutions produces a ground-state density of a system. Within the KS approach, the problem is reduced to solving a series of KS equations

$$\left[\frac{-\hbar^2}{2m_e}\nabla^2 + e^2 \int \frac{n(\mathbf{r}')}{|\mathbf{r} - \mathbf{r}'|} d\mathbf{r}' + v_{ext} + \frac{\delta E_{xc}[n]}{\delta n(\mathbf{r})}\right] \psi_i^{\text{KS}} = \varepsilon_i^{\text{KS}} \psi_i^{\text{KS}}. \tag{1.13}$$

On an operational level, Kohn-Sham equation 1.13 can be thought of as an attempt to improve on the Hartree-Fock method by including correlation effects into the self-consistent field procedure. Starting from a tentative set of KS orbitals and using the density constructed from this initial guess, the Kohn-Sham equations are solved to give new eigenfunctions. This set of orbitals is then used to calculate an improved density. The entire process is repeated until the total energy has satisfied a previously chosen convergence criterion, and at this point, the electronic energy is calculated[7].

In principle, this approach should produce the exact ground-state energy and density, but in practice, one small but vital contribution must be approximated – the so-called exchange-correlation energy $E_{xc}[n]$. The accuracy and quality of the results depends on the quality of this approximation [57]. The biggest challenge of DFT is the description of this term, which we discuss in the next section 1.2.3.

1.2.3. The Exchange-Correlation functional

He had a dream in which he saw a stairway resting on the earth,
with its top reaching to heaven, and the angels of God
were ascending and descending on it.
Jacob's dream, Genesis 28.12

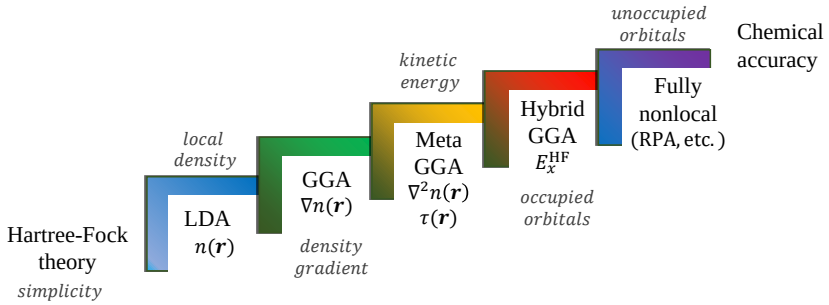

Figure 1.1. *Jacob's ladder* for the five generations of DFT functionals, according to the vision of John P. Perdew and Karla Schmidt. Sketch inspired by Ref. [58].

In this section, we present a *Jacob's ladder* of DFT approximations for the exchange-correlation energy $E_{xc}[n]$ as a functional of the electron density, which was described by John P. Perdew and Karla Schmidt [58]. In practical cases, the choice of functional $E_{xc}[n]$ strongly depends on the system of interest. Functionals vary from very simple to very complex [57, 59], nonetheless, all together,

[7]The most fundamental difference between DFT and HF is that DFT optimizes an electron density, while HF optimizes a wave function.

these functionals can be classified into *rungs* represented in a hierarchical form, ordinarily referred to as *Jacob's ladder*.

On *Jacob's ladder* of approximations, each rung represents a different level of approximation that should recover the results of lower rungs in the appropriate limits, lead to the chemical accuracy[8] and add more capabilities (Fig. 1.1). At the lowest rung of this ladder is the mother of all approximations, the local density approximation, where the local density determines the contribution to the energy. Higher rungs incorporate increasingly complex ingredients constructed from the density or the KS orbitals. We will now briefly discuss the first several rungs of this ladder to introduce some of the most widely used $E_{xc}[n]$ functionals.

Local density approximation

The simplest and the oldest approach, which is applied in materials science to represent the exchange-correlation functional $E_{xc}[n]$, is the local density approximation (LDA). This approach is based on considerations of the homogeneous electron gas, the only system for which the form of the exchange-correlation energy is known precisely. The generalization to the inhomogeneous system is then done by assuming that the exchange-correlation energy at each point in space depends on a locally constant electron density

$$E_{xc}^{\mathrm{LDA}}[n] = \int n(\mathbf{r})\varepsilon_{xc}^{\mathrm{LDA}}(n(\mathbf{r}))d\mathbf{r}, \tag{1.14}$$

where $\varepsilon_{xc}^{\mathrm{LDA}}(n(\mathbf{r}))$ is the exchange-correlation energy per electron corresponding to a homogeneous electron gas of density $n(\mathbf{r})$. It is usual to decompose $E_{xc}^{\mathrm{LDA}}[n]$ energy into an exchange and correlation parts $E_{xc}^{\mathrm{LDA}}[n] = E_x[n] + E_c[n]$. For LDA, the analytical expression for the exchange energy is known

$$E_x = -\frac{3}{4}\left(\frac{3}{\pi}\right)^{\frac{1}{3}} \int n(\mathbf{r})^{\frac{4}{3}} d\mathbf{r}. \tag{1.15}$$

The correlation energy is more complicated. However, expressions for the high and low density limit are available, and values in-between can be fitted to highly accurate quantum Monte Carlo calculations [60]. It is also possible to consider the extension of LDA functional to spin-polarized systems by separating the total density into the individual contributions from electron spin; that is especially important for the accurate description of elements expressing magnetism. DFT with the LDA has been shown to give accurate results in a variety of systems, most notably solids with strong covalent, ionic or metallic bonding, and is less useful for atoms and molecules, which bear less resemblance to a uniform electron gas [59]. Furthermore, LDA underestimates bond lengths

[8] Chemical accuracy is defined as 1 kcal/mol or 0.043 eV.

and overestimates binding energies. These features can be partly corrected by using more sophisticated DFT-based approaches.

Generalized gradient approximation

On the next rung is the generalized gradient approximation (GGA) or semi-local approximation, which depends on both the electron density and its gradient. The LDA approximation only incorporates the knowledge of the density at a certain point in space and assumes a certain spatial homogeneity of the electron density. Nonetheless, the ordinary physical system is typically inhomogeneous, thus the full expression is the gradient expansion approximation, which models a system where the density is slowly varying

$$E_{xc}^{\mathrm{GGA}}[n] = \int \varepsilon_{xc}^{\mathrm{GGA}}(n(\mathbf{r}), \nabla(n(\mathbf{r}))d\mathbf{r}. \tag{1.16}$$

Most GGA functionals are constructed in the form of a correction term which is added to the LDA functional

$$\varepsilon_{xc}^{\mathrm{GGA}}(n) = \varepsilon_{xc}^{\mathrm{LDA}}(n) + \Delta\varepsilon_{xc}\left[\frac{|\nabla n(\mathbf{r})|}{n^{4/3}(\mathbf{r})}\right]. \tag{1.17}$$

The dependence of the correction term $\Delta\varepsilon_{xc}$ is on the dimensionless reduced gradient [61]. GGA significantly improves upon the LDA and allows to describe most types of chemical bonds and binding energies in molecules, which has made DFT useful in chemistry[9]. Even though GGA functionals made DFT a standard tool for studying a broad range of applications, the main issue is that the gradients in natural materials are huge, which may cause the GGA expansion to fail. One of the biggest drawbacks of the LDA and GGA is the self-interaction error, which causes a spurious delocalization of the KS eigenstates (e.g. charge delocalization at defect). The second drawback is the underestimation of the fundamental gap for most of semiconductors and insulators. Recently, new functionals like Meta-GGA, that include higher-order gradient corrections[10], have been reported, but they are still in the relatively early stages of development. Next, we will discuss Heyd, Scuseria, and Ernzerhof hybrid functional [62], which is the functional employed in this Thesis.

[9] It is interesting to note that in chemistry, GGA exchange functionals contain empirical parameters whose values have been fitted to reproduce experiments. Whereas in physics, $\varepsilon_{xc}^{\mathrm{GGA}}[n]$ have been developed based on a rational function expansion of the reduced gradient and contain no empirically optimized parameters (e.g. PBE) [57].

[10] Meta-GGA functional includes the non-interacting kinetic energy density $\tau(\mathbf{r}) = \frac{1}{2}\sum_i |\nabla\psi_i^{\mathrm{KS}}(\mathbf{r})|^2$. Implementation of such a functional is likely to be expensive.

Hybrid functional DFT calculations

The fourth rung of *Jacob's ladder* is devoted to computationally more demanding non-local hybrid functionals, obtained by admixing a fixed amount of the Hartree-Fock exchange. The most successful and widely used functional in *ab-initio* studies of point defects in semiconductors is Heyd, Scuseria, and Ernzerhof hybrid functional, known as HSE [62]. HSE is a mixture of screened Hartree-Fock exchange with the GGA exchange-correlation functional of Perdew, Burke, and Ernzerhof (PBE) [63].

Firstly, HSE functional separates the exchange interaction, which falls off as $1/r$, into a short-range and long-range components by a switching function, usually an error function

$$\frac{1}{r} = \underbrace{\frac{\mathrm{erfc}(\sigma r)}{r}}_{\text{short-range}} + \underbrace{\frac{\mathrm{erf}(\sigma r)}{r}}_{\text{long-range}} . \tag{1.18}$$

Here, σ is the screening parameter, which controls the range-separation. The underlying justification for range-separated hybrids is that in natural materials, the exchange interaction is screened by the electrons, and exchange effects occur on a short-range scale[11].

In the HSE06 functional, the GGA-PBE exchange is mixed with Hartree-Fock exchange for the short-range interaction, while the GGA-PBE functional solely describes the long-range exchange as well as correlation

$$E_{xc}^{\mathrm{HSE}}[n] = \alpha E_x^{\mathrm{HF,\ SR}}(\sigma) + (1-\alpha) E_x^{\mathrm{PBE,\ SR}}(\sigma) + E_x^{\mathrm{PBE,\ LR}}(\sigma) + E_c^{\mathrm{PBE}}. \tag{1.19}$$

Parameter α defines the fraction of the HF exchange that should be mixed to the DFT part, and E_c^{PBE} is just the correlation energy from GGA-PBE, superscripts SR and LR indicate short-range and long-range, respectively.

According to recent calculations, HSE06 functional could very well reproduce the experimental band gaps for many materials and provide more accurate enthalpies of formation [64, 65]. Furthermore, HSE06 hybrid functional provides the most accurate results for bulk and *sp*-point defect-related quantities [66]. The reason for this improvement is the fact that many properties are overestimated by DFT and underestimated by HF method or vice versa, and the mixture of both gives good intermediate results. Furthermore, adding a certain fraction of HF reduces the *self-interaction error*.

The last rung, random phase approximation (RPA), describes correlation energies from the unoccupied KS orbitals. They require substantial basis sets

[11] The HF exchange is essentially Coulomb interaction ($1/r$), which may decay and converge very slowly, whereas in approximate DFT Coulomb interaction decays too quickly. It was proposed that a screened Coulomb integral could solve this problem. Due to the advantage of simple analytic integration, the complementary error function $\mathrm{erfc}(x)$ and error function $\mathrm{erf}(x)$ are used for the range-separation of the exchange part [62].

Table 1.1. Atomization energies (in eV) of small molecules computed with various exchange-correlation functionals: HF, LDA, GGA, Metta-GGA, Hybrid (B3LYP), and RPA are compared with experimental values (Exp.). Based on literature [67, 68].

	HF	LDA	GGA	Meta-GGA	Hybrid	RPA	Exp.
N_2	4.945	11.524	10.492	9.847	9.679	9.632	9.804
P_2	1.548	6.149	5.203	5.074	5.151	4.988	5.031
O_2	1.419	7.482	6.192	5.633	5.280	4.816	5.160
CO	7.482	12.857	11.567	11.008	11.223	10.406	11.137

and are not yet practical for general use.

In Table 1.1, different exchange-correlation approximations for atomization energies are compared [67, 68]. The lack of electron correlation makes Hartree-Fock calculations only good for qualitative description. The LDA has the overbinding tendency. The GGA functional and the inclusion of higher-order gradient of the density improve the result quantitatively. Hybrid scheme (e.g. B3LYP) gives a mean absolute error of 0.1 eV (or 2 kcal/mol) on this set of molecules [67, 68] (Table 1.1).

1.3. DFT Implementation

In calculations of condensed matter systems, that will be the main types of systems that DFT is applied to in this Thesis, the plane-wave (PW) basis set is the most popular and natural choice. In many cases, the pseudopotential approach is combined with plane-wave for treating the strong interactions between tightly bound core electrons and nuclei. We will now briefly discuss plane-waves in subsection 1.3.1 and then pseudopotentials in subsection 1.3.2.

1.3.1. Plane-wave basis set

The implementation of DFT to study infinite systems, such as solids, requires the use of periodic boundary conditions. The solution of Kohn–Sham equation, for such a periodic system, must satisfy Bloch's theorem. Single-electron KS orbitals are expressed as a product of a plane wave with a periodic function

$$\psi_{n,\mathbf{k}}(\mathbf{r}) = e^{i\mathbf{k}\cdot\mathbf{r}} u_{n,\mathbf{k}}(\mathbf{r}), \tag{1.20}$$

where n corresponds to energy band, $u_{n,k}(\mathbf{r})$ has the same periodicity of the unit cell of the system[12], $\mathbf{k}$ is a wave vector. Bloch function for any reciprocal lattice

[12] Periodic function is translationally invariant.

vector $\mathbf{G}$ is $\psi_{n,(\mathbf{k}+\mathbf{G})} = \psi_{n,\mathbf{k}}$, this implies that in a practical DFT calculation, one can restrict $\mathbf{k}$ to the first Brillouin zone.

The periodic part of the wave function can be expanded as a set of plane waves

$$u_{n,\mathbf{k}}(\mathbf{r}) = \sum_{\mathbf{G}} c_{n,\mathbf{k}+\mathbf{G}} e^{i\mathbf{G}\cdot\mathbf{r}}, \tag{1.21}$$

where $c_{n,\mathbf{k}+\mathbf{G}}$ is the plane wave coefficient. Thus, single-electron Kohn-Sham orbitals can be written as a linear combination of plane waves

$$\psi_{n,\mathbf{k}}(\mathbf{r}) = \sum_{\mathbf{G}} c_{n,(\mathbf{k}+\mathbf{G})} e^{i(\mathbf{k}+\mathbf{G})\cdot\mathbf{r}}. \tag{1.22}$$

In order to decrease the computational cost, the number of basis functions used is controlled by the largest wave vector in the expansion 1.22, i.e., the basis set is restricted. This is equivalent to imposing a cut-off on the kinetic energy as the kinetic energy of an electron with wave vector $(\mathbf{k}+\mathbf{G})$ is given by $\frac{|\mathbf{k}+\mathbf{G}|^2}{2}$. This cut-off energy defines the size of the PW basis set, i.e., the kinetic energy for the largest reciprocal lattice vector included in the PW basis[13] [69].

1.3.2. Pseudopotentials

Pseudopotential plane-wave method (PSPW)

Although the plane-wave method has its advantages, however, a prohibitively large number of plane-waves is required to accurately describe the rapidly oscillating wave functions of electrons near to a nucleus. The pseudopotential plane-wave (PSPW) method, which represents the potential of the ionic cores[14] is an efficient way to calculate material properties using DFT. In the PSPW method, the Coulomb potential $V(r)$ in the many-electron system Hamiltonian is replaced with a smooth function $\tilde{V}(r)$ by that the electron wave functions $\psi(r)$ oscillating rapidly in the core region are replaced by nodeless pseudo-orbitals $\tilde{\psi}(r)$ having the right energy and the same outer range properties, i.e. $\tilde{\psi}(r)|_{\,r=r_c} = \psi(r)|_{\,r=r_c}$ [70]. The pseudopotentials are chosen such that the resulting pseudo atoms have the same scattering properties as the original atoms [71]. By this, computing resources can be used efficiently with minimal effect on the accuracy of the calculation [72]. The schematic representation of the behavior of a pseudo wave function and pseudopotential is depicted in Fig. 1.2. The drawback of the PSPW method is that all information on the full wave function close to the nuclei is lost.

[13] The cut-off energy $E_{\text{cut}} \geq \frac{\hbar}{2m}(\mathbf{k}+\mathbf{G})$ must be increased until the total energy and other properties of interest are converged to within an acceptable range, i.e., it is sufficient to monitor the eigenvalues and total energies as a function of the cut-off energy.

[14] General assumption in the pseudopotential approximation is that only the valence electrons have a significant effect on the physical and chemical properties of the system, i.e., the core electrons are considered to be chemically inert.

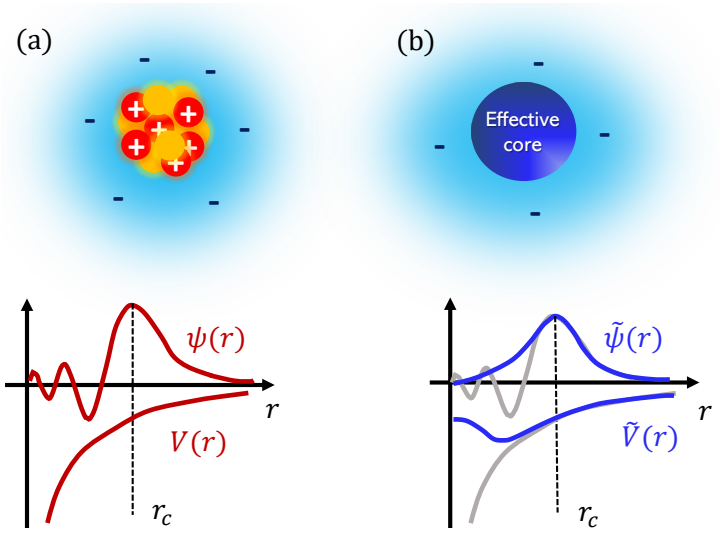

Figure 1.2. Schematic diagram of a pseudopotential. (a) The true unscreened, all-electron wave function $\psi(r)$ in the Coulomb potential $V(r)$ of the nucleus is compared to (b) the pseudo wave function $\tilde{\psi}(r)$ in the screened pseudopotential $\tilde{V}(r)$. Beyond the chosen cut-off radius r_c, both the pseudo wave function and pseudopotentials become identical to the real all-electron ones.

Projector-augmented wave method (PAW)

The so-called projector-augmented wave method (PAW) is an improvement of the pseudopotential technique approach [73,74]. In the PAW approach, rapidly varying parts of the electronic functions are projected onto a local basis set, e.g., a basis of atomic functions [71]. The PAW method is based on a transformation which links the pseudo wave function to the all-electron KS wave function by splitting the latter into two parts

$$\psi = \tilde{\psi} + \sum_{i}^{N} c_i \left(\phi_i - \tilde{\phi}_i\right). \tag{1.23}$$

The first part $\tilde{\psi}$ is the pseudo wave function and can be represented in terms of a plane wave basis set of suitable size. ϕ_i and $\tilde{\phi}_i$ are the atomic all-electron partial waves and the pseudo partial waves, respectively. The all-electron partial waves ϕ_i are introduced to correct the error of deviation of pseudo wave function near the nucleus. By this decomposition in equation 1.23, the original wave function is separated into pseudo wave functions that are smooth everywhere, and contributions including fast oscillations affecting certain region in space, the so-called *muffin-tin* region [73–75]. Space near the nucleus is divided accordingly into atom-centered spheres, defining the atomic regions,

and an interstitial region in between. The partial solutions of the different regions are matched at the interface between atomic and interstitial regions, i.e., wave functions and their derivatives are required to be continuous at the interface [76]. These all-electron partial waves ϕ_i are solutions of the radial Schrödinger equation for the isolated atoms inside the *muffin-tin* region i.e. inside an augmentation sphere, and pseudo partial waves $\tilde{\phi}_i$ are constructed as solutions of the radial Schrödinger equation for isolated atoms fitted to match the pseudo wave function $\tilde{\psi}$ [72, 74]. All-electron partial waves add the all-electron wave function inside an augmentation sphere and pseudo partial-waves cancel the smooth pseudo wave function inside an augmentation sphere [77].

In this Thesis, calculations are predominantly carried out using the Vienna *ab-initio* simulation package (VASP) developed by Georg Kresse and his coworkers [78], which is a plane wave DFT code. The valence electrons are separated from the core by use of PAW potentials as implemented in the VASP code.

1.3.3. Brillouin zone integration

The DFT calculation of many properties of solids involves integrating periodic functions $f(\mathbf{k})$ of a Bloch wave vector over the Brillouin zone (BZ) in reciprocal space [79, 80]. In practise, integrals over the BZ are replaced by a summation over the discrete set of k-points. By taking advantage of the symmetry of the system, this sum can be carried only over special k-points i.e. the largest subset of k-points for which no two k-points in the subset are symmetrically equivalent [80]

$$\frac{1}{(2\pi)^3}\int_{\mathrm{BZ}} f(\mathbf{k})d\mathbf{k} = \frac{1}{N\Omega}\sum_{i=1}^{N} f(\mathbf{k}_i) = \frac{1}{\Omega}\sum_{\mathbf{k}} w_{\mathbf{k}} f(\mathbf{k}). \tag{1.24}$$

Here Ω is the volume of the unit cell and the sum is over all k-points in the BZ; and $w_{\mathbf{k}}$ is the weight of the special k-points. The weights, that contain the effects of symmetry, must sum up to unity ($\sum_{\mathbf{k}} w_{\mathbf{k}} = 1$).

Monkhorst-Pack [81] method generates an evenly spaced grid ($M_1 \times M_2 \times M_3$) of k-points along the reciprocal lattice vectors of the structure throughout the BZ which provides an efficient means of integrating periodic functions of the wave vector. This method weights k-points from a given uniform mesh by using the symmetry of the system, see Fig. 1.3, i.e. the integrals are evaluated in a reduced region called the irreducible BZ which can be extended to fill the entire BZ [79].

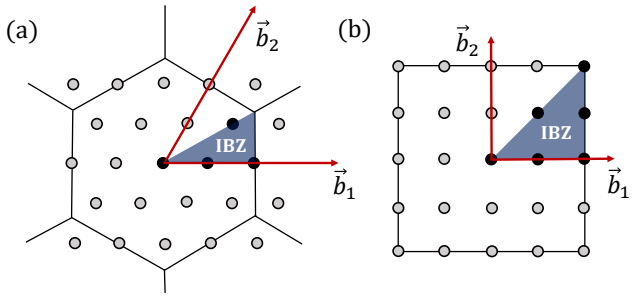

Figure 1.3. Special k-points (black circles) for the 2D (a) hexagonal and (b) cubic lattices. Monkhorst-Pack meshes 5×5 produce (a) 4 and (b) 6 special k-points, respectively. Γ-centered k-mesh preserves the symmetry. The irreducible wedges, i.e. symmetry-inequivalent parts of the BZ are shaded. Illustration adapted from Ref. [79].

1.3.4. Supercell approach

Results obtained through DFT calculations provide means for reliable interpretation and assignment of defect fingerprints in condensed matter systems observed by many different experimental techniques [45,82,83]. Most often, calculations of isolated defects are performed with a supercell approach [82, 84]. In this method, the defect that is contained within a supercell (i.e., large unit cell) is repeated periodically in space.

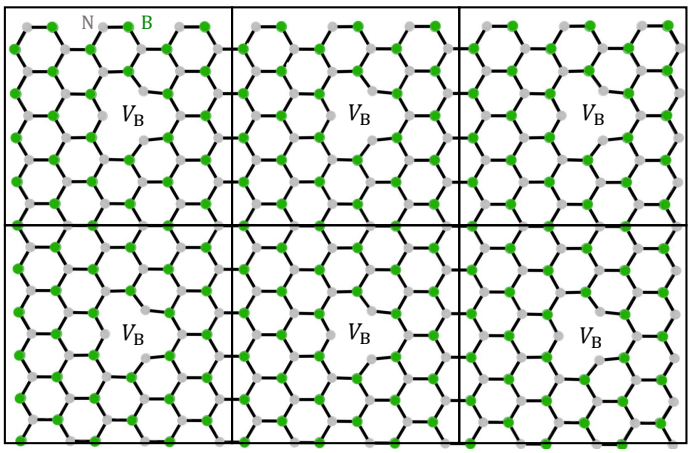

Figure 1.4. The hBN supercell containing a boron vacancy (V_B) is repeated periodically in all directions of space. Here only one layer of hBN supercell containing V_B in it is shown. Boron atoms are indicated by green spheres, nitrogen are grey.

In order to avoid neighboring cell interactions, the supercell must be large enough. Typical sizes of the supercell for studying wide-band-gap semiconductors are from several dozen to few hundreds of atoms. In this Thesis, we constructed the supercell by a change of basis to an orthorhombic structure, for which the unit cell is a rectangular prism with side lengths $a \times \sqrt{3}/2a \times c$ in terms of the length of the hBN lattice constants. The supercell is then a $5 \times 6 \times 2$ multiple of this orthorhombic cell, leading to a 240-atom supercell. This supercell results in a defect concentration of roughly $4.7 \cdot 10^{20}\text{cm}^{-3}$ and a distance of approximately ~ 12.8 Å between defects[15].

From supercell approach calculations one can extract probabilities of certain types of defect to form under given chemical and thermodynamical conditions during the growth, predict their structures, nature of the electronic defect states, migration barrier, elucidate their vibrational modes and other ground-state properties as well as optical properties from excited-state calculations. At present, the computational accuracy of the defect energy level position is typically a few tenths of an eV [82]. However, other more complicated problems arise with charged defects, exchange-correlation functionals, and other technicalities that are being addressed. Errors may also arise due to defect wave-function overlap, magnetic interactions, and strain [85]. Appropriate correction schemes, guaranteeing accuracy, will be introduced in 3 and 5 chapters of this Thesis.

In summary, *ab-initio* calculations play a crucial role in identifying, characterizing, and developing defects for quantum applications.

[15]Such a periodic array contains unrealistically large defect concentrations, resulting in artificial interactions (i.e., finite-size and periodicity effects like electrostatic, elastic or magnetic interactions [45, 82, 83]) between the defects. All mentioned artificial interactions are taken into account during the calculations.

Unique sources of light

As it turns out, nature allowed us to be imperfect.
Perhaps it's a kind of aesthetics and unusual art.
It tends to be even more breathtaking,
if we start to neglect the rules through symmetry breaking
confining there electrons that in turn
will give us unique sources of light.

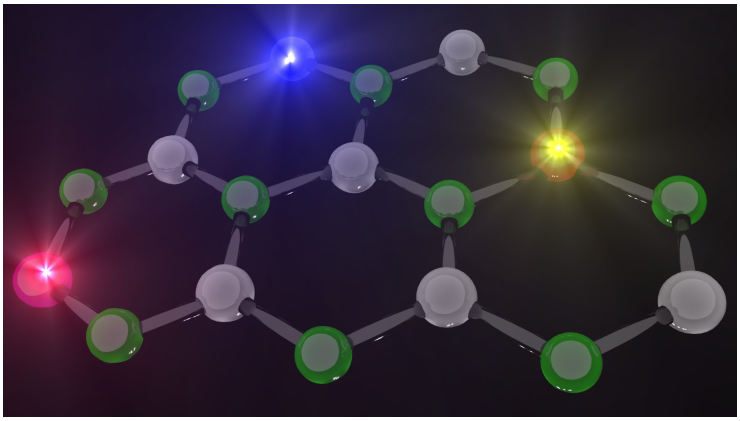

Illustration of single-photon emission from *unknown* point defects in hBN.

Chapter 2

Single-photon emitters in hBN

Many ideas for future technologies that will make use of the quantum nature of light require sources that produce streams of photons with controllable quantum correlations. Those are produced by single-photon emitters (SPEs) – crucial components for many photonic quantum technologies [1, 6, 86]. The most promising candidates for practical true SPE today are solid-state emitters that are a key ingredient in linear optical quantum computing and quantum key distribution (e.g. recently, BB84 protocol was implemented and SPEs based on defect centres in diamond were tested at room temperature) [87].

Table 2.1. Key properties of ideal single-photon emitters. Summarizing Ref. [1, 86, 88].

Properties of ideal SPEs	Requirements
(1) photostability	no blinking and no bleaching
(2) high brightness[16]	high emission rate ($10^6 - 10^7$counts/s)
(3) high single-photon purity	low multiphoton emission probability
(4) indistinguishability of photons	two-photon destructive interference[17]

First of all, single-photon emitter should display anti-bunching of photons – photons must be emitted from the source one at a time [89]. This so-called anti-bunching of emitted photons can arise from various mechanisms, but ensures that the probability of obtaining two or more photons at the same time remains negligible. Moreover, photons should be on-demand and deterministic, with well-defined spatio-temporal, spectral, and polarization modes. However, there is still no ideal SPE, and it raises the question – how does one recognize the *ideal*

[16] Additional requirement similar to (2) is a high quantum efficiency of the SPE, which is defined as the radiative rate divided by the overall (radiative plus nonradiative) rate.

[17] In 1987, Hong, Oum, and Mandel experimentally verified the interference with a beam splitter for two indistinguishable photons.

SPE? The answer is the necessary condition for any practical future application and fabrication. Furthermore, the quest for a perfect single-photon source requires additional properties mentioned in Table 2.1. In particular, the full characterization of the quantum emitter itself is of great importance [44].

In chapter 2, we discuss the identification of quantum point defects in new materials for applications in quantum science. This discussion will especially highlight how new applications can emerge from the investigation of the defect's fundamental properties. In the second part of this chapter, we will review various SPE systems and their properties. Finally, we will discuss the nature of the defects in hBN that remains unanswered and controversial, and thus calls for more in-depth analysis and further investigations.

2.1. Characterization of single-photon emitters

In section 2.1.1, we discuss the attributes and characteristics of single-photon sources that are identified by the photon-counting statistics of the light that they generate. Next, in section 2.1.2, we briefly review a few experimental techniques used for the optical characterization of solid-state SPEs.

2.1.1. Photon correlation measurements

One of the most challenging parts of the single-photon extraction is demonstrating that indeed only a singular photon has been produced; this task is in itself complex. How do we know that we indeed have produced a *single photon*? The primary tool at the disposal is Hanbury Brown and Twiss (HBT) interferometer [90]. Measurement of correlations between photons originating from any particular two-level (or three-level) emitter in the presence of a continuously exciting field may reveal their single-photon nature.

Popular light source characterization technique is the measurement of time-intensity second-order correlation function $g^{(2)}(\tau)$

$$g^{(2)}(\tau) = \frac{\langle I(t)I(t+\tau)\rangle}{\langle I(t)\rangle^2}. \tag{2.1}$$

In the simplest terms, $g^{(2)}(\tau)$ measures the degree of correlation between the intensity of a light beam $I(t)$ measured at two different times, separated by the time delay τ. Experimentally, $g^{(2)}(\tau)$ function is investigated by measuring the dynamics of photons and their arrival time, where timing information is obtained between consecutive photons detection processes[18] [91]. The mea-

[18]The $I(t)$ of the signal is obtained by counting the number of output pulses (i.e. photon counting) within a measurement time slot, while the time-dependent waveform of the signal is obtained by measuring the time distribution of the output pulses (i.e. photon timing). With current technology, the arrival time of photons can be measured with picosecond temporal resolution.

surement of this $g^{(2)}(\tau)$ function can be performed in an HBT type setup, as illustrated in Fig. 2.1 (c). In the HBT setup, the emitted light of the studied SPE is lead into a beam splitter (50:50), after which both light paths are guided into avalanche photon detection (APD) devices that collect the time of detection on a brief time scale. The time differences between two detections are added to a histogram, which is an approximation to the $g^{(2)}(\tau)$ function. HBT measurement determines the joint probability of photon detection from SPE at time t and second photon detection at time $t+\tau$. At any time, no more than one photon can be detected from SPE in a fixed time bin, i.e., and photon number is $n = 1$.

In the quantum derivation of $g^{(2)}(\tau)$ the measurement interferes with the measured system. While the first measurement counts n photons, the second one (affected by the first one) counts only $(n-1)$ photons. The expected value of second-order correlation function can be rewritten in terms of the photon number operator $\hat{n} = \hat{a}^\dagger \hat{a}$, with the photon annihilation $\hat{a}$ and creation $\hat{a}^\dagger$ operators[19]

$$g^{(2)}(\tau) = \frac{\langle \hat{a}^\dagger(t)\hat{a}^\dagger(t+\tau)\hat{a}(t)\hat{a}(t+\tau)\rangle}{\langle \hat{a}^\dagger(t)\hat{a}(t)\rangle^2}, \quad g^{(2)}(0) = \frac{n(n-1)}{n^2} = 1 - \frac{1}{n}. \quad (2.2)$$

With this, we see that a deterministic SPE should have $g^{(2)}(0) = 0$, as this quantity is connected to the probability of emitting two photons or more at the same time. This value is lower than that expected for thermal light sources ($g^{(2)}(0) = 2$) or for coherent light[20] ($g^{(2)}(0) = 1$) [92, 93].

The clear signature of an SPE is a characteristic dip in $g^{(2)}(0)$ function i.e., anti-bunching (see Fig. 2.1 (d)), which correlates arrival times of photons that reach a detector. However, it is challenging to achieve $g^{(2)}(0) = 0$ in the experiment due to the contribution of the background signal from the substrate or other surrounding SPEs. Therefore, it is widely accepted that a source with $g^{(2)}(0) < 0.5$ is considered as SPE [95, 96]. Furthermore, if the pumping rate is much lower than the inverse of the quantum emitters lifetime, we can take function $g^{(2)}(\tau) = 1 - \alpha e^{(-\tau/\tau_{\mathrm{rad}})}$ for a two-level system (α is a fitting parameter) and extract the lifetime τ_{rad} of a measured SPE [91, 96, 97]. Additionally, the shape of $g^{(2)}(0)$ function enables a clear distinction to be made between two and three-level systems. For example, in Fig. 2.1 (d) a bunching effect is observed for a three-level system, i.e., the enhanced probability to detect a photon at short times than at longer times[21] and $g^{(2)}(\tau)$ is higher than 1. For potential applications of single-photon sources, we are only interested in

[19] A detailed demonstration of the derivation of $g^{(2)}(\tau)$ function can be found in M. Fox and R. Loudon [92, 93] "Quantum optics" books.

[20] Photons emitted from lasers are distributed randomly in time.

[21] The waiting interval while the system is in the metastable state, which has a longer lifetime, creates the bunching effect, i.e. $g^{(2)}(\tau) > 1$ [96]. Kianinia *et al.* observed bunching effect for 4-level SPE in hBN [29].

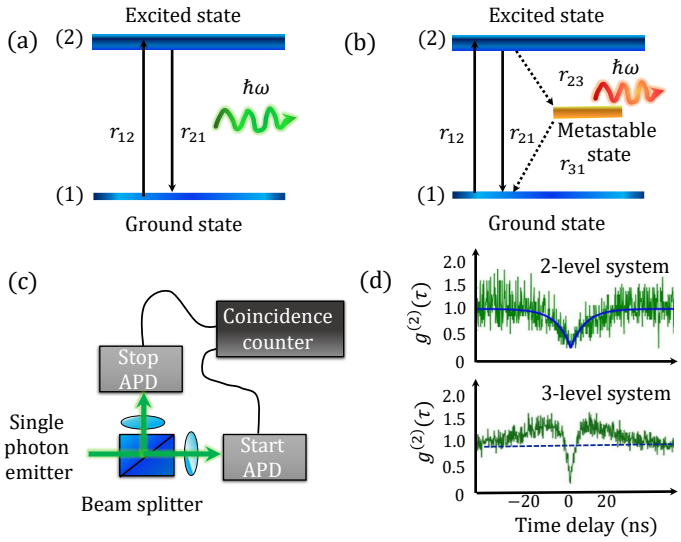

Figure 2.1. (a) A 2-level emitter with energy levels separated by the photon energy and (b) 3-level emitter, where r_{ab} are transition rates from level i to level j $(i, j = 1, 2, 3)$. (c) HBT setup. (d) $g^{(2)}(\tau)$ function of a 2-level SPE presenting an anti-bunching at $\tau = 0$ and $g^{(2)}(\tau)$ function of a 3-level SPE presenting a bunching (i.e. $g^{(2)}(\tau) > 1$) at finite delay together with the anti-bunching at $\tau = 0$. Graph of $g^{(2)}(\tau)$ functions inspired by Ref. [94].

two-level systems as three-level systems suffer from quenching (due to the presence of a metastable state; they have lower quantum efficiency than two-level systems) [96, 97]. On the other hand, two-level systems are likely to be of less use for spin qubits, as there will be no comparable spin-pumping or readout mechanism[22] [44, 98].

2.1.2. Optical characterization techniques

Measurement of single-photon emission faces the difficulty of combining effective addressing of SPEs with an efficient optical excitation considering that specific size of SPEs is in the nanometer range for quantum dots[23], and even smaller for imperfections such as point defects in semiconductors. Now we will give a brief review of a few of the most common SPEs optical characterization methods.

[22] As a result of an intermediate states, a strong bunching effect for charged nitrogen-vacancy (NV^-) center in diamond is observed. It is directly linked to the spin polarisation and readout properties of the emitter [96]. SPEs that do not display bunching effect are assumed to be spin-1/2 systems with no intersystem crossing [44, 98].

[23] The size of a typical quantum dot is between 5 and 100 nm, i.e., about 10^4 atoms may form a quantum dot.

Laser scanning confocal microscope allows us to perform selective excitation and detection of SPE emission at room temperature [29, 99]. Photoluminescence (PL) mapping of the surface with a laser beam, focused on an area of about 1 µm in diameter, enables detection of individual bright spots that give rise to a sharp optical signal from the host material [23]. Furthermore, confocal microscopy setup allows good collection efficiency of emitted photons, i.e., spectrally isolated emission from SPE is collected through the objective, passed through filters, and directed through optical fiber into the spectrometer [98]. Confocal microscopy, together with HBT setup, are the primary tool used for the search of new SPEs.

Photoluminescence excitation (PLE) spectroscopy combines high power supercontinuum white-light laser source with a grating monochromator that selects excitation wavelength [100]. During the measurement, the total intensity of emission over a fixed wavelength range is monitored while the excitation wavelength is swept through resonance with absorbing transitions of the SPE [98]. PLE technique allows to achieve much higher spectral resolution than PL. Furthermore, the energy level structure of SPEs, i.e., zero phonon line (ZPL) fine structure, can be investigated by PLE with narrow-line-width tunable laser source, e.g., the excitation wavelength is changed from 460 to 650 nm with a step size of 1 nm when measuring SPEs in solids [101]. Hence, the profile of the SPEs emission bands with vibronic character, i.e., phonon-assisted emission, can be monitored. At the same time, the electronic resonances are excited[24] [98].

Even in the highest-quality samples, relatively high density of point defects is expected; therefore, that imposes the use of a high spatial resolution spectroscopy to be employed. Cathodoluminescence (CL) is the nanometer scale analog of PL technique and integrated into a scanning transmission electron microscope (STEM), it allows a spatial selectivity as high as a few nanometers while providing a relatively easy access to a wide spectral range [91, 102]. CL-STEM images are obtained by sequentially recording one full CL spectrum per pixel while scanning the sample with a nanometric step size [103].

The attempt to obtain an image of isolated atoms has been one of the central goals in the development of electron microscopes. Annular dark-field (ADF) imaging, in conjunction with STEM, can resolve and identify the atomic species in the material of interest as the collected dark-field signal[25] increases with the atomic number [104, 105]. In ADF-STEM small probe of electrons is rapidly scanned across the sample, and the collected signal is strong enough to image all types of atoms, including light ones, e.g., Krivanek *et al.* demonstrated

[24] E.g. PLE experimental results confirmed the presence of a higher energy transition at 2.31 eV for SiV^- in diamond [101]. PLE on NV^- center allowed one to resolve 6 different transitions [98].

[25] The collected dark-field signal is due to Rutherford scattering of electrons from the partially screened atomic nucleus.

that ADF-STEM technique could clearly distinguish impurities in monolayer hBN [105].

Among other methods is time-resolved PL that can provide the spectral and temporal evolution of the SPE emission [106]. In the time-resolved PL method, SPE is excited with a short laser pulse. Then fast detector is used to determine the emission as a function of time after excitation. Histograms of photon arrival times per time bin are recorded, and the PL decay is reconstructed. It is essential to mention that the sample preparation process deserves special attention because it determines the quality of the observed optical response of SPE during the measurement [29, 98].

2.2. Review of single-photon emitters

Here, in section 2.2.1, we briefly compare a few different SPE systems before focusing on SPEs in hBN in section 2.2.2.

2.2.1. Platforms for the realization of single-photon emitters

The discovery by Kimble *et al.* in 1977 of photon anti-bunching from sodium atoms was the first observation of single-photon emission [107]. Although the reliability and efficiency of discovered SPEs were low, it was demonstrated that trapped atoms and ions are the purest source of single photons with a narrow emission line. These SPEs are intrinsically incapable of multi-photon emission[26] [108]. Currently, it is possible to control cold atoms to produce single photons on-demand efficiently [1]. However, the major difficulty lies in combining an ion trap with an optical cavity. Therefore, trapped atom or ion sources are not the optimal choice for technological applications leading to complex set-ups. Furthermore, SPE emission from trapped atoms/ions is undirected; this leads to poor detection efficiency. Additionally, it is yet to be demonstrated whether they can be coupled efficiently to network links [109].

As a benchmark for any new single-photon source technology, spontaneous parametric down-conversion is used. SPE source is based on a nonlinear frequency conversion process, where a pump laser forms pairs of photons in a birefringent crystal [110]. However, this process is non-deterministic[27]. Moreover, a critical issue is that the probability of creating pairs scales with pump intensity [111].

Nanocrystals consisting of organic dyes and aromatic molecules act as efficient SPE systems likewise. Although these SPEs are linearly polarized and

[26] For example, a trapped $^{138}Ba^{+}$ ion demonstrates $g^2(0) = 1.9 \cdot 10^{-3}$ [108].

[27] Photon pairs are generated at random times.

oscillator strength is very close to unity, the Debye-Waller[28] (DW) factor is negligible (DW = 0.1), and it decreases quickly for temperatures higher than 4 K. Debye-Waller factor is the ratio between the intensity of the ZPL and the total intensity of the emission spectrum. Similarly, the width of the ZPL increases steeply with temperature because of phonon-induced dephasing processes [109]. However, the biggest issue here is photostability and photobleaching that is limited at room temperature (RT)[29], i.e., thermal fluctuations from the excited state activate photochemical processes [112]. For practical applications, it is desirable to have SPE that works at RT. Nevertheless, recent research demonstrates that photostability can be improved [113]. Still, the size and shape of the resulting nanocrystals needs to be controlled more precisely.

These findings were followed by a demonstration of single-photon emission from quantum dots (QDs) [114]. Particularly important is that attractive quantum dots are made from epitaxial semiconductor compounds, e.g., III–V (InGaN/GaN, InAs/GaAs) and II-VI (CdSe/ZnS). One of the biggest advantages here is the possibility and realization of integrated QD-optical microcavity systems, i.e., systems that combine exceptional optical properties of QDs with the scalability of solid-state systems [115, 116]. In comparison with organic dyes, the semiconductor QDs have wide excitation spectra and narrow emission bandwidths as well as size-tunable PL in the visible spectral range[30] [117]. These SPEs are brighter, more stable, on-demand, and their size-tunable emission can be excited with a single light source. However, deterministic positioning and control of SPEs remains elusive for epitaxial QDs, similarly for fluorescent defects in solids. Other drawbacks, such as the cryogenic operating temperatures, limit their application potential, i.e., RT is still a technical challenge for some of QDs. Furthermore, droplet QDs have random spatial positions. Thus light emission from an ensemble is inhomogeneously broadened because of QD size fluctuations and local environmental variations[31], reproducibility of the samples, and growth of multiple identical dots is likewise an issue [115, 118].

The detection of negatively charged nitrogen-vacancy (NV^-) center in diamond at RT with scanning confocal microscopy in 1997 marked a turning point in the evolution of diamond-based quantum technologies [8]. Out of 500 luminescent centers in diamond, about 10 so far have been identified as bright, stable SPEs [119]. However, the chemical structure of only very few diamond

[28] SPEs with high Debye-Waller factors are very useful for many applications, where there is a need for a robust and narrow band signal, and a high signal to noise ratio.

[29] Increased temperature induces conformational changes of the molecule, which results in a decrease of SPE quantum yield [109].

[30] CdSe/ZnS core-shell structures exhibit particle-size dependent tunable PL with narrow emission bandwidth [117].

[31] Emission collection efficiency and linewidth can be improved by using optical cavity and distributed Bragg reflectors that lead to an emission in a well-defined direction [115, 118].

Table 2.2. The main advantages and drawbacks of SPEs in various systems commonly mentioned in the literature that we overview in Section 2.2.1 [1, 9, 12, 13, 86, 108–113, 115–119].

SPE system	Advantages	Disadvantages
Spontaneous parametric down-conversion	benchmark in experiments.	non-deterministic process.
Trapped atom and ion sources	pure SPE system, narrow spectral line, SPEs are on-demand.	not optimal technology, undirected emission, low operation rates.
Organic dye molecules in nanocrystals	linearly polarized SPE, narrow spectral line, lifetime few nanoseconds, oscillator strength is unity.	low Debye-Waller factor, uncontrolled size/shape, limited photostability, PL blinking.
Quantum dots	ease of integration, SPEs are on-demand, narrow spectral line, size-tunable emission, quantum efficiency is unity.	random positioning, cryogenic temperatures, size fluctuations, non-effective emission collection.
Fluorescent defects in solids	low-cost, ease of integration, operate at RT, on-demand, occur naturally, ultra bright emission.	still unknown defects, non-effective emission collection, random positioning, sample-dependent.

fluorescent defect centers is well understood[32]. SPEs in diamonds are associated with impurities, such as nickel, silicon, germanium, carbon, chromium, and some other unknown defects [120]. Some of these fluorescent defects can occur naturally in diamond, or can be created through ion implantation and subsequent annealing. Notwithstanding, diamond defect centers present the unique advantage of photostable emission and RT operation that enables rapid characterization. Furthermore, photon generation in diamond allows for easy integration into existing networks. Despite their advantages, NV centers and other SPEs in solids have many technical challenges to overcome. First of all – a high refractive index of a host, preventing most of the fluorescent light, emitted from a defect center in a flat solid, from being collected in a confocal microscope [1, 9]. Sample-dependent results also complicate further development[33]. Symmetry of fluorescent defect is also important, e.g., lack of inversion symmetry of the NV center leads to a non-zero electronic dipole moment that causes its optical frequencies to be sensitive to local strain and electric fields. On the

[32]The most studied defect centers in diamond are NV and silicon vacancy centers, unique objects viable not only as a robust SPEs but also as a reliable spin qubits. Until now, only their crystallographic and electronic structures are well established [86].

[33]E.g. crystal growth conditions, surface treatment, irradiation, impurity content [9].

other hand, defects with an inversion symmetry are less susceptible to local environmental fluctuations [1]. While the technical challenges facing solids are substantial, the promise has already been fulfilled through a plethora of novel applications that have become possible due to the unique properties of NV centers in diamond that can simultaneously work as a magnetic field, electric field, temperature, compression, and rotation sensors [9]. The main advantages and drawbacks of different SPE systems are summarized in Table 2.2.

The study of SPEs has not been limited to diamond material. To date, defect-related SPEs have been reported in wide-bandgap semiconductors, such as in zinc oxide [11], silicon carbide [12], gallium nitride [13], aluminum nitride [14], hexagonal boron nitride [23] and other materials [1]. Most recently, it was demonstrated that carbon nanotubes at RT host SPEs[34] [121]. As we can see, at the moment, no single system meets all the requirements for ideal SPE, and the best realization is yet to emerge.

2.2.2. Single-photon emitters in hBN

The playground of solid-state SPEs has expanded beyond the originally studied QDs and fluorescent defects in wide-bandgap semiconductors to include two-dimensional (2D) materials that are better hosts for stable SPE emission and high quantum efficiency [15]. So-called 2D semiconductors are only a few atoms thin and have the natural advantages for SPE in terms of structural *openness* and light-transparency that eliminates the issues of photon extraction [16]. So far, among 2D systems hosting SPEs are molybdenum disulfide and tungsten disulfide, as well as other transition metal dichalcogenides[35] [1, 122]. However, due to smaller bandgap, the operation of all presently known SPEs in transition metal dichalcogenides is limited to cryogenic temperatures.

In 2016, hexagonal boron nitride (hBN) emerged as a compelling 2D host of SPEs that operate at room temperature [23]. In this context, it has been shown that atom-like defects in hBN create sub-bandgap electronic states in the form of single-photon sources that have narrow emission linewidth, are fully polarized, have color diversity, and show absolute photostability at and beyond RT [31, 123]. hBN has ultra-bright emission [124], which is comparable to the brightest SPEs in diamond and by far much more extensive than for QDs, furthermore, it is the highest brightness SPE reported in the visible part of the spectrum till now, as well as the highest quantum efficiency [125]. Furthermore, hBN can be grown at low cost, using conventional furnaces and precursors over large areas [126]. The majority of advantages and disadvantages of SPEs in hBN is summarized in the Table 2.3.

[34] SPEs in carbon nanotubes operate at cryogenic temperatures; they have limited photostability (suffer from blinking/bleaching) [1].

[35] The single-photon emission from atomically thin transition metal dichalcogenides originates from a bound exciton that is confined to zero dimensions by a potential field generated by local strain and/or a crystallographic defect [1].

Table 2.3. Advantages and disadvantages of SPEs in hBN commonly mentioned in the literature that we overview in section 2.2.2.

Advantages	Disadvantages
ultra-bright emission[36]	origin of the defect is unknown
high quantum efficiency[37]	ZPL broadening
temperature stability[38]	spectral diffusion[39]
easy and cheap processing	color diversity[40]
linear polarization of emission	high background emission[41]
large Debye-Waller factor[42]	random positioning

While hBN-based SPEs have shown highly desirable optical properties, one challenge has been the deterministic placement of the SPEs and control over the emission wavelength. Nevertheless, it was shown that SPEs in hBN exhibit spectral tunability if strain is applied [124]. Other advantages offered by SPEs in hBN materials include the ease with which they may be coupled to waveguides and their compatibility with other 2D materials that may be present in some complex device, e.g., photonic crystal cavity from hBN [127]. A series of experiments designed to shed light on the level structure and photo-dynamics of SPEs in hBN have been performed. The atomic structure of the quantum emitter(s) is yet to be fully understood. However, some vacancy-related defects have been proposed in literature [29]. Next, we will provide a brief review of the experimental literature on the creation and activation of SPEs in hBN.

2.2.3. Creation and activation of single photon emitters in hBN

SPEs in hBN have been observed in a range of materials, including bulk crystals [27], multilayers [128], monolayers [23], nanotubes [129] and other nanostructures (e.g., hBN nanococoons[43] [130]) as well. So far, two different types of SPEs in hBN from *unknown defects* have been observed. The first one is in the ultraviolet spectral range, i.e., at 4.1 eV [103], and the second is in the visible part of the spectrum in the vicinity of 2 eV [23]. However, this visible emission is spread over a considerable continuous spectral range. Further, to

[36] Single photon count rates of SPE in hBN exceeded 7×10^6counts/s at saturation [124], while SPE in diamond provides 3.2×10^6counts/s.

[37] Quantum efficiency of SPEs in hBN at 580 nm approaches 87±7 %. [125].

[38] Single-photon emission shows long-term stable operation up to 800 K [31].

[39] Spectral diffusion increases for larger excitation energies, publication III.

[40] SPEs in hBN span over a large spectral band, which presents a central problem for developing identical SPEs. More than 600 ivestigated SPEs in hBN exhibited narrow spectral lines distributed over a spectral range between 1.6 and 2.2 eV [123].

[41] Exfoliated hBN flakes show high background emission that reduces single-photon purity.

[42] DW$\sim$ 0.75, while NV center has DW= 0.04.

[43] hBN nanocoon is a ball-like BN allotrope that possesses a nanoscale size [130].

distinguish these two types of SPEs, we are going to refer 2 eV or 4.1 eV SPEs in hBN. Now the author will discuss the creation of 2 eV SPEs, whereas, in Chapter 5 of this Thesis, the author will perform an *ab-initio* investigation of the source responsible for 4.1 eV emission in hBN. Although the physical nature of the point defects at play in hBN remains the subject of ongoing research, the experimental recipe for creation and activation of SPEs in hBN is constantly being improved.

Two aspects are of great importance – formation and localization of defects responsible for quantum emission. Choi *et al.* demonstrated that 2 eV SPEs can be efficiently activated in as-grown hBN by electron irradiation or high-temperature annealing, i.e., typically annealing step at $800 - 850$ °C temperature in argon atmosphere is required [128]. Annealing proved to be a crucial step to ensure SPEs stability in order to avoid working with blinking emitters [26]. Additionally, the effect of high-energy electron irradiation on SPEs was investigated and shown to increase SPEs concentration in different types of exfoliated hBN flakes[44] dramatically [34]. Furthermore, this way, engineered SPEs are located throughout hBN flakes, *not only* at flake edges or grain boundaries, and do not require activation by high-temperature annealing of the host material after electron exposure [34]. On the other hand, it has been recently observed that 2 eV SPEs family in hBN tends to occur stochastically at the edges or regions of high curvature [131]. Further investigation by applying a focused ion beam to mill an array of holes into hBN, has revealed localized PL spots that matched the geometry of the patterned holes [132]. A tendency of bright emitters to appear on the perimeters of the exfoliated hBN flakes was also investigated by Chejanovsky *et al.* [26].

Subjection of the hBN flakes to the chemical etching methods appears to increase the SPEs density dramatically compared to the exfoliated flakes [26]. Quantum emitter formation probability can be increased likewise by atom/ion implantation, e.g., boron−nitrogen complexes, silicon, and oxygen ions[45], or focused laser irradiation of the as-grown material [26, 128]. It is interesting to note that the ion species had little influence on the defects formation probability, i.e., it served as an indicator that the main role of the bombarding ions is to activate already-present intrinsic point defects, rather than to introduce foreign fluorescent defects[46] [128]. However, it seems that not all ions create SPEs in hBN, e.g., optical measurement of an exfoliated hBN flake irradiated

[44] E.g. high-purity, isotopically pure and carbon-rich multilayers of hBN were investigated [34].

[45] Boron and boron-nitrogen complexes were selected to test whether the formation probability of intrinsic defects would increase, as these atoms generate mostly vacancies and interstitials. Silicon and oxygen atoms were chosen to determine whether the emitters are related to common foreign impurities [128].

[46] Quantum emitters in the implanted flakes are mostly optically stable. They do not exhibit blinking, whereas about 40% of the emitters in the reference flakes showed severe blinking and eventual bleaching, i.e., ion implantation increases photostability [128].

with helium ions and subsequently annealed in an argon atmosphere at 1000 °C has shown even lower density of SPEs in the irradiated region and PL intensity of the irradiated region was reduced five-fold compared to the non-irradiated area [124]. On the contrary, Xu *et al.* has shown that O_2 plasma-etching increases the concentration of emitters in the samples, and annealing in the air creates SPEs that exhibit intensity quenching, severe blinking, and eventual photobleaching during analysis. Additionally, the formation of new near-infrared SPEs at 1.77 eV was observed [133]. On the other hand, it was shown that carbon implantation can likewise increase formation probability of SPEs in hBN and thus Mendelson *et al.* suggested that carbon defect structure like $C_N - V_B$ should be responsible for visible spectrum SPEs [134], whereas recent *ab-initio* calculations results proposed dangling boron bonds [135], $C_B - V_N$, and $V_N - N_B$ complexes [23, 35, 36] as the likely sources of the 2 eV SPEs. On the other hand, the spatial density of SPEs increases with increasing annealing temperature in both reducing and oxidizing environments, the SPE defects, in this case, are likely to charge neutral. Furthermore, spectral features analysis of SPEs infers that there are at least two groups of defects [24].

hBN growth method plays an essential role in the mechanism of SPEs formation. It appears that for samples grown by low-pressure chemical vapor deposition, post-growth annealing is not necessary to activate or stabilize the quantum emitters, i.e., hBN already has the emitters present [136] thus it is inconsistent with previous studies. Chemical vapor deposition at sub-atmospheric pressures tends to reduce unwanted gas-phase reactions and improves film uniformity across the wafer. The density of SPEs provided by this growth method is uniform and an order of magnitudes higher, constituting a vast improvement over other available hBN growth methods. Furthermore, the emitters in these samples are not concentrated preferentially or exclusively at grain boundaries or other large scale defects as is typical of exfoliated hBN flakes[47]. This suggests an essential detail for the correct growth conditions that can affect defect formation energies, i.e., in order to get high and uniform distribution of SPEs, growth conditions should be controlled like they are controlled during low-pressure chemical vapor deposition process [136].

As we see, currently, there is a considerable controversy in the literature, and prior desperate observations have given rise to several physical models. In Chapter 3 of this Thesis, the author will investigate common impurities and native point defects in hBN in terms of *ab-initio* calculations. The results will be presented in the context of experimental work and other calculations.

[47]Tape exfoliated hBN from crystal sources results in unreliable thicknesses and highly non-uniform emitter distributions that are concentrated at flake edges, wrinkles, and grain boundaries.

Pauli's *"filthy mess"* in semiconductors

According to W. Pauli
semiconductors are a "filthy mess"[48]
and it will blight career of a Physicist
working with akin defects excess.
However, in order to achieve something,
someone must make this colossal sacrifice.
Hence, the actual responsibility of a Physicist
is to shed light on controversial results.

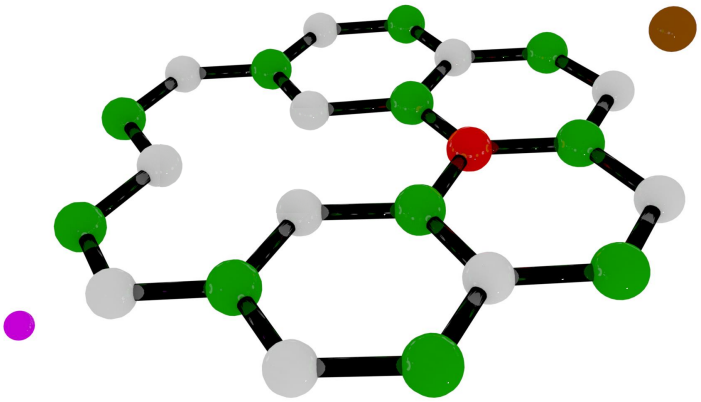

Illustration of a few common native point defects and impurities in hexagonal boron nitride.

[48]To quote a remark attributed to Wolfgang Pauli *"One should not work on semiconductors, that is a filthy mess; who knows whether they really exist."* (letter to Rudolph Peierls, 1931) [137].

Chapter 3

Native point defects and impurities in hBN

3.1. Introduction

In chapter 3, we investigate the electronic properties of native point defects along with the most common impurities in hBN. We use hybrid functionals to obtain accurate band structure for the host, as well as a reliable description of carrier localization, ensuring a correct treatment of defect physics. Furthermore, we investigate the migration properties of point defects in order to determine their kinetics at different temperatures. The information and results provided in this chapter are based on Paper I.

3.1.1. Literature review of point defects in hBN

hBN is a prominent member of the family of layered van der Waals compounds. Over the past decade, hBN has attracted considerable interest as a very versatile material that can be used in several applications due to its unique combination of physical and chemical properties [21, 138]. It is now well established that hBN has an optical band gap of 6.08 eV [18]. Recent advances in single-crystal [22], as well as in mono and multilayer growth [139–141], have led to a flurry of research on hBN as a potential material for wide-band-gap electronic and optoelectronic applications, e.g., hBN with an atomically smooth surface is as an exceptional insulating substrate for graphene electronic devices [142]. Due to large bandgap, it can be used in making deep-ultraviolet plane-emission devices [143]. Photoluminescence measurements have shown that hBN exhibits bright excitonic luminescence in the deep ultraviolet [22]. Also, hBN exhibits a rich array of sub-band-gap luminescence lines originating from recombina-

tion at point defects, i.e., native defects or impurities [144]. Point defects can have a profound impact on the electronic and optical properties of semiconductors [145], and their characterization is fundamental to understanding material properties.

Point defects may act as compensating centers that interfere with achieving *n*–type or *p*–type conductivity. For hBN, there have been very few reports of *n*–type or *p*–type doping [146, 147], and high-quality doping (with large carrier concentrations and high mobility), has not been reproducibly achieved. Recently, using *ab-initio* calculations, it was determined that silicon substituting nitrogen site results in too deep acceptor levels for *p*–type doping, on the other hand, beryllium and magnesium substituting boron site do not give impurity states in the bandgap, thus it is unlikely that any shallow acceptor state can be formed in hBN [148]. Point defects can also act as recombination centers (both radiative and non-radiative), reducing the efficiency of bandgap luminescence [149].

As we discussed earlier in Chapter 2, the recent discovery [23,123] that hBN can host bright and stable SPEs in the visible and ultraviolet spectral ranges has sparked tremendous interest in the application of hBN as a light source in quantum optics applications. In a series of papers, Tran *et al.* identified SPE from color centers in irradiated or annealed hBN emitting at energies between 1.6 and 2.2 eV [23, 24, 150]. Subsequent experiments have reported a broad range of color centers exhibiting SPE with ZPL in this energy range and widely varying vibronic properties [25, 44], see paper III.

As-grown hBN frequently exhibits deep-level luminescence with a ZPL at 4.1 eV [151–155] and relatively weak coupling to bulk phonon modes (Huang-Rhys factor $S = 1.3$ [153]), furthermore 4.1 eV luminescence exhibits single-photon emission [103]. This emission has typically been associated with the acceptor level of a C impurity substituting N atom (C_N) [151, 154].

Despite the obvious technological importance, the precise chemical nature of the dominant point defects in hBN remains unclear, as this is extremely difficult to characterize experimentally. A number of previous studies have addressed native point defects or impurities in hBN using *ab-initio* calculations [156–160]. However, these studies all had shortcomings, such as being based on less accurate functionals, not considering all possible spin configurations, or not including proper finite-cell-size corrections.

In summary, an accurate and comprehensive picture of the defect chemistry in hBN is still not available. Consequently, this chapter is dedicated to the investigation of common impurities and native point defects in hBN in terms of *ab-initio* calculations.

3.2. Methodology

3.2.1. Computational details

We perform calculations using DFT within the generalized Kohn-Sham scheme [55], using the screened hybrid functional of Heyd, Scuseria, and Ernzerhof (HSE) [62, 161]. In this approach, the short-range exchange potential is calculated by mixing a fraction of nonlocal Hartree-Fock exchange with the generalized gradient approximation of Perdew, Burke, and Ernzerhof (PBE) [63]. The screening parameter is set to 0.2 Å^{-1}, and the mixing parameter to $\alpha = 0.31$. This value of α is similar to that used to study GaN and AlN [162]. A correction for the van der Waals interactions is included within the Grimme-D2 scheme [163]. The valence electrons are separated from the core by use of projector augmented wave (PAW) potentials [164] as implemented in VASP [165]. For the present calculations, B $2s^2 2p^1$, N $2s^2 2p^3$, C $2s^2 2p^2$, O $2s^2 2p^4$, and H $1s^1$ electrons are treated as valence. For the bulk hBN primitive cell, we use a $9 \times 9 \times 3$ **k**-point grid for integrations over the Brillouin zone; for the larger supercells, we use a Γ-point ($\mathbf{k} = 0$). Energy cut off of 500 eV is used for the plane-wave basis set. Spin polarization was taken into account.

Defect calculations were performed in orthorhombic supercells containing 240 atoms sites, with lattice vectors $5(\mathbf{a} + \mathbf{b})$, $3(\mathbf{a} - \mathbf{b})$, and $2\mathbf{c}$, where $\mathbf{a}$, $\mathbf{b}$, and $\mathbf{c}$ are lattice vectors of the primitive hBN lattice. The supercell lattice vectors are fixed to the HSE calculated equilibrium values[49]. Native defects and impurities are created by adding and removing atoms from the supercell, and the internal coordinates are relaxed until all forces are less than 0.01 eV/Å. The same computational set of parameters and supercells was used in Chapter 4 and Chapter 5.

3.2.2. Formation energies

The likelihood of incorporating a defect can be determined by calculating the formation energies, i.e., the energies that are required to create a defect in a solid. We use established methodologies for evaluating defect formation energies and transition levels based on total energy calculations within the supercell approach [83, 166]. For a defect D with charge state q, the formation energy $E^f[D^q]$ is calculated as

$$E^f[D^q] = E_{\text{tot}}[D^q] - E_{\text{tot}}[\text{hBN}] - \sum_i n_i \mu_i + q E_F + \Delta^q, \tag{3.1}$$

[49] It should be noted that defect and impurity calculations are performed using bulk-unit-cell optimized theoretical lattice constant. This is essential to avoid spurious elastic interactions with defects or impurities in the neighboring supercell. If the defect-containing supercell's volume is relaxed (in addition to relaxing the positions of the atoms in proximity to the defect), the calculation will correspond to finding the lattice parameter of the system containing an ordered array of defects at a high concentration [82].

where $E_{\text{tot}}[D^q]$ is the total energy of the supercell containing D^q, and $E_{\text{tot}}[\text{hBN}]$ is the total energy of the defect-free supercell. The number of atoms that are added ($n > 0$) or removed ($n < 0$) to/from the supercell is n_i, where i is the type of the atom, and the chemical potential μ_i represents the energy of the reservoir with which the atomic species are exchanged[50]. The electron chemical potential is given by the position of the Fermi level (E_F), taken with respect to the valence-band maximum (VBM). Finally, Δ^q is a charge-state dependent term that corrects for the finite size of the supercell [167, 168].

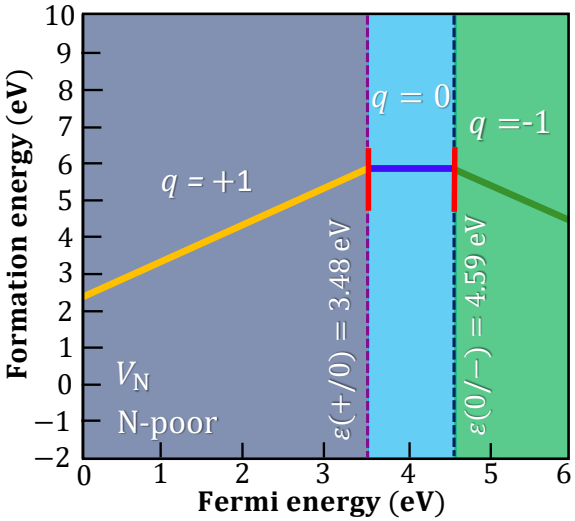

Figure 3.1. Formation energy of nitrogen vacancy (V_N) in hBN as a function of Fermi level under N-poor conditions is given as an example (calculated in this Thesis). The slope of each line segment corresponds to the charge state, according to equation 3.2. The colored region each represent the most stable charge state at a given Fermi level, and the vertical dotted lines show the transitions between different charge states. In this case, the defect exhibits two charge-state transition levels, the $q = +1$ state is stable only for up to 3.48 eV value of the Fermi level, while the neutral state is most stable from 3.48 eV to 4.59 eV. If the Fermi level is higher than that, the $q = -1$ charge state is most stable.

The defect charge-state transition level $\varepsilon(q/q')$ is defined as the Fermi-level position below which the defect is stable in charge state q, and above which it is stable in charge state q'. It is calculated as

$$\varepsilon(q/q') = \frac{E^f(D^q; E_F = 0) - E^f(D^{q'}; E_F = 0)}{q' - q}, \tag{3.2}$$

[50]The formation energy of bringing an impurity to a substitutional site is separated into two processes, removal of a host atom and the incorporation of the impurity atom [83, 166].

where $E^f(D^q; E_F = 0)$ is the formation energy of D^q when the Fermi level is at the VBM (i.e., for $E_F = 0$). Defect charge-state transition levels represent the physical situation in which one defect charge state can fully relax to its equilibrium configuration after a charge-state transition such as in deep level transient spectroscopy, i.e., charge-state transition levels determine how a defect will behave electrically [83].

3.2.3. Chemical potentials

By varying the chemical potentials μ_i in the calculation, different experimental conditions can be explored[51]. Upper and lower bounds are given by the stability of the phases that constitute the reservoir, which is expressed by the thermodynamic stability condition [83]. For the calculations in this Thesis, μ_B is referenced to the total energy of a single atom in solid-phase B, and μ_N is referenced to the total energy of an N atom in an N_2 molecule; we define here $\Delta\mu_N$ and $\Delta\mu_B$ with respect to these energies. Bounds are placed on the $\Delta\mu$ values based on the stability condition for hBN. In thermodynamic equilibrium B and N are linked by the stability of the hBN phase

$$\Delta\mu_B + \Delta\mu_N = \Delta H^f(\mathrm{BN}), \tag{3.3}$$

where $\Delta H^f(\mathrm{BN})$ is the enthalpy of formation for hBN. Equilibrium with N_2 sets an upper bound on μ_N (N-rich conditions): $\Delta\mu_N = 0$. Equation 3.3 then yields $\Delta\mu_B = \Delta H^f(\mathrm{BN})$ in the N-rich limit. We can also assign N-poor limit, with $\Delta\mu_N = \Delta H^f(\mathrm{BN})$ and $\Delta\mu_B = 0$. The HSE-calculated value for $H^f(\mathrm{BN})$ is -2.90 eV, in reasonable agreement with the experimental value of -2.6 eV [169]. Neither N-rich nor N-poor conditions realistically represent actual growth conditions, but they serve as limiting cases.

When impurities are present, their chemical potentials are subject to similar bounds, i.e., secondary phases may have to be taken into account [83]. We assigned chemical potentials to the C, H, and O impurity species. The upper limit of the chemical potential for the different species is given by their total energy, μ_C is referenced to the total energy of a C atom in a diamond. For μ_H and μ_O, the diatomic molecules H_2 and O_2 are used as a reference. The high stability of B_2O_3 imposes an additional upper bound on μ_O

$$2\Delta\mu_B + 3\Delta\mu_O \leq \Delta H^f(\mathrm{B_2O_3}), \tag{3.4}$$

where we have calculated $\Delta H^f(\mathrm{B_2O_3}) = -12.69$ eV.

For oxygen on a nitrogen site, for example, the removed nitrogen atom has to be brought to a reservoir where it has the energy μ_N. If this energy is high (nitrogen-rich environment), the formation energy will be high as well. The

[51] In the general formalism, chemical potentials μ_i are regarded as variables [83].

upper limit of the chemical potential of the impurity may be determined by the formation of its bulk component, but potentially also of a compound with one of the elements of the host. For oxygen, e.g., the chemical potential is limited by the formation of boron oxide (B_2O_3).

3.2.4. Electrostatic corrections

Coulomb interaction is long-range, and the unphysical interaction with the image charge due to finite supercell may need a proper correction[52]. As already mentioned in section 3.2.2, for well-localized defects within the supercell, we use the correction scheme proposed by Freysoldt *et al.* to correct for the electrostatic interaction between the charged defect and its images, and a potential alignment term caused by the introduction of the defect [83, 167, 168]. The full Freysoldt correction may be expressed as

$$E_{\mathrm{corr}} = E_{\mathrm{lat}} - q\Delta V_{q/b}. \tag{3.5}$$

Correction for the interaction between the periodic images of the charge is E_{lat}, i.e., Madelung energy for a periodic array of point charges immersed in a compensating background. The correction for the band shift is $q\Delta V_{q/b}$. Correction for the interaction between the periodic images of the charge E_{lat} is calculated by weighing the electrostatics of a model charge distribution, which is fitted to the actual calculation by the studied defect, and comparing the potential in the periodic cell with the potential where the boundary conditions are not periodic [168]

$$E_{\mathrm{lat}} = \int_{\Omega} \left[\frac{1}{2} q(\tilde{V}_q^{\mathrm{lr}} - V_q^{\mathrm{lr}}) \right] d^3r. \tag{3.6}$$

The integral in equation 3.6 is carried out over the simulation cell. The factor $\frac{1}{2}$ is required to remove the double counting [170]. V_q^{lr} is the long-range potential of the model charge distribution and $\tilde{V}_q^{\mathrm{lr}}$ is the corresponding quantity in the periodic cell are shown in Fig. 3.2, red line. The second term removes the electrostatic interaction energy of the model charge with itself, that is contained in the first term [168]. The potential alignment-like term $\Delta V_{q/b}$ can be expressed as:

$$\Delta V_{q/b} = \tilde{V}_{q/b} - \tilde{V}_q^{\mathrm{lr}}, \tag{3.7}$$

where $\tilde{V}_{q/b}$ is the difference between the electrostatic potential in the pristine bulk configuration and with the defect added are shown in Fig. 3.2, grey line. $\Delta V_{q/b}$ is violet in Fig. 3.2, and should be evaluated at a place far from the defect in the supercell to get the correct offset in the zero-point reference energy

[52] Periodic translation of the supercell allows defects to interact with their own images in the neighboring cells of the simulation.

(region in the plot near the right and left edges). An obtained difference is defined between two screened potentials. The static dielectric constant describes the dielectric screening[53], i.e., for hBN, we take a mean value between perpendicular and parallel dielectric constants for $\omega = 0$, $\varepsilon_{\text{aver}} = 5.5$. For example, electrostatic potentials (averaged over the xy plane) for C_B^+ in hBN supercell are presented in Fig. 3.2.

According to Komsa *et al.* [170], for well-localized defects, the Freysoldt approach simplifies to sum of Madelung and potential alignment. The software to compute the corrections, used in this Thesis, is available online[54].

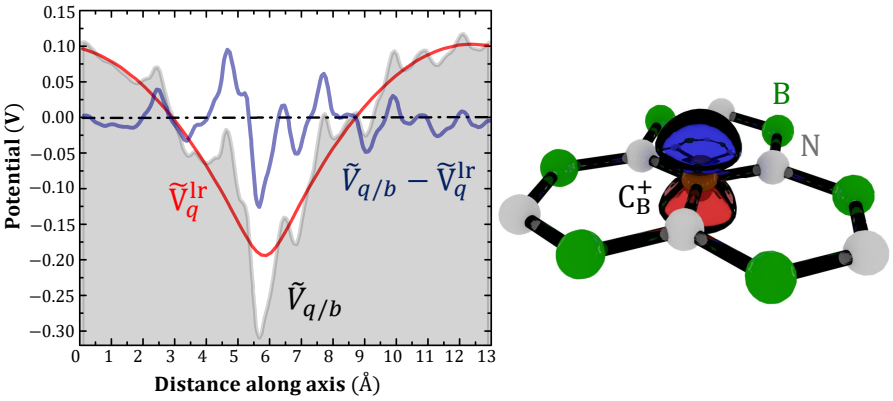

Figure 3.2. Electrostatic potentials (planar-averaged) for C_B^+ in hBN supercell. The defect is located at 5.68 Å on the axis, i.e., in the center of the supercell. Periodic images of the defect are distributed at the distance 12.939 Å along x, 12.450 Å along y and 13.108 Å along z directions. As we see, the final correction for $q = +1$ is $E_{\text{corr}} = 0.31$ eV.

3.3. Results and Discussion

3.3.1. Structural and electronic properties of bulk hBN

The symmetry of the hBN crystal has a space group $P6_3/mmc$ and point group D_{6h}. Within the (0001) plane, each nitrogen atom is threefold coordinated to boron and vice versa, in a honeycomb pattern that is a result of sp^2 bonding. The in-plane B—N bond length is calculated to be 1.44 Å. Out of the plane, hBN exhibits AA′–type stacking with alternating B and N atoms along the [0001] direction. The interlayer separation is determined by the van der Waals interaction and calculated to be 3.28 Å.

[53]The Freysoldt correction does not work perfectly in all cases, the long-range potential is overestimated in in-plane directions and underestimated in out-of-plane direction; it is caused by the application of average dielectric constant.

[54]URL https://sxrepo.mpie.de/.

Calculated band gaps and lattice constants are presented and compared with the experiment in Table 3.1. The experimental geometry is clearly very well reproduced within *ab-initio* calculations.

Table 3.1. Bulk properties of hBN. The present HSE-calculated results are compared with experimental values.

Parameters	a, Å	c, Å	E_g^{ind}, eV	E_g^{dir}, eV
Thesis	2.49	6.55	5.94	6.42
Experiment	2.50 [171]	6.65 [171]	6.08 [18]	6.40 [172]

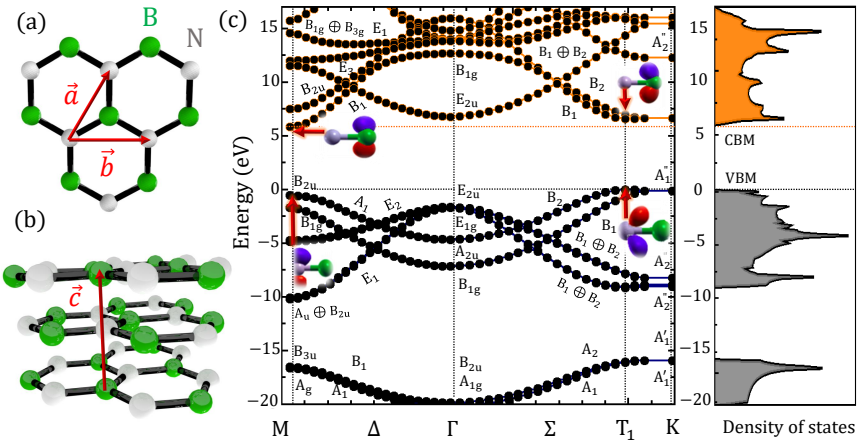

Figure 3.3. (a) Top-down view of the in-plane honeycomb structure of hBN, (b) side view showing the interlayer spacing and AA′ stacking, (c) *ab-initio* results for band structure and the corresponding electronic density of states of hBN. Electronic band structure plotted along a high-symmetry path in the Brillouin zone. The energy of the highest occupied valence state is set to zero. The VBM is at the T_1 point, and the CBM is at the M point. Sharp peaks in density of states represent van Hove singularities.

The calculated electronic band structure for hBN is plotted in Fig. 3.3 (c). The valence-band maximum (VBM) is derived from π–bonding states with mostly N $2p_z$ character; the conduction-band minimum (CBM) is derived from π^*–antibonding states with mostly B $2p_z$ character (see Fig. 3.3 (c) inserted orbitals). The VBM is found at the so-called T_1 point near K (between Γ and K); the CBM is at the M point. The indirect fundamental bandgap is 5.94 eV; the lowest direct gap is 6.42 eV at the M point. As shown in Table 3.1, the calculated fundamental indirect bandgap is close to the experimental value of

6.08 eV[55] [18]. The HSE calculated band gaps are also in agreement with the quasiparticle gaps of Arnaud *et al.* based on GW calculations [174].

In the electronic density of states, the appearance of van Hove singularities is observed (Fig. 3.3 (c)). Certain van Hove singularities are a consequence of crystal symmetries, others do not follow from symmetry and are therefore called accidental. Van Hove singularities usually are related to high-intensity features in absorption or emission spectra [175].

3.3.2. Electronic properties of native point defects in hBN

In this section, we will discuss electronic properties of native defects in hBN, namely boron vacancy (V_B), nitrogen vacancy (V_N), boron antisite ($\mathrm{B_N}$), nitrogen antisite ($\mathrm{N_B}$), boron interstitial (B_i), and nitrogen interstitial (N_i), see Fig. 3.4, in terms of charge-state transition levels, which are represented in Fig. 3.6.

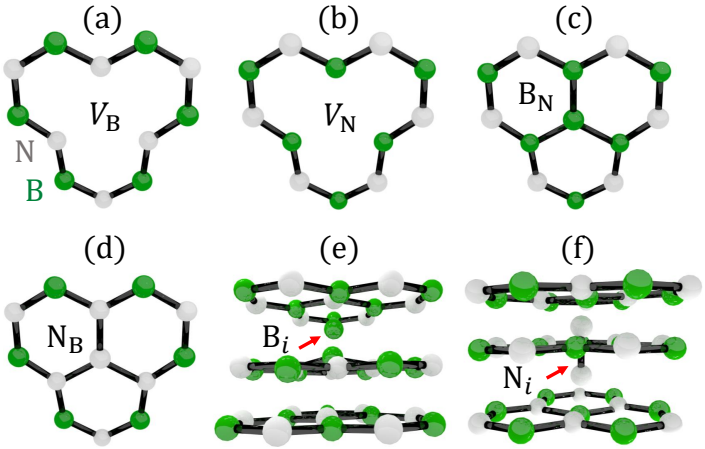

Figure 3.4. Native point defects in hBN: (a) boron vacancy (V_B), (b) nitrogen vacancy (V_N), (c) boron antisite ($\mathrm{B_N}$), (d) nitrogen antisite ($\mathrm{N_B}$), (e) boron interstitial (B_i) and (f) nitrogen interstitial (N_i) in neutral charge state. Atom colors: B (green), N (white).

Boron vacancy (V_B). Each boron in the hBN lattice has three nearest-neighbor nitrogen atoms. Removing the boron atom leaves three N $2sp^2$ and three N $2p_z$ dangling bonds. These dangling bonds combine to form localized symmetric (a_1', a_1'') and higher-lying antisymmetric (e', e'') molecular orbitals,

[55] It is interesting to note that DFT predicted the monolayer to have a direct bandgap of 6.47 eV, with a cross-over to indirect band gaps occurring at two layers. This direct-to-indirect transition to be driven by a shift in the conduction-band minimum at the M point; this shift changes the bandgap by 0.5 eV, going from a single monolayer to bulk [173].

see Fig. 3.5 (the orbitals labeled according to the irreducible representations of the D_{3h} point group). The defect states of V_B are largely derived from valence-band orbitals. Electron counting indicates that the defect can accept up to three electrons, i.e., V_B is, in principle, a triple acceptor. In the neutral charge state, three holes appear in the high-lying e' and e'' states of the minority spin channel, corresponding to a high-spin (HS) $S = 3/2$ paramagnetic state. V_B was previously reported to possess a low spin (LS) ground state, based on calculations within the local density approximation (LDA) [176]; in our HSE calculations (which treat exchange more accurately, particularly for highly localized states [177]), the HS–LS energy splitting is 0.8 eV, showing the HS state is strongly favored. The charge-state transition levels are plotted in Fig. 3.6, they induce significant distortions in the local geometry around the defect. When the Fermi level is near the VBM, V_B is stable in the neutral charge state. With increasing Fermi level, V_B transitions into a $q = -1$ charge state; for yet higher values of the Fermi level, the $q = -2$ charge state is stabilized. The transition levels are all found at a large energy from the VBM, making V_B a very deep acceptor. The $q = -3$ charge state is found not to be stable.

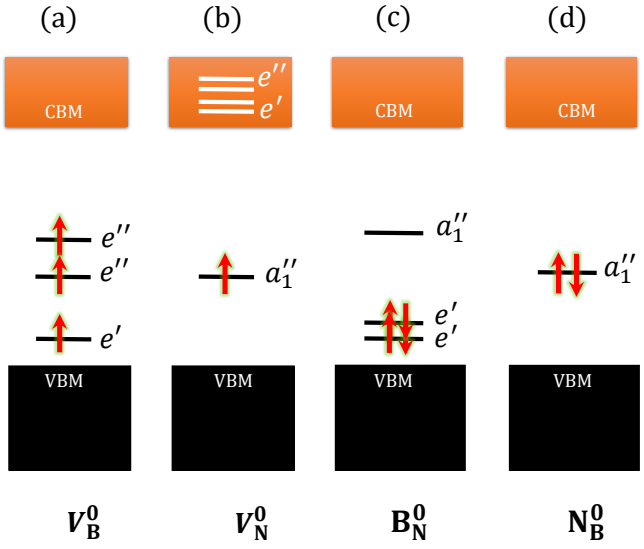

Figure 3.5. Schematic diagram of Kohn-Sham states of (a) V_B, (b) V_N, (c) B_N, (d) N_B in neutral charge state. The orbitals labeled according to the irreducible representations of the D_{3h} point group for V_B, V_N, B_N, N_B.

Nitrogen vacancy (V_N). The removal of an N atom from the hBN lattice leaves three B $2sp^2$ and three B $2p_z$ dangling bonds, and, as with V_B, these combine into low-lying a states and higher-lying e states. The V_N defect states

are largely derived from conduction-band orbitals. Electron counting indicates that in the neutral charge state, three electrons occupy the lowest a_1' and a_1'' defect orbitals. In the neutral charge state, there exists only one gap state that is singly occupied, with $S = 1/2$. This state can, therefore, either donate or accept a single electron; V_N acts as both a donor and an acceptor. As shown in Fig. 3.6, the $(+/0)$ and $(0/-)$ levels of V_N lie deep in the band gap. Both the $q = +1$ and $q = -1$ charge states are nonmagnetic.

Boron antisite (B_N). A boron atom can substitute for a lattice N atom to form an antisite defect B_N. In this case, gap states form from the localized B−B bonds. Boron has two fewer valence electrons than nitrogen, so in the neutral charge state, this defect introduces two holes, both of which occupy the highest defect state, resulting in a nonmagnetic ground state ($S = 0$). As neutral B_N introduces occupied and unoccupied gap states, this defect can act as both a single donor and acceptor, with higher charge states not being stable. The $(+/0)$ and $(0/-)$ levels are indicated in Fig. 3.6. Both the $q = +1$ and $q = -1$ charge states have $S = 1/2$.

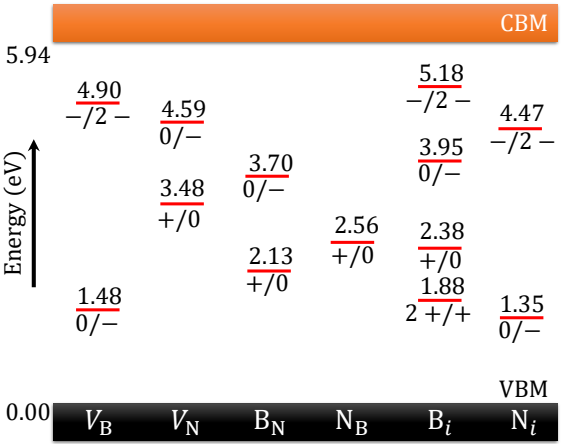

Figure 3.6. Charge-state transition levels for native point defects in hBN.

Nitrogen antisite (N_B). The N_B defect forms when an N atom substitutes for a lattice B atom, leading to the formation of N–N bonds. The N atom has two extra valence electrons when compared to B, and these electrons fill the lowest unoccupied N_B defect state in a nonmagnetic ($S = 0$) configuration. Removing an electron from this defect orbital results in a positively charged state with $S = 1/2$. We find that a $q = +2$ state is never stable. The $(+/0)$ level occurs around midgap, at 2.56 eV, Fig. 3.6.

Boron interstitial (B_i). Given the layered nature of hBN, the interstitial is essentially intercalated. The B atom can be seen to sit between the layers in Fig. 3.4. When a B atom is present at the intercalated site, a large number of gap states associated with the atomic levels of the B atom appear. The B_i defect can act as a donor, with the $q = +1$ and $q = +2$ charge states becoming stable when the Fermi level moves closer to the VBM. B_i can also act as an acceptor when the Fermi level is closer to the CBM, stabilizing the $q = -1$ and $q = -2$ charge states. All of the charge-state transition levels for B_i are presented in Fig. 3.6.

Nitrogen interstitial (N_i). Unlike B_i, which forms at an intercalated site, N_i prefers to incorporate in a split-interstitial configuration, in which it forms a covalent bond with a lattice N atom. The result is similar to an N_2 molecule substituting on an N site. This defect introduces unoccupied gap states, which are essentially the antibonding states of the N_2 molecule; consequently, N_i behaves as an acceptor, with $q = -1$ and $q = -2$ charge states being stable. A positive charge state for this defect was not stable.

3.3.3. Formation energies of native point defects in hBN

In thermodynamic equilibrium, the concentration of a defect N is determined by the formation energy according to a Boltzmann expression

$$N = N_{\text{sites}} \exp\left(-\frac{E^f[D]}{k_B T}\right), \tag{3.8}$$

where N_{sites} is the concentration of sites[56] on which the defect can form, $E^f[D]$ is the formation energy from equation 3.1, k_B is the Boltzmann constant, and T is the temperature. If conditions are close to equilibrium (which is the case in high-temperature growth or annealing), only defects with a sufficiently low formation energy will be present in large concentrations. In this Thesis, we consider temperatures in the range $700 - 1300$ K, which are typical for chemical vapor deposition of hBN [24, 140, 141]. Bulk growth is performed at higher temperatures, but defect equilibria are probably established at lower temperatures during cooldown. Because of the exponential dependence on formation energy, defect concentrations are insignificant unless the formation energy is below 2.6 eV when $T = 1300$ K or below 1.4 eV when $T = 700$ K. The formation energies for native point defects in hBN are plotted in Fig. 3.7, for chemical potentials corresponding to N-rich and N-poor conditions.

N-rich conditions in Fig. 3.7 (b), (d) and (f). In N-rich conditions among native point defects, N_B and N_i, have the lowest formation energies. The formation energies of these defects depend on the Fermi level and the Fermi level, in turn, is determined by charge neutrality. In the absence of any impurities in

[56] $N_{\text{sites}} = 5.7 \times 10^{22}$ cm^{-3} for substitutional sites in hBN.

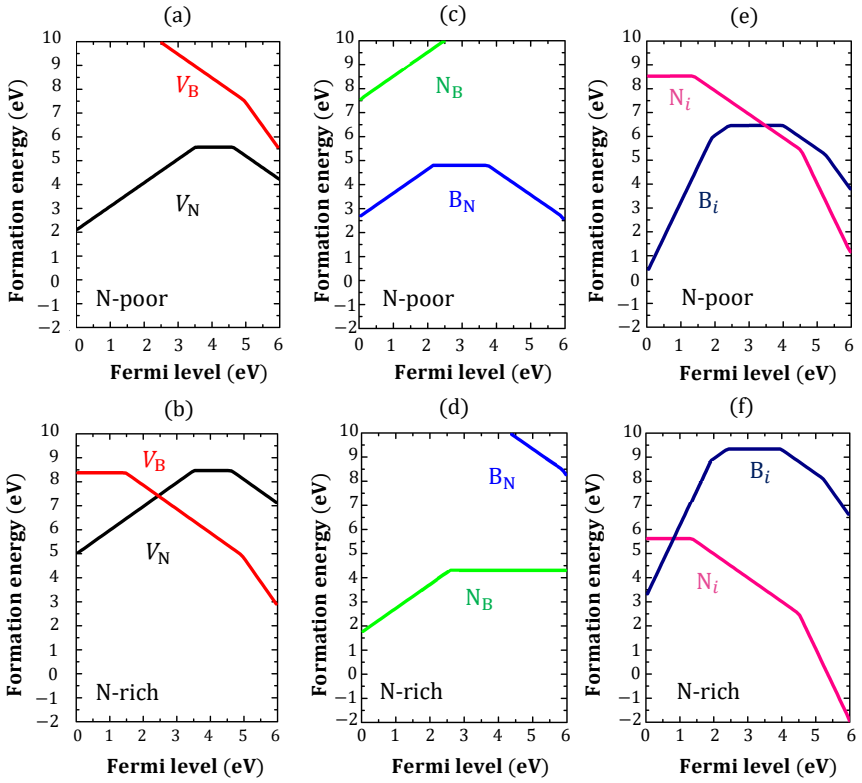

Figure 3.7. Formation energies of native point defects in hBN as a function of Fermi level under N-poor (a, c, e) and N-rich (b, d, f) conditions.

hBN, the Fermi level would be pinned at the value for which the concentrations of positively and negatively charged point defects are equal, i.e., at the crossing point in the formation-energy curves. The crossing point of N_B and N_i defects will be at 2.18 eV above the VBM. At this point, the formation energy of N_B and N_i is $E^f = 4.46$ eV, an extremely large value leading to negligible concentrations of these defects. This implies that the Fermi level is more likely to be determined by impurities incorporated into the hBN material. Depending on the impurity, the Fermi level would shift closer to the VBM or the CBM, favoring either N_B or N_i, which would act as compensating centers.

N-poor conditions in Fig. 3.7 (a), (c) and (e). In N-poor conditions, the lowest energy native point defects are B_i, V_N, B_N, and N_i. In the absence of impurities, the Fermi level would again be pinned around the mid-gap, where the formation energy of the point defects is around $E^f = 5$ eV. Again, this indicates a negligible native defect concentration, and points to the role of impurities in determining the Fermi level of hBN. Several authors have sug-

gested that vacancy and antisite complexes play a role in the defect chemistry of hBN [23, 178]. Zobelli *et al.* investigated $V_B - V_N$ vacancy complexes in the context of defect migration [178]. However, we find that the neutral $V_B - V_N$ complex has a formation energy of 10.05 eV; consideration of other charge states does not significantly lower the energy of the defect. Tran *et a*l. proposed that a neutral $N_B - V_N$ complex could act as a color center in hBN and account for single-photon emission [23]. Again, such a complex has a very high formation energy equal to 8.15 eV under the most favorable combination of chemical potentials, and considering other charge states did not substantially lower the energy of the complex. We can conclude that vacancy and antisite complexes are unlikely to play a role in hBN.

Summarizing this section, we can conclude that native point defects in hBN tend to have very high formation energies, and, in the absence of impurities, will not form in large concentrations under thermodynamic equilibrium.

3.3.4. Migration properties of native point defects in hBN

The population of native point defects will be in equilibrium if the relevant migration barriers are low enough to allow efficient motion of the defects at a given temperature. By determining the migration barrier E_{mb} for a native point defect, we can estimate the temperature at which the defect becomes mobile. Above this temperature, the system can be considered to be in equilibrium, at least concerning that particular defect, since it would not be possible to maintain a nonequilibrium concentration of the defect.

Knowledge of this *annealing temperature* is useful for various purposes. It allows assessing whether a given growth temperature is high enough for the assumption of thermodynamic equilibrium to be valid in the determination of point-defect concentrations. In situations where nonequilibrium concentrations of point defects might be present, for instance, due to low-temperature growth, or due to intentional damage caused by, e.g., irradiation, the annealing temperature indicates at what temperature the point-defect concentration would return to equilibrium. Within transition state theory [179], the rate Γ at which a defect hops to a neighboring equivalent site can be expressed as

$$\Gamma = \Gamma_0 \exp\left(-\frac{E_{mb}}{k_B T}\right). \tag{3.9}$$

The prefactor Γ_0 is related to a typical phonon frequency; in hBN, this can be taken as approximately 10^{14} s^{-1} [180]. An estimate for the annealing temperature can then be obtained as the temperature at which the rate $\Gamma = 1$ s^{-1} [181]. We note that the annealing temperature is not very sensitive to the choice of phonon frequency used as the prefactor in equation 3.9.

Vacancy migration. Our potential energy surfaces for the migration of V_B and V_N in the neutral charge state, calculated using the climbing-image nudged-elastic-band method [182, 183], are shown in Fig. 3.8. The paths and migration barriers for the neutral charge state are similar to those reported by Zobelli *et al.* [178]. Here we have extended the migration study to include other charge states of the vacancies. In Table 3.2, the migration barriers for each of the stable charge states of V_B and V_N are presented, along with their annealing temperature. For V_B, the neutral charge state has a migration barrier of 2.78 eV. There exists some variation between charge states, but E_{mb} is relatively similar, and the annealing temperatures for these defects are around 1000 K (i.e., 727°C). We can, therefore, assume that the concentration of V_B is likely to be in equilibrium when hBN is grown or annealed at temperatures above 1000 K. However, V_B is *frozen in* when generated at room temperature, e.g., by electron or ion irradiation. Indeed, hBN samples exposed to irradiation have been reported to exhibit V_B defects as well as larger V_B-related defect structures [184–186]. High-resolution transmission electron microscopy has revealed peculiar triangle-shaped multivacancy structures. The plethora of unusual large defects that were observed is a consequence of the rather severe reactive ion etching process used to thin the sample. Also, it was observed that the electron beam itself creates vacancies through knock-on damage [186, 187].

Table 3.2. Migration barriers (E_{mb}) for vacancy and interstitial defects in hBN. The charge state q is indicated, and the annealing temperature T_{an} is presented, as calculated using equation 3.9 assuming a hopping rate of 1 s^{-1}.

Defect	q	E_{mb} (eV)	T_{an} (K)	Defect	q	E_{mb} (eV)	T_{an} (K)
V_B	0	2.78	1000	V_N	1+	5.51	1980
	1−	3.09	1110		0	5.00	1800
	2−	2.33	840		1−	6.05	2180
B_i	2+	0.81	290	N_i			
	1+	1.08	390		0	0.83	300
	0	0.51	180		1−	1.00	360
	1−	1.05	380		2−	0.88	320
	2−	0.54	190				

For V_N, the migration barriers are much larger; in the neutral charge state $E_{mb} = 5$ eV. This energy corresponds to the largest barrier the defect needs to overcome along its migration path, see Fig. 3.8. Metastable sites exist along the path, and additional barriers occur to escape out of those sites, but those intermediate barriers, on the order of 2.5 eV, are not rate-limiting. The other charge states exhibit even larger barriers. These barriers are larger than vacancy migration barriers in graphite [188]. This can be attributed to the need for atoms to move between second-nearest-neighbor sites in hBN, as opposed to

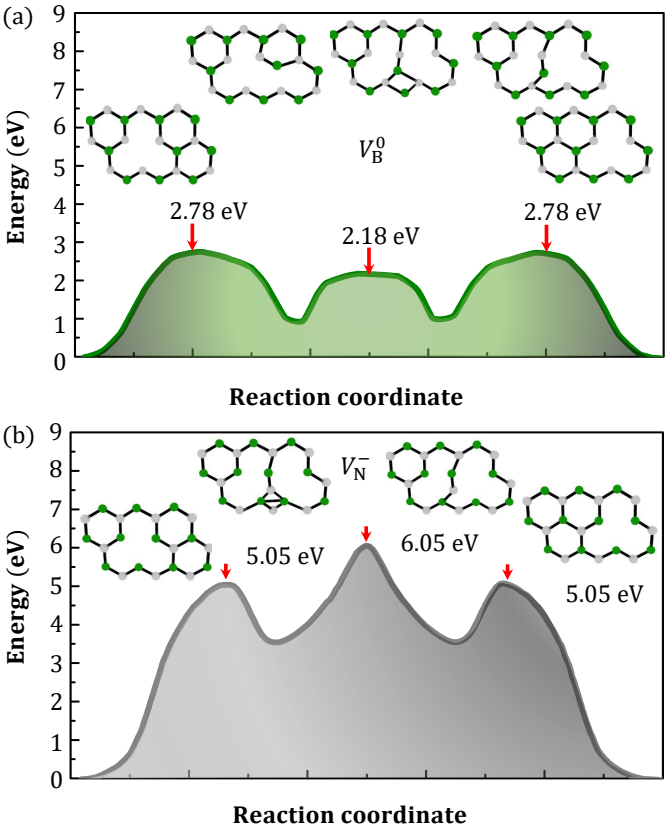

Figure 3.8. Calculated potential energy surfaces for migration of the (a) neutral V_B and the (b) charged V_N in hBN. Structural configurations along the reaction paths are depicted above, respectively.

first-nearest-neighbor motion in graphite. Because of the high barriers, these defects do not become mobile until temperatures around 2000 K, much higher than typical growth and annealing temperatures [24, 140, 141], suggesting they can be present in nonequilibrium concentrations when prepared or processed under certain conditions. We note that the growth of single crystals by the high-pressure high-temperature technique is performed at temperatures as high as 2000 K [22].

Interstitial migration. The small barrier in the potential energy surface is associated with a reorientation of the B atom with respect to the atoms in the surrounding layers; this barrier is easily overcome, but this step is necessary for long-range migration. The larger barrier originates from traversing the B−N bond length to a neighboring site; even the larger barrier is shallow, at 0.51 eV. For N_i, the barrier is related to breaking the N−N bond at the split-interstitial

site; the N_i atom moves into the interplanar region and then to a neighboring N atom, reforming an N−N bond. The barrier for this process is again very modest, only 0.83 eV. The migration barriers for each of the stable charge states of B_i, listed in Table 3.2, are quite low, indicating that interstitial B atoms can move very freely in between the hBN layers. The annealing temperatures in Table 3.2 indicate that B_i is mobile at temperatures close to room temperature. This makes it unlikely that B_i would be present as an isolated defect: B_i will move around until it is annihilated, e.g., at a vacancy or step edge, or until it can lower its energy by forming a complex with another defect. Similar arguments apply to N_i: the migration barriers are low for all charge states, and N_i is very unlikely to be present as an isolated defect. Table 3.2 shows that, for a given defect, there is no systematic trend in migration barriers as a function of the charge state. We attribute this to the fact that migration paths and barriers are governed by local bonding, which depends on the local electronic and spin state of the defect. The occupation of defect levels in the gap affects the strength of bonding, and the defects levels and the electronic structure change as the defect moves along the migration path. These properties are charge-state dependent, and hence do not necessarily follow simple trends. We have also examined the migration of antisites, but all possible paths lead to very high migration barriers.

Summarizing this section, we can conclude that interstitial defects are more likely to form when the Fermi level is closer to the band edges, which would occur when dopant impurities are present. Under those conditions, the interstitials will act as compensating centers, occurring in a charge state opposite to that of the dopant, and they would be Coulombically attracted to the impurities and possibly form a complex.

3.3.5. Formation energies of impurities in hBN

Due to the high formation energies of the native point defects, impurities are expected to play a dominant role in the defect chemistry. Certain impurities are likely to be present unintentionally in the growth environment, and it is important to assess whether they can be incorporated during growth. Carbon and oxygen impurities have been found to be present in III-nitrides [189, 190], e.g., in GaN [191], AlN [192], as well as BN [193]. Hydrogen is also a ubiquitous impurity, and it is often part of the growth process: for growth of hBN by chemical vapor deposition, hydrogen-containing precursors such as borazine ($N_3H_3B_3H_3$) [140] or ammonia borane (NH_3BH_3) [141] are used. Our calculated formation energies for the various impurities, as well as likely complexes, are shown in Fig. 3.9. The charge-state transition levels are shown in Fig. 3.10. Comparing Fig. 3.9 with Fig. 3.7 immediately shows that impurities can have far lower formation energies than native point defects.

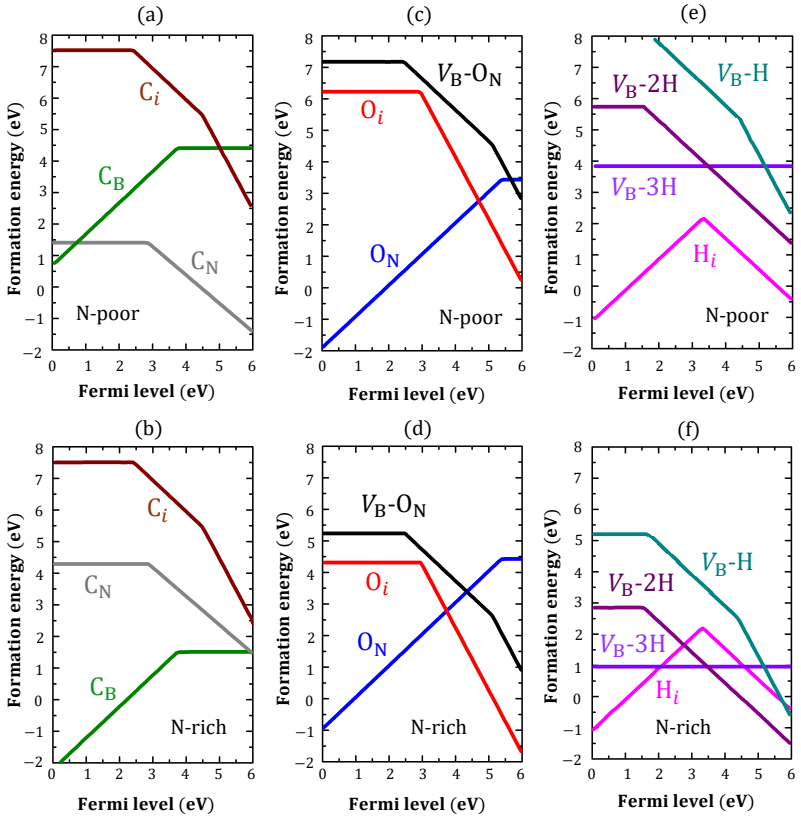

Figure 3.9. Formation energies of impurity-related defect centers in hBN as a function of Fermi level in N-rich and N-poor conditions for C impurities (a, b), O impurities (c, d), and H impurities (e, f).

Carbon impurities. For carbon, we investigate substitution at either a B or an N site (C_B; C_N). Based on the formation energies, Fig. 3.9 (a, b), it is clear that substitutional carbon is easily incorporated. C_B is most favorable under N-rich conditions, and acts as a donor; the (+/0) level is at 3.71 eV above the VBM (Fig. 3.10). Under N-poor conditions, C_N is dominant; this is an acceptor type defect with a (0/−) level 2.84 eV above the VBM. For the case of C_B, localized C–N bonding and antibonding states form. In the neutral charge state, C_B introduces one excess electron, and this occupies an antibonding-like state in the bandgap, resulting in a paramagnetic $S = 1/2$ center. The defect state is derived from C and N $2p_z$ orbitals. In the $q = +1$ charge state, C_B is nonmagnetic. For C_N, a single hole is introduced in the neutral charge state. This hole occupies a bonding orbital with mostly C $2p_z$ character and some mixing with the surrounding B $2p_z$ states. The neutral charge state is magnetic with $S = 1/2$; the defect acts as a single acceptor,

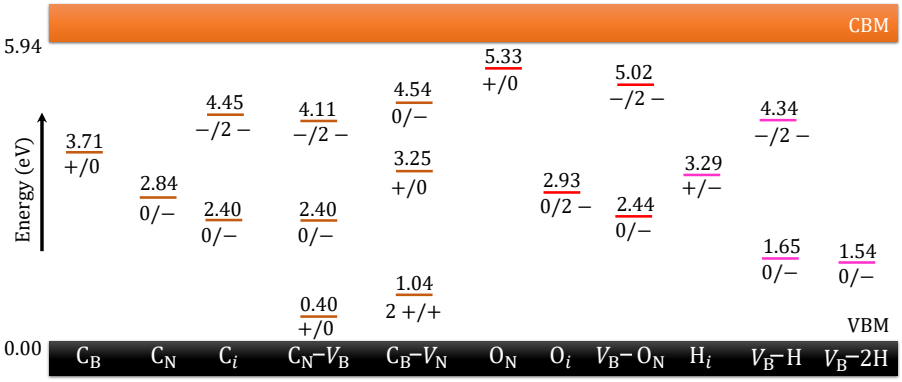

Figure 3.10. Charge-state transition levels for impurity-related defect species in hBN. Defect levels related to carbon are shown in orange, due to oxygen in red, and hydrogen in pink.

and the negative charge state is nonmagnetic. We have also investigated an interstitial C atom (C_i). The C atom sits at an intercalated site. C_i acts as an acceptor, with a $(0/-)$ level 2.40 eV above the VBM, and a $(-/2-)$ level 4.45 eV above the VBM (Fig. 3.10). The formation energy of C_i is very high (Fig. 3.9 (a, b)), and this defect is unlikely to be present in thermodynamic equilibrium; however, the migration properties of C_i are important for understanding how C impurities are incorporated unintentionally during growth, or in doping. The migration barriers are presented in Table 3.3. The migration barrier is low for all charge states, suggesting that C_i moves freely at the intercalated site (consistent with the findings for B_i). Given the high formation energy and low migration barrier of C_i, this defect would either diffuse out of the sample, or migrate until it is annihilated by a vacancy to form C_N or C_B, or until it forms a complex with some other charged defect.

Theoretical studies have proposed a variety of different centers as potential candidates for the SPEs. Recently, Mendelson *et al.* proposed carbon-vacancy related complexes $V_N - C_B$ [134]. Indeed, electronic structure has many defect levels placed within the bandgap, i.e., possibility for internal optical transitions. However, as we see, proposed centers have extremely high formation energies, see Fig. 3.11, making their observation in as-grown material highly unlikely[57].

Oxygen impurities. For oxygen impurities, we consider substitution at an N site only (O_N); oxygen on the boron site (O_B) has an extremely large formation energy. The formation energies indicate that O_N can easily incorporate, particularly under N-poor conditions, and this defect could be present

[57]However, formation of SPEs under chemical etching, electron beam irradiation or ion implantation might be impurity-vacancy related.

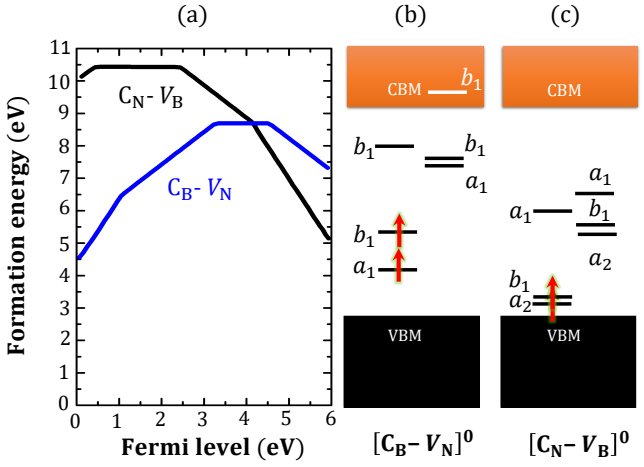

Figure 3.11. (a) Formation energy of carbon-vacancy complexes ($C_N - V_B$ and $C_B - V_N$) in hBN, (b) Schematic diagram of Kohn-Sham states. The orbitals labeled according to the irreducible representations of the C_{2v} point group.

in large concentrations, see Fig. 3.9. O_N is a deep donor, with an (+/0) level 5.33 eV above the VBM, Fig. 3.10. For O_N, localized B−O defect states form; in the neutral charge state, an excess electron is introduced, which occupies an antibonding-like gap state with O and B $2p_z$ orbital character. Since the gap state is singly occupied, O_N^0 is paramagnetic with $S = 1/2$. The $q = +1$ charge state is nonmagnetic. Since O_N acts as a donor, it will shift the Fermi level towards the CBM, and lower the formation energy of native defects with acceptor character. Also, complex formation between the donor and acceptor may occur. Additionally, donor impurities such as O and H can bind to the dangling bonds of boron vacancy and form complexes. In particular, we have explored a complex between O_N and V_B (included in Fig. 3.9 (c, d)); this $V_B - O_N$ complex could be considered an analog to the $N_C - V_C$ center in diamond. This defect acts as a deep acceptor. In the neutral charge state, $V_B - O_N$ has two unoccupied gap states in the minority spin channel, and prefers a HS state with $S = 1$; the defect can accept up to two electrons. Oxygen impurities can also incorporate as an interstitial (O_i), between the hBN layers. O_i acts as a double acceptor, with a (0/2−) level 2.93 eV above the VBM (Fig. 3.10). The $q = +1$ charge state is never stable, i.e., O_i behaves as a *negative U* center. The formation energy is lowest under N-rich conditions. The difference between N-rich and N-poor conditions arises because, for Fig. 3.9 (c, d), we assume the oxygen chemical potential μ_O to be set at the solubility limit, which is determined by equilibrium with B_2O_3. When oxygen is incorporated unintentionally, μ_O is probably well below this extreme limit, leading to considerable formation

energies and relatively low concentrations of O_i in hBN. Still, the migration barriers for O_i are important to understand the kinetics of O incorporation; the barriers are listed in Table 3.3. The O_i defect is highly mobile, even at room temperature, and would be very easily incorporated if its formation energy were low enough. Given its high mobility, O_i would then likely form complexes, and we do not expect it to be present as an isolated defect. Indeed, it was observed that nitrogen vacancies are decorated by oxygen atoms in hBN [194].

Table 3.3. Migration barriers (E_{mb}) for interstitial impurities in hBN. The charge state q is indicated, and the annealing temperature T_{an} is presented, as calculated using equation 3.9 assuming a hopping rate of 1 s^{-1}.

Defect	q	E_{mb} (eV)	T_{an} (K)
C_i	0	1.01	360
	1−	0.86	310
	2−	0.92	330
O_i	0	0.53	190
	2−	0.35	130
H_i	1+	0.75	270
	1−	0.46	170

Hydrogen impurities. Interstitial hydrogen (H_i) is a common impurity in many semiconductors, and is typically amphoteric [195]; i.e, H_i will behave as a donor under p-type conditions, and as an acceptor under n-type conditions. We find the same behavior in hBN (Fig. 3.9 (e, f)). H_i sits at an intercalated site, and has a $(+/-)$ level 3.29 eV above the VBM (Fig. 3.10), consistent with the value found in Ref. [196]. The formation energy of H_i is low, particularly near the band edges, which suggests H_i can be incorporated easily and may behave as a charge-compensating center. The migration properties of H_i are presented in Table 3.3. This defect has a low migration barrier, with $E_{\mathrm{mb}} = 0.75$ eV for H_i^{1+}, and $E_{\mathrm{mb}} = 0.46$ eV for H_i^{1-}. This suggests that H_i is highly mobile, even at room temperature. We thus expect that H_i will form complexes with charged defects and impurities in hBN. Hydrogen atoms interact strongly with vacancy defects in III–nitrides [197]. We have therefore investigated complexes of V_{B} with one, two, or three hydrogen impurities ($V_{\mathrm{B}} - \mathrm{H}$; $V_{\mathrm{B}} - 2\mathrm{H}$; $V_{\mathrm{B}} - 3\mathrm{H}$). The formation energy of the $V_{\mathrm{B}} - \mathrm{H}$ complexes[58] can be low, and is lowest under N-rich conditions, which favor the formation of boron vacancies (see Fig. 3.9 (e, f)). The singly decorated $V_{\mathrm{B}} - \mathrm{H}$ complex behaves similar to V_{B}, with one of the N sp^2 dangling bonds passivated by hydrogen. $V_{\mathrm{B}} - \mathrm{H}$ thus acts as a double acceptor. The neutral charge state is HS with $S = 1$; the $q = -1$ and $q = -2$ charge states have $S = 1/2$ and $S = 0$, respectively. The acceptor levels are deep; the $(0/-)$ and $(-/2-)$ levels are shown in Fig. 3.10. In $V_{\mathrm{B}} - 2\mathrm{H}$, two of

[58] Hydrogen can also form complexes with V_{N}; these are all found to have very high formation energies, and they are not discussed in this Thesis.

the sp^2 dangling bonds on N atoms are passivated, and this defect acts as a single acceptor, with $S = 1/2$ in the neutral charge state. The $q = -1$ charge state is nonmagnetic. The fully passivated $V_B - 3H$ has a low formation energy of 0.95 eV under N-rich conditions, suggesting that it can be present in large concentrations. It is stable only in the neutral charge state, and therefore this defect is electrically inactive.

3.3.6. Discussion and comparison with experiments

Ultraviolet emission in hBN. Several proposals have been put forth to explain the origin of this 4.1 eV line. Some of them centered around the C_N acceptor; carbon is indeed likely to be present as an unintentional impurity in hBN. Based on temperature-dependent PL experiments, Du *et al.* proposed that the 4.1 eV line originates from a donor-acceptor pair (DAP) recombination involving a shallow V_N donor and a deep C_N acceptor [154]. Katzir *et al.* proposed that the 4.1 eV emission originates from the recombination of a conduction-band electron with a neutral C_N defect [151]. Concerning the DAP recombination model, our results (Fig. 3.6) clearly show that the donor level for V_N is deep in the gap, ruling out this model; moreover, to the best of our knowledge, no shallow donors have been identified in hBN. Shallow-donor to deep-acceptor transitions are thus highly unlikely in hBN. Regarding the nature of the deep acceptor, our calculations show that the recombination of electrons in the conduction band with the $(0/-)$ level of C_N gives rise to a ZPL at 3.1 eV. This is so far away from the observed 4.1 eV line that we can confidently rule out C_N as the source of the 4.1 eV emission. Questions surrounding the origins of a frequently observed luminescence signal around 5.3 eV [198–200] can be answered. Based on the calculated charge-state transition level of the O_N impurity, we suggest this luminescence is related to unintentionally incorporated oxygen, see Appendix.

Visible SPEs emission in hBN. Measurements on irradiated or annealed hBN samples have also frequently shown narrow emission lines with energies that range from 1.6 eV to 2.2 eV [26, 28, 201]; here, we broadly refer to these lines as the *2 eV luminescence*. Emissions in this range of energies exhibit clear ZPLs and evidence of a single-photon emission [28]. Examination of the calculated thermodynamic transition levels in Fig. 3.10, allowed to identify plausible defects that may give rise to a free-to-bound transition in the energy range of 1.6 eV to 2 eV. Among vacancies, the hydrogenated boron vacancies are most likely to form. The $V_B - H$ complex has a $(0/-)$ level at 1.65 eV above the VBM, and hence recombination with holes in the VBM would lead to a ZPL at that energy; the complex also has a $(-/2-)$ level at 4.34 eV above the VBM, for which recombination with electrons in the CBM would lead to a ZPL at 1.6 eV. It has also been suggested that the 2 eV emission is associated

with an internal optical transition involving an excited state of the defect [23]. Bright emission requires that the internal transition occurs between gap states in the same spin channel. We find that V_B and its complexes with hydrogen or oxygen form a high-spin state with two or more gap states in the same spin channel. Boron vacancy complexes will be investigated further in the next chapter of this Thesis. We also find that interstitials that are incorporated at an intercalated site (and couple weakly to the lattice) have multiple gap states in the same spin channel, which is essential for an internal transition. As we have shown, defect complexes comprising multiple point defects, such as $V_N - C_B$ [134], also give rise to multiple gap states in hBN. However, none of the remaining isolated point defects that we have investigated, either native defects or impurities, exhibit multiple gap states in their electronic structure or are stable at room temperature and have low formation energy; this precludes them from being a source of the 2 eV emission.

3.4. Summary and Conclusions

A recent study by McDougall *et al.* combined experiment and theoretical calculations to investigate the impact of point defects on the x-ray absorption near-edge structure (XANES) of hBN [202]. The authors measured experimental XANES spectra for several different samples, including sputtered films, single crystals, and powders; by comparing these results with calculated spectra, the authors concluded that O_N, C_B, $V_B - 3H$ were the most dominant defects in these samples. These findings are in excellent agreement with calculated results presented in Fig. 3.9, since we found that these defects have low formation energies and are likely to form. This experimental result is also in agreement with our key finding that impurities play the dominant role in determining defect equilibrium in hBN, rather than native point defects. Additionally, other observations demonstrate that the substitutions arose when holes opened up in the material due to the bombardment by the electron beam, and that they are subsequently filled with C and O atoms available in the overlayers [105].

We have investigated the energetic, electronic, and migration properties of native point defects and common impurities in hBN and discussed them in light of experimental work. Isolated native point defects in hBN have extremely high formation energies, and in the absence of impurities are unlikely to form in observable concentrations under thermodynamic equilibrium. Interstitial defects are too mobile to be stable as isolated defects, but could be present in complexes with (intentional or unintentional) dopant impurities. Vacancy defects have much higher migration barriers and could be present in nonequilibrium conditions, for instance, after irradiation. The defect chemistry of hBN is likely dominated by C, O, and H impurities. Complex formation with hydrogen or oxygen significantly lowers the formation energy of boron vacancies.

Based on our calculated results, we discussed mechanisms for the experimentally observed 4.1 eV and 2 eV emission lines. Overall, these results provide essential information towards identifying the microscopic origin of SPE in hBN. Based on the calculated charge-state transition level of the O_N impurity, we proposed that origin of a frequently observed luminescence signal around 5.3 eV luminescence [198–200] is related to unintentionally incorporated oxygen.

STATEMENT 1

Impurities rather than native defects dominate the defect chemistry of hBN. Due to higher formation energies and migration barriers, bare vacancy defects could be present in nonequilibrium conditions only. The common attribution of the 4.1 eV luminescence to C_N defect is ruled out.

The role of *detrimental* interactions

Investigation of various defect complexes in this material
revealed to us the presence of special dark spots,
if their distances from emitters match the right criteria
they will act as a major quenching force.
Hereby emission will be affected
if quenchers interact with the light sources,
this phenomenon was named to honor
German physicist Theodor Förster.
The main message of this chapter is in the last part
after annealing procedure all quenchers "disappear" or move out,
leading to stabilization of a single photon's quantum light.

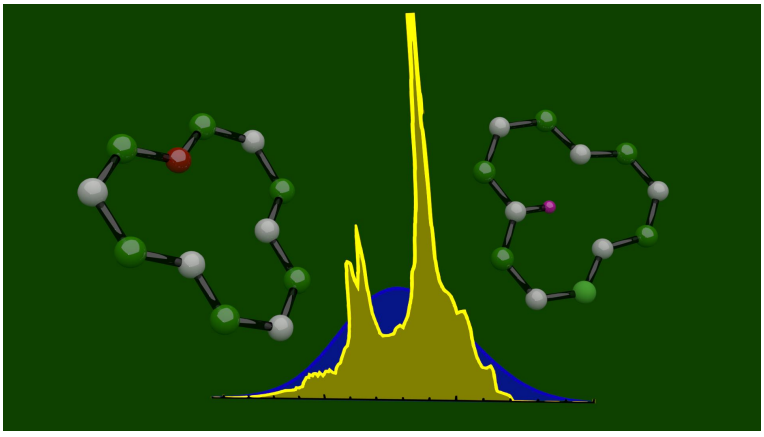

Illustration of SPE emission (yellow) and quencher absorption (blue) spectra overlap in hBN.

Chapter 4

Boron vacancy complexes as luminescence quenchers in hBN

4.1. Introduction

Recently, there was a flurry of experimental studies on single-photon emitters in hexagonal boron nitride, emitting in the red energy spectrum (~ 2 eV). The emitters are usually dim or undetectable in as-grown material, but become very bright upon annealing at temperatures higher than 800 °C. In the previous chapter, the author has demonstrated that impurities likely dominate defect chemistry of hBN. Therefore, in chapter 4, by using first-principles calculations and numerical modeling, the author investigates the electronic, structural, and optical properties of boron-vacancy related complexes. The author unrolls the main results and explains how they might relate to previous experimental observations. The information and results provided in this chapter are based on Paper II.

4.1.1. Literature review of luminescence quenching in hBN

As-grown material typically does not show single-photon emission, or the emission is rather weak [23, 28]. In earlier chapter 2, see section 2.2.3, the author has already discussed a variety of methods used to activate single-photon sources. Nevertheless, certain patterns in the formation of SPEs in hBN are noteworthy. Let us briefly summarize once again that SPEs in hBN are typically observed after a short (up to an hour) annealing in the Ar atmosphere at about 850 °C and (optionally) a subsequent plasma clean in O_2 atmosphere [23]. Lately, this procedure of activation of SPEs has been reproducibly repeated by

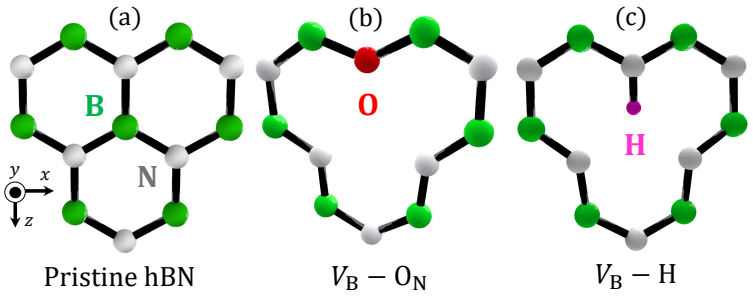

Figure 4.1. (a) Fragment of pristine hBN; (b) V_B–O_N; (c) V_B–H. Atom colors: B (green), N (white), H (purple), O (red).

many groups [25, 26], see paper III. Some variations of the technique have also been proposed with similar success. E.g., in Ref. [30] the annealing is done at 500 °C in the N_2 atmosphere. In Ref. [28], the final annealing is preceded by electron bombardment, but in the majority of cases, no pre-treatment before annealing is needed to activate the emitters. The photostability of SPEs depends on the annealing atmosphere, in Ref. [133] it was shown that annealing in the air activated SPEs that suffer from blinking and eventual photobleaching.

Boron vacancies are defects that are most frequently observed in transmission electron microscopy (TEM) experiments [184, 187] and are therefore believed to be ubiquitous in hBN. However, in previous chapter, the author has shown that under thermodynamic equilibrium, the formation energies of boron vacancy complexes with oxygen or hydrogen (shown in Fig. 4.1) are significantly lower than formation energies of bare vacancies. This conclusion is particularly important for growth methods in which either O or H species are present, such as chemical vapor deposition or synthesis in solution[59]. This calls into question the role of boron vacancy complexes in the observed single-photon emission in hBN and the activation of this emission upon annealing.

4.2. Methodology

4.2.1. One-dimensional configuration coordinate diagram

In this work, the author has studied intra-defect radiative and non-radiative transitions. These processes can be conveniently analyzed using one-dimensional configuration coordinate (CC) diagrams [45, 203], as shown in Fig. 4.2.

[59] In the molecular epitaxy method, both boron and nitrogen carriers are molecules that possess hydrogen atoms.

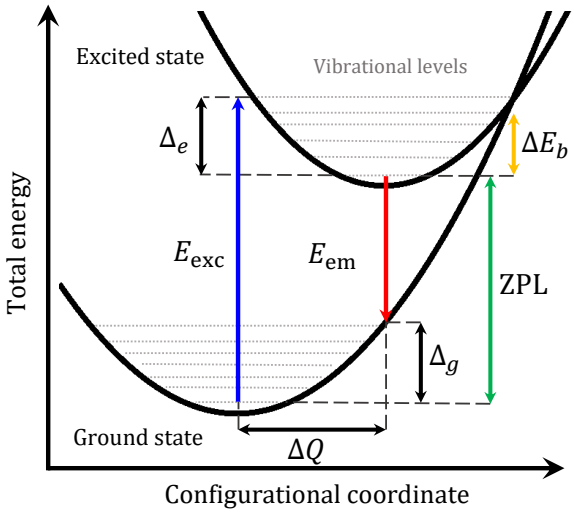

Figure 4.2. Configuration coordinate diagram showing intra-defect optical transition of a defect. The total energy is plotted along the linearly interpolated ground-state geometry of the defect in the ground and excited states. Vibrational levels are shown as horizontal lines within the two potential wells.

The geometry of the excited state will be different from the geometry of the ground state, and this change is represented by a horizontal offset of the two parabolas in Fig. 4.2, i.e., the change of configuration coordinate ΔQ represents a change in the total geometry of the defect during the excitation process. The energy difference between the two parabolas at the equilibrium geometry of the ground state is the excitation energy E_{exc}, and the energy difference between the two parabolas at the equilibrium geometry of the excited state gives the value of emission energy E_{em}. The so-called Franck-Condon shifts Δ_g and Δ_e represent relaxation energies in the ground and the excited state, respectively. The energy difference between energies at equilibrium configurations in the excited and the ground states is called the zero-phonon line (ZPL)[60]. While the configuration coordinate is not strictly a vibrational eigenmode, it is possible to define an effective (or average) phonon frequencies $\omega_{\{e,g\}}$ that describe the change in the geometry [45]. This helps to define the Huang-Rhys factors [204]

$$S_g = \frac{\Delta_g}{\hbar\omega_g} \tag{4.1}$$

and similarly for the excited state. Huang-Rhys factors are important parameters that describe the optical luminescence and absorption lineshapes. Lastly, ΔE_b is the energy difference between the intersection of the two parabolas and the equilibrium energy in the excited state. In the classical interpretation, ΔE_b

[60]ZPL is a transition between two electronic states that does not involve phonons.

is the barrier for the non-radiative transition from the excited to the ground state, and it is useful in interpreting *ab-initio* data. Intra-defect excited states are treated via the Delta Self-Consistent Field approach, whereby electronic excitation is achieved by promoting an electron to a higher-lying Kohn-Sham orbital [50, 205]. This approach is discussed in more detail when considering specific excitation in section 4.2.2.

4.2.2. The Delta Self-Consistent Field DFT calculations

The Delta Self-Consistent Field (ΔSCF) approximation is a density functional method closely resembling standard DFT. Excited states are calculated using the constrained DFT (CDFT) approach, where higher-energy solutions can be obtained in practice by converging the KS orbitals self-consistently with the so-called *non-Aufbau* orbital occupation patterns, amounting to a constraint on orbital occupations [205–207]. Therefore, in ΔSCF occupation of a selected occupied orbital is set to zero, and simultaneously the occupation of a virtual orbital is set to one; see Fig. 4.3 (a). In this approximation, the change of the occupancies in the KS orbitals of the defect states mimics excitation process [86, 208]. The ΔSCF-DFT calculations may provide reliable results if excited states are described by a single Slater-determinant of the KS particles[61] [209].

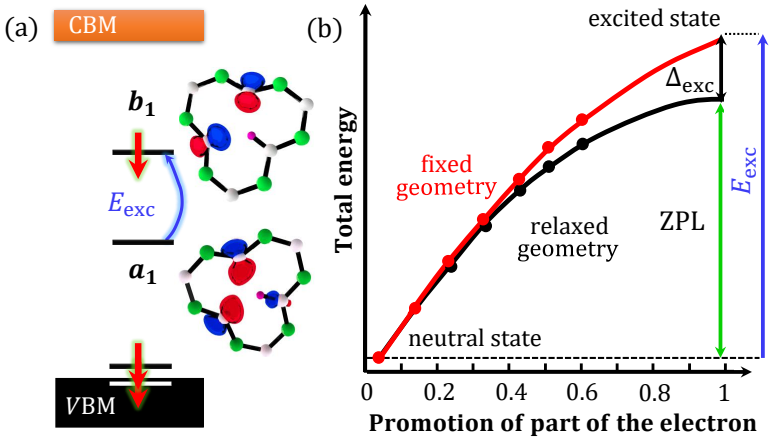

Figure 4.3. (a) In this example, internal optical transition $a_1 \rightarrow b_1$ in charged boron vacancy-hydrogen complex is calculated, (b) ΔSCF calculation of optical excitation is performed by introducing the *fractional orbital occupation* i.e., by promoting part of the electron to a higher orbital.

[61] ΔSCF-DFT is surprisingly accurate for singlet-singlet transitions that are well described by a single-orbital excitation. However, it often fails to provide accurate total energies of highly correlated states that are multi-determinant [86, 208, 209].

We now turn to the calculation of the excited states in boron-vacancy complexes. Fortunately, excited states in neutral ($S = 1$ with multiplet $^3B_1$) and in charged ($S = 1/2$, $^2B_1$) boron vacancy complexes can be described in terms of a single Slater determinant. In Fig. 4.3, as example, the calculation of internal optical transition $a_1 \rightarrow b_1$ in charged boron vacancy-hydrogen complex is represented. The occupation of a a_1 and b_1 orbitals is specified so that an electron is forced to occupy the empty spin channel of the b_1 state, i.e., a_1 state is depopulated, while higher-lying orbital b_1 is populated. Depopulation/population is carried out by introducing the *fractional orbital occupation* [206], it is necessary in the case of V_B–O_N and V_B–H defects. Calculations where one electron was promoted had been found to be computationally very difficult. The reasons for that are the subject of future investigations. Similar behavior has been found for gallium vacancy complex with oxygen in gallium nitride [210]. Therefore *fractional orbital occupation* [206] method helps to approximate the final value of the excitation and ZPL energies[62].

4.3. Results and Discussion

4.3.1. Electronic structure of boron vacancy complexes

The two defects studied in Chapter 4, i.e., the boron vacancy-hydrogen (V_B–H) and the boron vacancy-oxygen (V_B–O_N) complexes, are depicted in Fig. 4.1 and their charge-state transition levels are shown in Fig. 4.4. In previous chapter, the author has shown that both defects can exist in three possible charge states: 0, -1, and -2.

To understand the electronic structure of the defect, let us start with the neutral charge state[63]. Calculations show that there are four localized KS states in the neighborhood of the defect, as shown in Fig. 4.5. In the simplest picture, these defect states can be understood as linear combinations of sp^2 dangling bonds and p_z orbitals pertaining to the two unpassivated N atoms adjacent to the vacancy. The four states can be labeled by the irreducible representation of the C_{2v} point group with their axis of symmetry lying in the plane. The z-axis is the symmetry axis, which points from the vacancy to the oxygen/hydrogen atom (x, y, z axes are shown in Fig. 4.1). Electronic states, b_2 and a_2, that are lower in the bandgap can be mostly thought of as bonding and anti-bonding combinations of the two p_z orbitals. Higher lying states, a_1 and b_1, are formed

[62] Calculation of the excitation energy requires the geometry of the ground state to be kept fixed during excitation of a higher state. Full geometry relaxation of the excited state in this ΔSCF-DFT method gives values of ZPL energy and Franck-Condon shift in the excited state, whereas emission energy and Franck-Condon shift in the ground state values can be obtained by depopulating the excited state while keeping the geometry of the excited state fixed.

[63] The electronic structure of both defect complexes, V_B–O_N and V_B–H, is very similar.

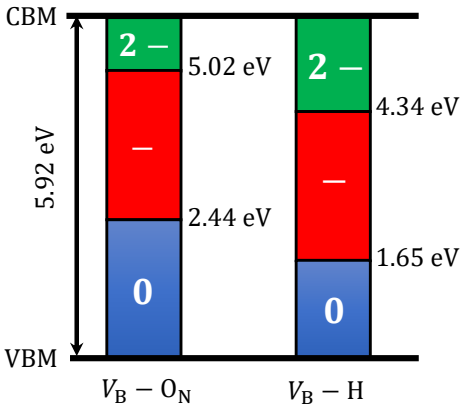

Figure 4.4. Charge-state transition levels of V_B–H and V_B–O_N.

from symmetric and anti-symmetric combinations of the sp^2 dangling bonds. In the neutral configuration, these states are filled by six electrons.

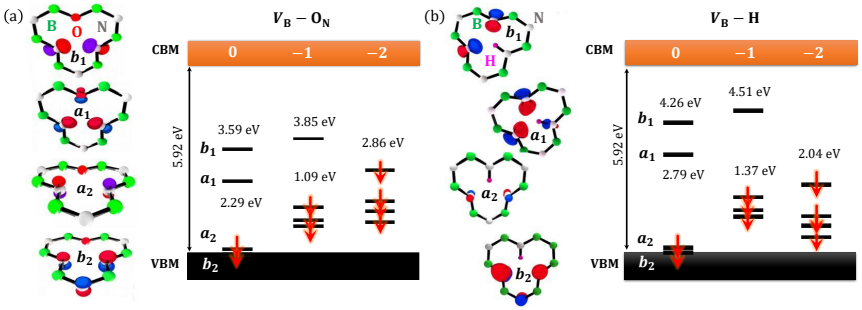

Figure 4.5. Wave functions of the defect states and energies of Kohn-Sham states in the minority spin channel of V_B–O_N (a) and V_B–H (b) complexes in different charge states ($q = 0, -1, -2$). The orbitals labeled according to the irreducible representations of the C_{2v} point group. Atom colors: B (green), N (white), H (purple), O (red).

In previous chapter, the author has shown that the triplet spin state ($S = 1$) is lower in energy than the singlet ($S = 0$), and is, therefore, the ground state. This means that all four defect states are filled in the majority spin channel, while only two of the four states, specifically b_2 and a_2, are filled in the minority spin channel. Therefore neutral complex acts as a double acceptor. The calculated KS energy levels for the minority spin channel in different charge states are shown in Fig. 4.5. In the $q = -1$ charge state, an additional electron occupies the a_1 level, and in the $q = -2$ charge state – the b_1 level is also occupied. The symmetry of the total electronic wave function

can be determined from the symmetry of filled KS states. These symmetries in three charge states for V_B–O_N and V_B–H are identical. The ground state wave functions in different charge states are given in Table 4.1.

Table 4.1. Properties of ground state wave functions pertaining to three charge states of V_B–O_N and V_B–H defects.

Charge	Spin	Electronic configuration	Ground state
0	1	$b_2^2 a_2^2 a_1^1 b_1^1$	$^3B_1$
−1	1/2	$b_2^2 a_2^2 a_1^2 b_1^1$	$^2B_1$
−2	0	$b_2^2 a_2^2 a_1^2 b_1^2$	$^1A_1$

4.3.2. Geometry of boron vacancy complexes

The symmetries of a_1 and b_1 orbitals can help rationalize geometry changes shown in Fig. 4.6. Indeed, since the a_1 state is bonding, i.e., symmetric combination of two sp^2 dangling bonds, its occupation leads to a shortening of the N–N distance (in charge state $q = -1$). In contrast, the b_1 state is anti-bonding, i.e., anti-symmetric combination, and thus its occupation results in an increase of that distance (in charge state $q = -2$).

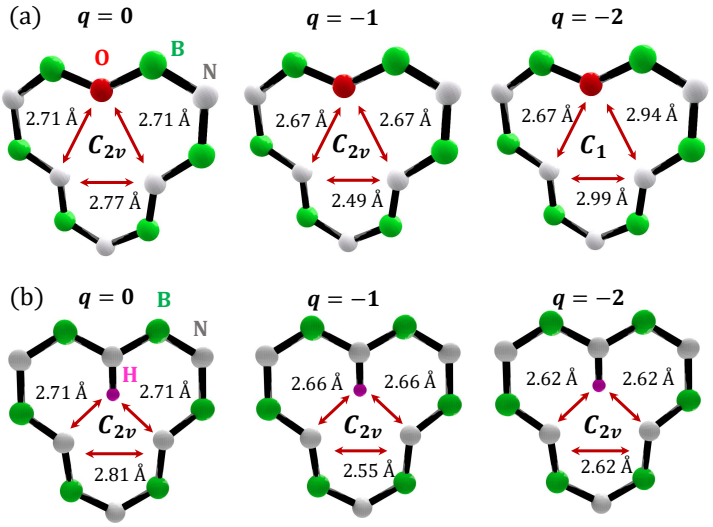

Figure 4.6. Local geometries of the (a) V_B–O_N and (b) V_B–H complexes in three charge states $q = 0, -1, -2$.

Geometries of the V_B–O_N defect in three charge states are shown in Fig. 4.6 (a). For $q = 0$ and $q = -1$, the point group is C_{2v}, and all atoms in the nearest vicinity of the defect remain in-plane. The situation is different for the $q = -2$

charge state, in which the symmetry is lowered to C_1. This happens because of large out-of-plane distortions, shown in Fig. 4.7. One of the N atoms that are adjacent to the vacancy moves vertically and forms a bond with the B atom (bond length 1.60 Å, cf. interlayer distance 3.3 Å).

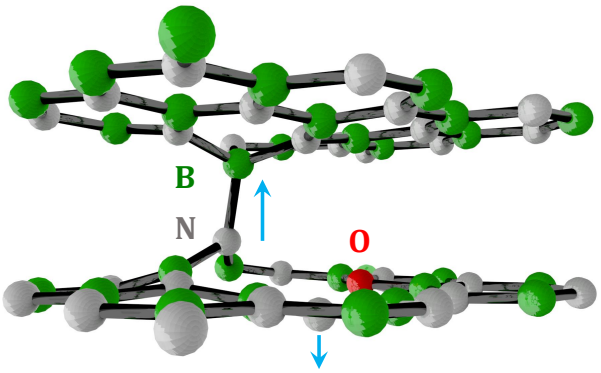

Figure 4.7. Vertical distortion of the V_B–O_N defect in $q = -2$ charge state. The point group symmetry is C_1.

Geometries of the V_B–H defect in all three charge states (0, −1, and −2) are shown in Fig. 4.6 (b). In all three cases, the defect maintains the C_{2v} point group, and we find that there are no out-of-plane distortions. However, there are noticeable changes in the defect geometry for different charge states. The distance between the N atom that is directly bonded to the H atom and the other two N atoms that are adjacent to the vacancy decreases monotonically as the charge state changes from 0 to −2. At variance, the distance between the two N atoms that are next to the vacancy varies in a non-monotonic fashion (2.81 Å for $q = 0$, 2.55 Å for $q = -1$, and 2.62 Å for $q = -2$).

Given the similarity of the electronic structure of the two defects, it might look somewhat surprising that they exhibit a different behavior in the $q = -2$ charge state. The reason behind different geometry changes can be rationalized by taking a closer look at the local electrostatics of the defects. A schematic illustration is shown in Fig. 4.8. While the two sp^2 dangling bonds that are electrically active are nearly identical in both cases, they find themselves in a different environment.

In the ionic picture, the O atom can be thought of as an ion with charge −2 (Fig. 4.8 (a)). The total charge on the N–H pair is similarly −2, which is, however, split between N, which carries −3, and H, which carries +1 (Fig. 4.8 (b)). Our previous calculations of a bare boron vacancy, in chapter 3, showed that completely filled negatively charged N dangling bonds repel each other, leading to sizeable out-of-plane distortions. This is precisely what we find for the V_B–O_N defect. Extra attraction between the positively charged hydrogen

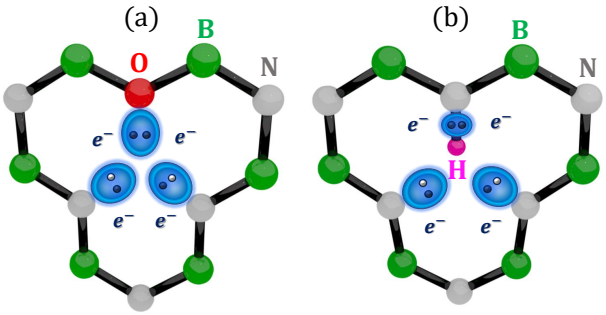

Figure 4.8. Ionic picture of neutral (a) V_B–O_N and (b) V_B–H. Atom colors: B (green), N (white), O (red), H (purple).

and those dangling bonds in the case of the V_B–H defect seems to stabilize the planar configuration for this defect.

Similar reasoning can help explain why the charge-state-transition levels of the V_B–H defect are by nearly 1 eV lower in the bandgap than the corresponding charge-state transition levels of the V_B–O_N defect (Fig. 4.4). When electrons are added to the neutral V_B–H to create $q = -1$ and $q = -2$ charge states, the aforementioned attraction between the added electrons and the H atom helps to stabilize the negative charge state, resulting in their lower energies. This, in its turn, leads to a lowering of $(0/-)$ and $(-/2-)$ charge-state transition levels.

4.3.3. Excited states of V_B–O_N and V_B–H

Boron vacancy complexes, with O or H atoms, have far lower formation energies than native point defects and thus are expected to form in large concentrations in hBN. Furthermore, V_B–O_N and V_B–H defects possess a rich electronic structure and can exist with multiple gap states in the same spin channel (as shown in Fig. 4.5); ergo, the role of excited states should be investigated.

From symmetry considerations, we can build up an energy level diagram of excited states for any of the internal transitions. A single Slater determinant can describe the promotion of the electron to a higher (a_1 or b_1) energy level. The resulted symmetry of many-electron states is shown in Fig. 4.9. To be able to distinguish between similar total wave functions of low-lying and high-lying excited states, we label the upper manifolds with $^3B_1^*$, $^3B_2^*$, $^3A_2^*$, and lower manifolds with $^3B_2$ and $^3A_2$ (Fig. 4.9 (a)), respectively. The electrical dipole moment component μ_i transforms like $(x, y, z) \rightarrow (B_1, B_2, A_1)$ in C_{2v} point group symmetry.

As we see, boron vacancy complexes can have eight excited states in total; five in triplet manifold and three in doublet manifold. However, while twice-excited state $^3B_1^*$ is unstable, internal transitions $a_2 \rightarrow b_1$ and $b_2 \rightarrow a_1$

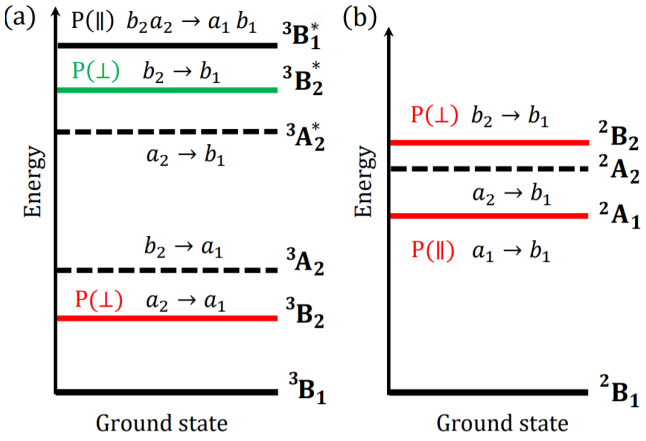

Figure 4.9. Energy level diagram of excited states for (a) neutral and (b) charged boron vacancy complexes. Dipole-allowed transitions from the ground state are represented by green and red lines (color of the line corresponds to the wavelength of excitation). Multiple electron excitations, i.e., twice-excited states, are represented by black lines and forbidden states by black dashed lines. P is polarization: $\parallel$ – in plane, $\perp$ – out of plane.

are dipole forbidden. The only allowed transitions from the ground state in the first order are two excited states ($^3B_2$, $^3B_2^*$) in the neutral charge state and two ($^2A_1$, $^2B_2$) in the negatively charged state. The calculated values of excitation energies, presented in Table 4.2, may be directly compared with the experimental data. Apparently, the lowest excitation energy[64] boron vacancy complexes have in a neutral state, and it is equal to ~ 1.1 eV. In negatively charged complexes, the lowest excitation is equal to 1.77 eV for V_B–H and 2.11 eV for V_B–O_N, respectively. Calculated zero-phonon lines are in the infrared spectral region.

The polarization of the exciting light for intra-defect transitions is charge-state dependent. In the neutral state, it is perpendicular to the symmetry axis, whereas, in the charged state, it has both components ($\parallel$ – in–plane and $\perp$ – out of plane as shown in Fig. 4.9). Due to substantial geometrical changes, i.e., distortions out of plane during the excitation process, boron vacancy complexes have both high relaxation energies and large Huang-Rhys factors[65] (higher than 5.7). The fraction of light emitted into the ZPL will be lower than $3 \cdot 10^{-3}$ for neutral state and lower than $2 \cdot 10^{-4}$ for the negatively charged state, whereas experimentally determined Debye-Waller factor for 2 eV SPEs is around 0.82

[64]The highest excitation to $^3B_2^*$ energy level for both complexes is about ~ 3.3 eV, and it was not investigated further.

[65]Large values of Huang-Rhys factor are typical for systems with strong electron-phonon coupling. This factor significantly influences luminescence lineshape. As Huang-Rhys factor increases, the intensity in the zero-phonon line decreases.

Table 4.2. Allowed internal transition energies of V_B–O_N and V_B–H as calculated by HSE ΔSCF method. Total wave function symmetry in the excited state is Ψ^*.

Complex	Ψ^*	E_{exc}, eV	ZPL, eV	S	ΔE_b, eV
$[V_B–O_N]^0$	$^3B_2$	1.16	0.83	5.7	0.11
$[V_B–H]^0$	$^3B_2$	1.08	0.80	5.9	0.05
$[V_B–O_N]^-$	$^2A_1$	2.11	1.34	36.2	0.09
$[V_B–H]^-$	$^2A_1$	1.77	1.20	8.8	0.42

[23]. ΔE_b values are at range from 0.05 eV up to 0.42 eV, see Table 4.2. Due to low barriers internal transitions are expected to be non-radiative, see Appendix.

4.3.4. V_B–O_N and V_B–H as luminescence quenchers in the 2 eV region

Absorption values of boron vacancy complexes, given in Table 4.2, are precisely in the range of observed 2 eV SPEs emission. Thus, if boron vacancy complexes are close to 2 eV SPEs, SPEs energy will be efficiently transferred to the defect, which acts as a luminescence quencher, and as a result, the intensity of the SPE will decrease. This non-radiative redistribution of an electronic excitation between two defects in solid coupled by the dipole-dipole interaction is known as Förster resonant energy transfer (FRET).

In general, FRET in hBN can occur due to the spectral overlap between the emission of the SPE at 2 eV [23] and the absorption spectrum of the boron vacancy complex with oxygen. The author notes that indeed there is a spectral overlap between normalized absorption cross-section of internal transition $a_1 \rightarrow b_1$ in $[V_B–O_N]^-$ with SPE emission, shown in Fig. 4.10.

From a quantum electrodynamics treatment [203], the absorption cross-section $\sigma(E)$ is given by

$$\sigma(E) = \frac{c^2\hbar^3\Gamma}{8\pi n_D^2 E^2} L(E). \tag{4.2}$$

Here $L(E)$ is the absorption line shape function [203, 211], n_D is the refractive index of the host ($n_D = 2.2$ for the $E_{exc} = 1.08 - 2.11$ eV [212]), and Γ is the rate of the transition.

Computed transition dipole moment for the internal transition $a_1 \rightarrow b_1$ in $[V_B–O_N]^-$ complex is $\mu = 1.15$ eÅ. Calculated absorption cross-section for $[V_B–O_N]^-$ complex in hBN (see Fig. 4.11) is $\sigma(E) = 0.2\text{Å}^2$, while for $[V_B - H]^-$ $\sigma(E) = 0.25\text{Å}^2$ and $\mu = 1.11$ eÅ. This result is consistent with one of the most recent experimental estimates for the absorption cross-section of NV^- centers, i.e., $\sigma(E) = 0.31 \pm 0.08$ Å^2 [213].

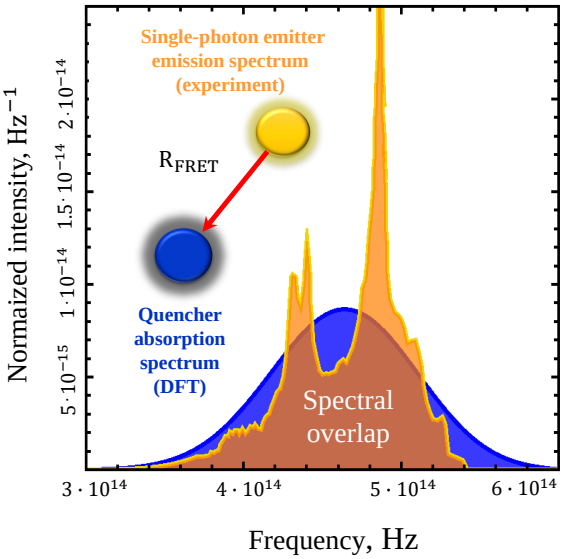

Figure 4.10. Overlap between absorption of the $[V_B–O_N]^-$ complex (DFT, calculated in this Thesis, blue) with emission of the SPE (experimental data adopted from [23], yellow).

The critical distance between two defects in solid at which the energy transfer is half-maximal is called effective Förster radius R_{FRET}. The efficiency of energy transfer is related to the sixth power of the ratio of the distance R, between SPE and quencher, and the R_{FRET}. Effective Förster radius is

$$R_{\mathrm{FRET}}^6 = \frac{3c^4}{64\pi^5 n_D^4} \int_0^\infty \frac{\mathrm{SPE}(\upsilon)\sigma_{\mathrm{abs}}(\upsilon)}{\upsilon^4} d\upsilon. \tag{4.3}$$

Here $\mathrm{SPE}(\upsilon)$ is emission spectra of the SPE and $\sigma_{\mathrm{abs}}(\upsilon)$ is the absorption spectra of the quencher.

Evaluated Förster radius for energy transfer between SPE and quencher in hBN is $R_{\mathrm{FRET}} = 4.5$ nm; i.e., it is equal to 20 B–N distances. At distances smaller than 4.5 nm, SPE emission energy will be effectively absorbed by the boron vacancy complex with oxygen and dissipated nonradiatively (Fig. 4.12 in the region, where $k_{\mathrm{FRET}} > k_{\mathrm{rad}}$). This result is consistent with Förster radius of $R_{\mathrm{FRET}} = 3.8$ nm, between NV center in diamond and organic molecule, as was demonstrated by Tisler *et al.* [214]. Furthermore, both SPE emission and quencher's absorption are polarized in the plane. It is important to note that based on ZPL energy and phonon side band spectral shape, SPEs in hBN are classified into two general groups. First group with ZPL at 2.15 eV and second group with ZPL at 1.78 eV [24]; ergo, in the Appendix, the author calculates

the Förster radius between SPE (at 1.77 eV) and $[V_B–H]^-$ complex.

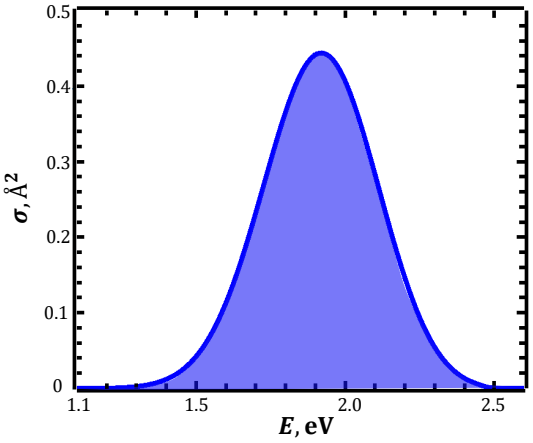

Figure 4.11. Absorption cross-section of the $[V_B–O_N]^-$ complex.

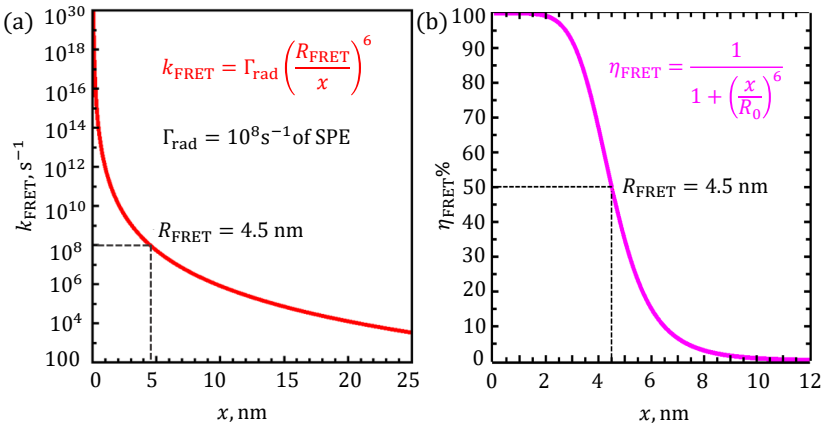

Figure 4.12. (a) Rate of Förster energy transfer in hBN between $[V_B–O_N]^-$ and SPE. At distances $x < 4.5$ nm energy transfer will be faster than the radiative decay rate of SPE Γ_{rad}. (b) R_{FRET} is the characteristic distance at which energy transfer is half-maximal.

Distribution of distances between quenchers and SPE can be approximately estimated with a lower cut-off of $R_0 = (3/4\pi n)^{\frac{1}{3}}$. Therefore, it was evaluated that at concentrations of $2.6 \cdot 10^{18}$ cm^{-3} of quenchers, the distance between selected SPE and a quencher is expected to be approximately equal 4.5 nm. Remarkably, in best quality hBN crystals, carbon and oxygen impurities can be as low as $10^{17} - 10^{18}$ cm^{-3}, which has been experimentally determined by secondary ion mass spectroscopy and CL in Ref. [193]. Furthermore, it is known

that during growth and exfoliation procedure, oxygen can be trapped within the hBN lattice [194]. In an oxygen-rich environment, the concentration of boron vacancy complexes with oxygen can be even higher [24, 133].

It is worth noting that the concentration of SPEs is significantly lower than the concentration of quenchers. In general, 1 emitter per 1 μm^2 is observed. Furthermore, less than 10 emitters per whole exfoliated flake (about 30 µm lateral) were observed by Chejanovsky *et al.* [26]. Taking the typical thickness of the multilayer to be approximately about 100 nm, we end up with SPE densities of 10^{13} cm^{-3}. Accordingly, taking into account the concentration of SPEs and the expected concentration of oxygen-related complexes, FRET from a boron vacancy complex to a single photon emitter in hBN should be an efficient mechanism.

4.3.5. Two nitrogen dangling bonds

Given that SPEs, which are quenched, occur in the vicinity of a dangling bonds (DBs): at the edge of flakes or near grain boundaries [26,128,133], the model of boron vacancy complexes, i.e. two nitrogen dangling bonds, could in principle be extended and uncover the physics of PL quenching and PL instabilities in hBN.

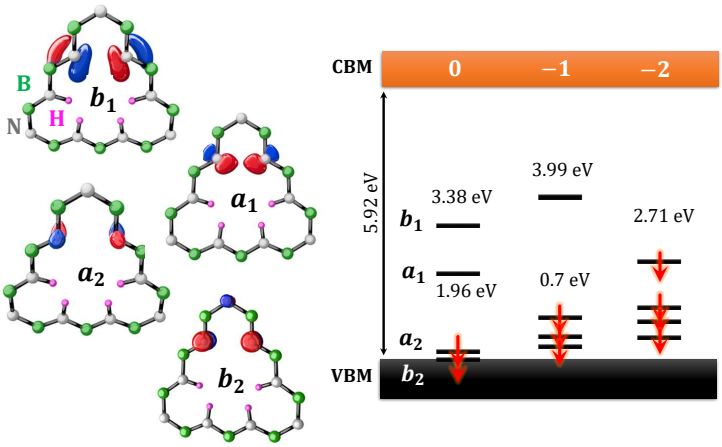

Figure 4.13. Wave functions of the defect states and energies of Kohn-Sham states (minority spin channel) of two isolated nitrogen dangling bonds in different charge states. The orbitals labeled according to the irreducible representations of the C_{2v} point group. Atom colors: B (green), N (white), H (purple).

As we see in Fig. 4.13, two perfectly isolated nitrogen DBs show similar four localized KS states in the neighborhood of the defect, as was shown in Fig. 4.5 for boron vacancy complexes. It should be noted that boron and nitrogen dangling bonds will display the opposite behavior in hBN. While 2 eV

SPE emission is attributed to boron dangling bonds [135], according to our findings, two nitrogen dangling bonds are perfect luminescence quenchers of 2 eV emission. Interaction between boron and nitrogen DBs will depend on local distortions. Finally, both of them (boron and nitrogen DBs) can easily be formed at the edge of the crystal or near grain boundary. Once again, it turns out that 2 nitrogen DBs are independent of their surrounding environment. This implies, that perfectly isolated, 2 nitrogen DBs with a fully passivated third one, will give rise to non-radiative intra-defect transitions[66].

4.3.6. Comparison with experiments

2 eV SPEs suffer from severe problems such as blinking and bleaching, which result in severe fluctuations of photon emissions and even defect-luminescence quenching [23,26–28,128]. Chejanovsky *et al.* obtained excellent photostability of SPEs even under ambient conditions [26]. Furthermore, annealing proved to be a crucial step for emitter stability in order to avoid working with blinking emitters. In previous chapter 3, the temperatures at which point defects and impurities can be *annealed out* were determined. Annealing temperature for boron vacancies is around $\sim$ 840–1110 K for different charge states, and this result suggests that these defects become mobile during higher growth temperatures for chemical vapor deposition (and other growth techniques), as well as at typical annealing temperatures. The annealing process can also dehydrogenate boron vacancy complexes with H [197], electronically activating the defect. Surprisingly, it appears that the annealing environment determines the stability of the observed emission. Perhaps due to an ionization mechanism or oxygen quenching [26,133], SPEs annealed at 850 °C in vacuum were less stable than those annealed in argon. It is interesting to note that Martinez *et al.* has observed that only around 5% of the emitters in bulk high-purity hBN crystal exhibits a perfect photostability over time [27]. Furthermore, Shotan *et al.* demonstrated that during extended exposure to blue light, the optical response of SPEs could be changed, ultimately producing bleaching of SPEs (see paper III). This result suggests that a drastic modification of the defect environment takes place, possibly through surface photochemistry.

On the other hand, it was recently shown that high-dose ion irradiation contributes to the dark-defect-ensemble generation, i.e., it is related to the defect quenching in hBN. It makes our argument stronger that dangling nitrogen bonds are involved in the quenching mechanism, since kick-out energy for boron atoms is lower than for nitrogen atoms [215]. As a whole, all these results unveil a *complex physics* of SPEs in hBN.

[66] Furthermore, this model in principle could be expanded and applied for charged boron vacancies, where one of the dangling bonds is fully occupied; however, bare boron vacancy due to a higher symmetry (D_{3h}, not C_{2v}) has more optically accessible excited electronic states. Thus, these findings are applied only for 2 nitrogen DBs that display C_{2v} point group symmetry.

4.4. Summary and Conclusions

In Chapter 4, by using first-principles calculations and numerical modeling, the author shows that the thermal activation of emitters is most likely due to boron vacancies and their complexes with hydrogen and oxygen. Due to the large coupling to the lattice, these defects will have non-radiative internal transitions, i.e. boron vacancy complexes are not emitters themselves. Through Förster's resonant energy transfer from red SPEs to boron vacancy complexes, they will act as efficient luminescence quenchers. Two nitrogen DBs are independent of their surrounding environment. At about 800 °C the concentration of these complexes diminishes significantly due to the activated diffusion of boron vacancies, explaining experimental findings. This model was expanded for two perfectly isolated nitrogen DBs, which likewise will give rise to non-radiative intra-defect transitions in hBN. Future experiments are required to confirm these findings.

STATEMENT 2

Quenching of 2 eV single photon emission can be explained through Förster resonant energy transfer from red SPEs to boron vacancy complexes with hydrogen and oxygen. The proposed 2 eV SPE luminescence quenching model can be expanded for two perfectly isolated nitrogen dangling bond systems in hBN.

Ode to carbon in hBN

It is not surprising that we like those,
who are similar to us,
carbon likes carbon, not unlike two lovers
are attracted to each other
the love of this pair is so strong
that in pair they belong for lifelong
this ultraviolet romance
is the main reason and chance
to give a birth for a quantum light
in hexagonal boron nitride.

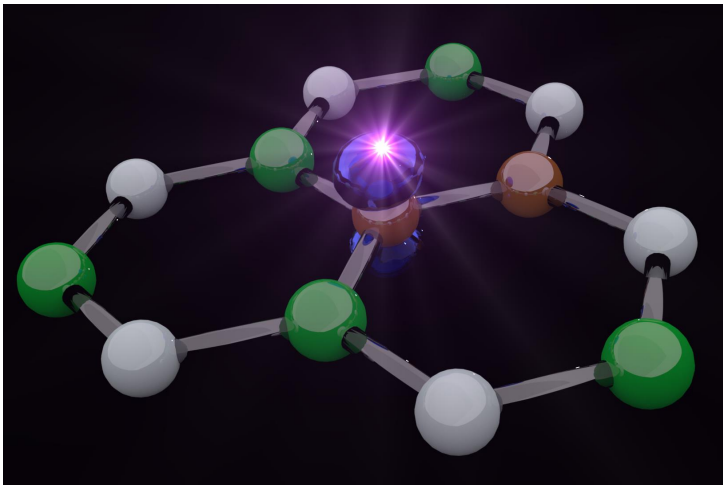

Illustration of single-photon emission in the UV range from carbon dimer defect in hexagonal boron nitride.

Chapter 5

Carbon dimer defect as a source of the 4.1 eV luminescence in hBN

5.1. Introduction

Although carbon was identified as playing an essential role in the observation of well-known point defect emitting in the UV range in hBN, there is no direct experimental proof that carbon is one of the components of this point defect. The literature review in 5.1.1 clearly describes the relevance and timeliness of investigating the origin of the 4.1 eV band (the so-called 4.1 eV defect). In this context, with numerous recent papers on this subject, the author provides *ab-initio* calculations through hybrid density functionals in order to test the recent proposition that carbon aggregates may explain defect luminescence in the UV range [216]. The results provided in this chapter are based on Paper IV.

5.1.1. Literature review of the 4.1 eV luminescence in hBN

In this section, the author gives a brief review that covers the most recent literature on the UV emission in hBN. Photoluminescence, cathodoluminescence, and electroluminescence experiments dating back to the 1950s [217] already revealed a strong emission band between 3.3 and 4.1 eV in bulk hBN. This near-UV emission was so prevalent in some early samples that the bandgap of hBN was sometimes erroneously assumed to be just above 4 eV [218]. However, more careful spectroscopic experiments [154, 198, 219] on better-quality material revealed that the 4 eV luminescence is defect-related and is composed of

at least two bands with very distinct properties. One is a broad featureless band centered around 3.9 eV [198]. The other is a much narrower band with a clearly distinguishable ZPL at 4.08 eV (typically called the 4.1 eV band in the literature) and which is accompanied by a few phonon replicas [154, 198, 219]. The dimensionless Huang-Rhys parameter, which quantifies electron-phonon coupling during optical transitions [203], was estimated to fall in the range $S = 1$–2 for this band [220]. The PL of this structured band appears when excitation energies exceed the ZPL of 4.1 eV. At variance, the broad 3.9 eV band appears only at excitation energies larger than 4.5 eV [198]. Furthermore, time-dependent luminescence associated with these bands possesses very distinct characteristics. The structured narrow band shows very fast single-exponential decay with a lifetime $\tau = 1.1$–1.2 ns [198, 219], while the wide band exhibits multi-exponential dynamics with the slowest components having decay times of a few 100 ns [198]. Additionally, a non-single-photon broadband is, although spatially localized, not correlated with the SPE emission. The intensity of this broad 3.9 eV band increases upon electron irradiation, and therefore vacancies and interstitial defects are likely to play a role in it [103]. In summary, all experimental results mentioned above, indicate a very distinct origin of the two bands, and from now on in this work will be discussed only the structured 4.1 eV band.

Recently, single-photon emission associated with the 4.1 eV band has been reported [103]. Fast electrons in a transmission electron microscope [221] were used to excite luminescence at $T = 150$ K. Measurement of the second-order correlation function confirmed that photons originate at a single emitter. The lineshape and the lifetime [221] of the CL band were identical to those in ensemble measurements, confirming that in both experiments, luminescence was caused by the same defect. These experiments have renewed the interest in the 4.1 eV band due to its potential use in quantum optics.

Despite the ubiquity of the 4.1 eV line, the microscopic nature of the defect that causes the luminescence is still not known. The intensity of the band increases drastically in both bulk crystals [219] and epitaxial layers [222] when carbon is purposely introduced during growth. Therefore, the involvement of carbon has been naturally assumed [154, 219]. It has been suggested [151, 154, 222] that the 4.1 eV emission is caused by a transition from either a shallow donor (a so-called donor-acceptor-pair or DAP transition) or the conduction band (free-to-bound transition) to the neutral carbon acceptor on the nitrogen site, C_N. However, there are strong arguments against these models. First, the time dynamics of DAP and free-to-bound transitions are inconsistent with the measured lifetime of $\tau = 1.1$–1.2 ns. For DAP transitions, the variation in donor-acceptor pair distances usually leads to marked non-exponential decay dynamics with very long tails [198], at odds with the single-exponential decay of the 4.1 eV line [198, 219]. Regarding radiative free-to-bound transi-

tions, these occur on a millisecond time scale at typical excitation conditions (carrier densities $\sim 10^{17}$ cm^{-3}) [203], significantly slower than the dynamics of the 4.1 eV line. An additional argument comes from our previous chapter 3, where the acceptor level of C_N was found to be at 2.84 eV above VBM. Since the bandgap of hBN is $\sim$ 6.1 eV, DAP, and free-to-bound transitions should, therefore, have energies smaller than 3.2 eV, i.e., they should not appear in the UV region at all. The fast nanosecond radiative decay dynamics of the 4.1 eV line [198, 219, 221] indicates that this is a transition where the ground state and excited state are localized in close proximity, likely on the same defect. Recently, Korona and Chojecki [216] used quantum chemistry calculations to suggest that carbon clusters made from two to four atoms give luminescence in the range from 3.9 to 4.8 eV in monolayer hBN. However, different UV lines were not discriminated in that study, and neither the stability of clusters nor parameters (lifetime and electron-phonon coupling) of optical transitions were investigated.

5.2. Methodology

5.2.1. Singlet excitations at defects

DFT only works when the states in the non-interacting case reduce to single Slater determinants. In this section, we construct a Hohenberg-Kohn theory for states of not pure, but mixed symmetry. It is a so-called *multiplet problem* that was investigated by Ziegler, von Barth, and Lanno [223–225]. According to this approach, if a single Slater determinant is not a properly symmetric state, it can still be expressed as a linear combination of these states [226]. It is convenient to explain this method with a specific case, e.g., the singlet excitations at neutral carbon dimer (C_BC_N) in hBN, which will be investigated in this chapter. Kohn-Sham states of C_BC_N in ground state, excited singlet and triplet states are presented in Fig. 5.1.

If we follow the reasoning of Ulf von Barth, we can write three components of the triplet state

$$\Psi_{T;+1} = \frac{1}{\sqrt{2}} \begin{vmatrix} \phi_1(1)\alpha(1) & \phi_1(2)\alpha(2) \\ \phi_2(1)\alpha(1) & \phi_2(2)\alpha(2) \end{vmatrix}, \Psi_{T;-1} = \frac{1}{\sqrt{2}} \begin{vmatrix} \phi_1(1)\beta(1) & \phi_1(2)\beta(2) \\ \phi_2(1)\beta(1) & \phi_2(2)\beta(2) \end{vmatrix},$$
$$\Psi_{T;0} = \frac{1}{\sqrt{2}} \left[\phi_1(1)\phi_2(2) - \phi_2(1)\phi_1(2)\right] \frac{1}{\sqrt{2}} \left[\alpha(1)\beta(2) + \beta(1)\alpha(2)\right]. \quad (5.1)$$

Here α and β are used for spin-up and spin-down electron, ϕ_1 and ϕ_2 are the single-particle spatial wave functions for the b_2 and b_2^* states. As we see, the third component is more complicated.

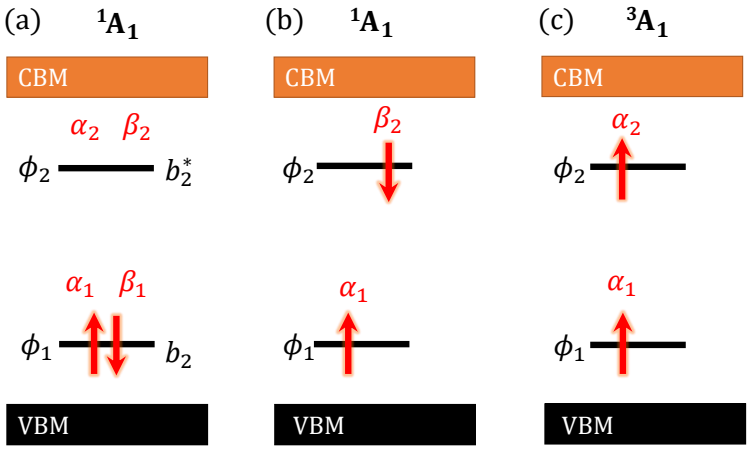

Figure 5.1. Kohn-Sham states of the C_BC_N defect in hBN in (a) ground state, (b) excited singlet, and (c) excited triplet states.

The excited state singlet is expressed as

$$\Psi_S = \frac{1}{\sqrt{2}}\left[\phi_1(1)\phi_2(2) + \phi_2(1)\phi_1(2)\right]\frac{1}{\sqrt{2}}\left[\alpha(1)\beta(2) - \beta(1)\alpha(2)\right]. \tag{5.2}$$

This state is not a pure spin state, but, as we will see, a mixture of a singlet and a triplet, i.e., a multi-determinant state[67]. Application of DFT to singlet excited state $^1A_1$ is not rationalized, because excited singlet state and lower state, i.e., ground-state singlet $^1A_1$, are of the same symmetry [224, 226], see Fig. 5.1 (a) and (b). However, the excitation, which we assumed to be a singlet state, is, in fact, a mixed-spin state

$$\Psi_{S/T} = \frac{1}{\sqrt{2}}\begin{vmatrix}\phi_1(1)\alpha(1) & \phi_1(2)\alpha(2)\\ \phi_2(1)\beta(1) & \phi_2(2)\beta(2)\end{vmatrix} = \frac{1}{\sqrt{2}}\left(\Psi_S + \Psi_{T;0}\right). \tag{5.3}$$

The average energy[68] of this mixed-spin state $E(S/T)$ can be calculated as

$$E(S/T) = \langle\Psi_{S/T}|H|\Psi_{S/T}\rangle = \frac{1}{2}[E(T) + E(S)], \tag{5.4}$$

It can be noted that the energy of the mixed-spin state represents the average between a singlet and a triplet states (i.e., $E(S) \neq E(S/T)$), where the energy of the triplet state is

$$E(T) = \langle\Psi_{T;+1}|H|\Psi_{T;+1}\rangle. \tag{5.5}$$

[67] In a pure singlet state, the spin density should be localized, however, there is a spin-up density at the position of the b_2 orbital, and a spin-down density at the position of the b_2^* orbital.

[68] Calculation of the expectation value of the many-electron Hamiltonian.

Hence final relation for singlet excitation energy is

$$E(S) = 2E(S/T) - E(T). \tag{5.6}$$

Summarizing, the author concludes that the energies of $E(S/T)$ and $E(T)$ are correctly described by the ΔSCF approach using DFT because they are made of single Slater determinants. Fortunately, the singlet state is a linear combination of these two states; therefore, we can estimate the actual excitation energy.

5.3. Results and Discussion

5.3.1. Formation energy of C_BC_N

We start by calculating the formation energy [83] of the carbon dimer $E_f(C_BC_N)$, which is given by

$$\begin{aligned} E_f(C_BC_N) &= E_{tot}(C_BC_N) - E_{tot}(BN) + \mu_B + \mu_N \\ &\quad -2\mu_C + q(E_F + E_V) + \Delta_q, \end{aligned} \tag{5.7}$$

where $E_{tot}(C_BC_N)$ is the total energy of the supercell containing one dimer, and $E_{tot}(BN)$ is the total energy of a pristine supercell. μ_N and μ_B are chemical potentials of nitrogen and boron; $\mu_N + \mu_B = \mu_{BN} = E_{BN}$, where E_{BN} is the total energy of bulk BN per formula unit. μ_C is the chemical potential of carbon, set to the per-atom energy of a diamond crystal. In equation 5.7, q is the charge of the defect, and E_F is the Fermi level, referenced to the VBM E_V. Δ_q is a finite-size electrostatic correction term [167]. The author notes that the formation energy of the dimer does not depend on individual chemical potentials μ_N and μ_B, as $\mu_N + \mu_B = \mu_{BN}$.

The calculated formation energy is shown in Fig. 5.2, together with formation energies of C_B and C_N defects. For these two latter defects formation energies *do* depend on the chemical potentials of boron and nitrogen; only two limiting cases are shown in Fig. 5.2. For N-rich conditions $\mu_N^{rich} = 1/2E_{tot}(N_2)$, half the energy of the N_2 molecule; for B-rich (N-poor) conditions $\mu_B^{rich} = E_{tot}(B)$, the energy of the B atom in elemental boron.

We find that C_BC_N has three possible charge states, $q = -1$, $q = 0$, and $q = +1$, see Fig. 5.2. The neutral charge state is the most stable one throughout most of the band gap, with a formation energy of 2.1 eV. As can be seen in Fig. 5.2, the formation energy of the dimer is not lower than those of simple substitutional defects for the two limiting cases of atomic chemical potentials. However, there is a wide range of chemical potentials ($\mu_N^{rich} - 2.5$ eV $< \mu_N < \mu_N^{rich} - 0.6$ eV) and Fermi levels for which C_BC_N is more stable than either C_B or C_N. In addition, if both C_B and C_N are present in the material (e.g., as

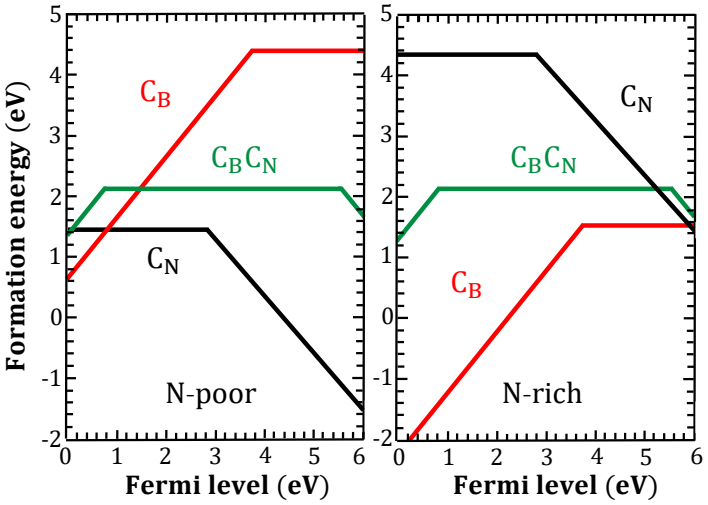

Figure 5.2. Calculated formation energies vs. the Fermi level for C_BC_N, C_B, and C_N defects under (a) N-poor and (b) N-rich conditions.

a result of non-equilibrium growth), the formation of C_BC_N is expected. For example, when C_B^+ binds to C_N^- to form $(C_BC_N)^0$, an energy of 3.1 eV is released, indicating an exothermic reaction. The author concludes that whenever carbon is present during the growth of hBN, C_BC_N should be a common defect.

5.3.2. Electronic structure of C_BC_N

C_BC_N dimer is a complex formed between the donor C_B and the acceptor C_N. The calculated charge state transition levels are near the band edges, see Fig. 5.2. When the donor and acceptor are far away, C_B is positively charged, whereas C_N is charged negatively. When forming the dimer, the oppositely charged donor and acceptor are Coulombically attracted, as a result, formed complex becomes electrically neutral. The molecular orbital diagram of C_BC_N dimer formation in hBN is presented in Fig. 5.3. C_N and C_B molecular orbitals strongly interact and form two states, an antibonding and bonding states, within the band gap of hBN.

We now turn to the electronic properties of the dimer. In the neutral state, which is the one we will consider here, the dimer is non-magnetic ($S = 0$). Singlet is more stable than triplet, and our DFT HSE calculations give the energy difference of 3.20 eV. The Kohn-Sham electronic state diagram, Fig. 5.4 (a), indeed, shows that there are two defect states in the bandgap. The lower-lying state is a p_z orbital localized on the *acceptor* site C_N, while the higher-lying state is a p_z orbital on the *donor* site C_B, Fig. 5.4 (b). The defect geometry belongs to the C_{2v} point group, and both states can be labeled according to

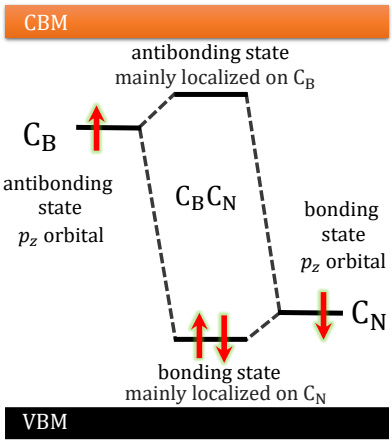

Figure 5.3. Molecular orbital diagram of formation of C_BC_N dimer in hBN, showing the interaction between two p_z orbitals of isolated C_B and C_N defects.

the irreducible representation b_2. To distinguish the two states, we label the upper one b_2^*.

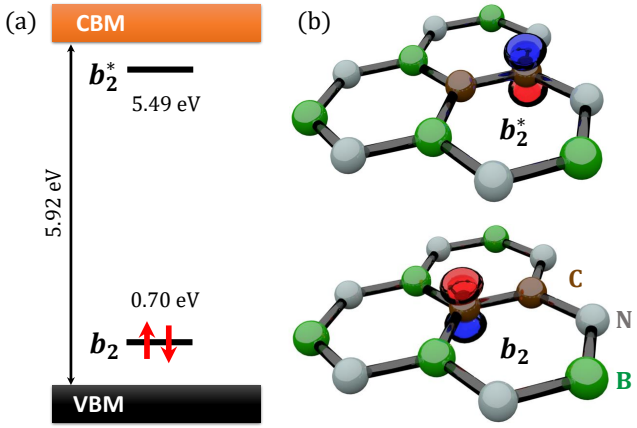

Figure 5.4. (a) Energies of Kohn-Sham states and (b) wave functions of the defect states of the neutral C_BC_N complex in hBN.

In the ground state of the neutral dimer, the b_2 state is doubly occupied, while the b_2^* state is empty, resulting in electronic configuration $|b_2\bar{b}_2\rangle$, symbols without a bar are for spin-up electrons, symbols with a bar for spin-down. This is a singlet state $^1A_1$. Geometry changes of excited C_BC_N dimer are presented in Fig. 5.5. In the ground state, the length of the C−C, C−N, and C−B bonds are 1.361, 1.391, and 1.497 Å, respectively (cf. the nearest-neighbor distance

of 1.435 Å in bulk hBN). The excited state is obtained when one b_2 electron is promoted to the b_2^* state, yielding configuration $|b_2\bar{b}_2^*\rangle$, also a $^1A_1$ state. We calculate the energy and the resulting geometry of the defect in the excited state using the ΔSCF approach [205] with constrained orbital occupations. In the excited state, there is a slight geometry rearrangement: the C−C bond elongates by 6% to 1.453 Å, while C−N and C−B bond lengths change by less than 1.5% (to 1.372 and 1.499 Å, respectively).

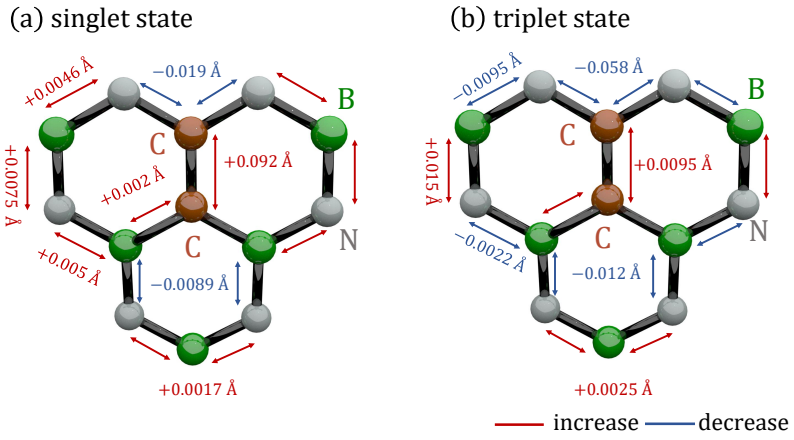

Figure 5.5. Local geometry changes for C_BC_N dimer in hBN in the excited (a) singlet and (b) triplet states.

5.3.3. Configurational coordinate diagram of C_BC_N

The calculated one-dimensional configuration coordinate diagram [203] is shown in Fig. 5.6 (a). We obtain a ZPL energy of $E_{\mathrm{ZPL}} = 4.06$ eV. The Franck-Condon shifts are 0.22 eV in the excited state and 0.24 eV in the ground state. To quantify electron-phonon coupling, we calculate [227] the Huang-Rhys factor S, which is a measure of the average number of phonons emitted during the optical transition [203]. We find an effective phonon frequency of $\hbar\Omega = 130$ meV, yielding the Huang-Rhys factor $S = 0.24/0.133 = 1.9$, which is consistent with the experimental estimate S =1–2 reported in Ref. [220]. The Huang-Rhys factor is related to the Debye-Waller factor w_{ZPL} (the fraction of light emitted into the ZPL) via $w_{\mathrm{ZPL}} \approx e^{-S}$. Our calculated value of $w_{\mathrm{ZPL}} \approx 0.17$ is smaller than the experimental value of 0.26 reported in Ref. [155]. However, note that due to the exponential dependence of w_{ZPL} on S small errors in the latter can lead to large errors in the former.

Apart from the excited-state singlet $^1A_1$, there is also a triplet state $^3A_1$ with configuration $|b_2b_2^*\rangle$. $^3A_1$ is 3.25 eV above the ground state, i.e., 0.81 eV lower than the excited-state singlet due to the exchange interaction between the

two electrons. The energy-level diagram of the neutral C_BC_N dimer is shown in Fig. 5.6 (b).

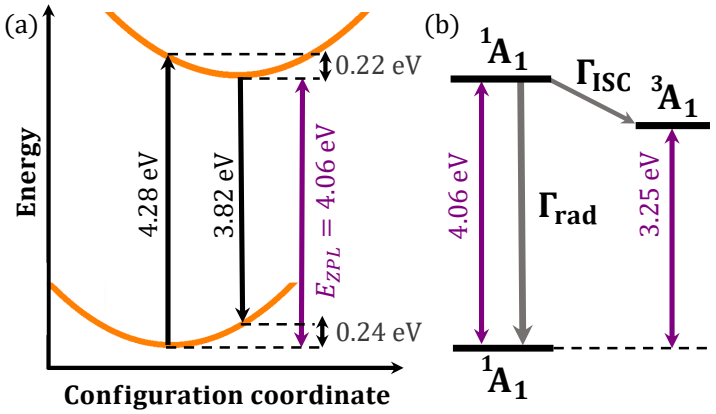

Figure 5.6. (a) Configuration coordinate diagram describing the optical excitation process between two $^1A_1$ states for the neutral C_BC_N dimer in hexagonal boron nitride. (b) Energy-level diagram of the neutral C_BC_N dimer.

The rate of the radiative transition between the two singlet states is given by (in SI units) [203]:

$$\Gamma_{\text{rad}} = \frac{1}{\tau_{\text{rad}}} = \frac{n_D E_{\text{ZPL}}^3 \mu^2}{3\pi\varepsilon_0 c^3 \hbar^4}. \tag{5.8}$$

Here ε_0 is vacuum permittivity, n_D is the refractive index of the host ($n_D \approx 2.6$ for energy $E \approx 4$ eV [212]), and $\mu = 1.1$ eÅ is the computed transition dipole moment for the transition $b_2 \to b_2^*$. Using the calculated value of $E_{\text{ZPL}} = 4.06$ eV, we obtain the rate $\Gamma_{\text{rad}} = 8.3 \times 10^8$ s^{-1}, corresponding to $\tau_{\text{rad}} = 1.2$ ns.

The $b_2 \to b_2^*$ transition is a strong dipole transition (so-called $\pi \to \pi^*$ transition) with the polarization along the C–C bond. However, one should not observe polarization in ensembles due to 6 possible orientations of C–C axes, i.e. polarization will be well defined only for isolated SPEs in hBN. Experimental measurements of polarization would be really valuable but have not yet been performed, to the best of our knowledge.

The calculated $\tau_{\text{rad}} = 1.2$ ns is in good agreement with the experimental value of 1.1–1.2 ns [198, 219], but one should exercise caution comparing the two. The lifetime of the excited state $^1A_1$ is governed by two decay mechanisms, see Fig. 5.6 (b): the radiative transition to the ground state Γ_{rad} and the intersystem crossing (ISC) to the triplet state Γ_{ISC}: $\tau = 1/(\Gamma_{\text{rad}} + \Gamma_{\text{ISC}})$, thus the rate of ISC should be evaluated.

5.3.4. Inter-system crossing

Here we provide the estimate for the inter-system crossing (ISC) rate $\Gamma_{\rm ISC}$ between excited states $^1A_1$ and $^3A_1$ of the C_BC_N defect, Fig. 5.6 (b). The principal mechanisms for inter-system crossing are (i) spin-orbit interaction and (ii) hyperfine interaction [228].

(i) Spin-orbit interaction can be written in the form $V_{\rm so} = \sum_{i=1,2} \vec{\lambda_i} \cdot \vec{\sigma_i}$, where the sum is over the two optically active electrons of the C_BC_N defect, $\vec{\sigma}$ is a vector made of Pauli matrices, and $\vec{\lambda}$ quantifies the spin-orbit interaction (mean-field approximation is assumed). In the C_{2v} point group, the three Cartesian components of $\vec{\lambda}$ transform like B_2, B_1, and A_2 irreducible representations [229], and therefore they do not couple two states with A_1 orbital symmetry. Thus, the author concludes that to first order spin-orbit interactions will cause no ISC between $^1A_1$ and $^3A_1$ states.

(ii) To estimate the contribution of hyperfine interactions, we first note that both defect orbitals are localized on carbon atoms, see Fig. 5.4 (b). Since the majority of carbon nuclei are ^{12}C with no nuclear moment, only hyperfine interactions with more distant B and N nuclei will contribute. The ISC rate due to hyperfine interactions rate is given by the Fermi golden rule $\Gamma_{\rm hf} = (2\pi/\hbar)V_{\rm hf}^2 L(\Delta E)$, where $V_{\rm hf}$ is hyperfine coupling strength, and $L(\Delta E)$ is a lineshape function for the transition $^1A_1 \rightarrow ^3A_1$, identical to the lineshape functions in optical transitions [227] ($\Delta E = 0.81$ eV is the energy difference between the two states, Fig. 5.6 (b)). In Ref. [230] it was estimated that hyperfine coupling of electrons in p_z-type orbitals with B or N nuclei that reside *on the site* where the orbital is localized is on the order of 10^8 s^{-1}. Even if we assume the same coupling constant with more distant nuclei, we obtain rates much lower than 1 s^{-1} showing that ISC due to hyperfine coupling is negligible.

This analysis allows to conclude that $\Gamma_{\rm ISC} \ll \Gamma_{\rm rad}$, and therefore the decay of the excited state $^1A_1$ will be mainly due to radiative decay. This justifies the comparison of the calculated radiative rate with the measured rate of luminescence decay. Since $\Gamma_{\rm ISC} \ll \Gamma_{\rm rad}$, we also conclude that the quantum efficiency of the radiative transition is close to unity.

5.4. Summary and Conclusions

Results show that the calculated optical properties of the C_BC_N defect are in perfect agreement with the known properties of the 4.1 eV line. In fact, carbon dimers *have* been observed by ADF electron microscopy in boron nitride monolayers [105] exfoliated from *bulk* hBN. Carbon atoms have distinct intensity in ADF images, and this allowed for a direct identification of C_BC_N pairs [105]. This experimental proof of the existence of C_BC_N defects in bulk hBN is in excellent agreement with our conclusions regarding the stability of

carbon dimers.

In summary, the author has reported the results of hybrid functional calculations for the C_BC_N dimer in hBN. Those calculations allow us to conclude that C_BC_N is the defect that is responsible for the 4.1 eV emission in hBN. The carbon dimer is expected to form whenever carbon is present during growth, explaining the observed correlation between the presence of carbon and the 4.1 eV line. The calculated zero-phonon line of the intra-defect optical transition of 4.06 eV is close to the experimental value. Moreover, the theoretical Huang-Rhys factor of $S = 1.9$ is consistent with the experimental estimate $S = 1$–2, and radiative lifetime $\tau_{\text{rad}} = 1.2$ ns is close to experimental value $\tau_{\text{rad}} = 1.1$–1.2 ns.

Identification of the chemical nature of the defect will enable more controlled experiments involving the 4.1 eV line, in particular, using the C_BC_N defect as a single photon emitter [103]. Analysis shows that the quantum efficiency of this emitter should be close to unity. Combined with a short radiative lifetime, this results in a very high photon yield. Together with a modest value of the Huang-Rhys factor (large weight of the ZPL) and a well-defined polarization axis, this makes the carbon dimer a very interesting quantum emitter in the near UV.

3 STATEMENT

Ultraviolet single-photon emission in hBN at 4.1 eV was assigned to a carbon dimer defect. The internal optical transition occurs between two localized p_z-type defect states, with a short radiative lifetime. The calculated key parameters for optical transition are in excellent agreement with experimental data.

Conclusions

Thesis employs extensive hybrid DFT calculations to produce accurate results for the characterization of point defects in hexagonal boron nitride, in particular for the observed single-photon emission. By studying a range of hBN native point defects and impurities, the author uncovered dominant defect structures and their physical properties. The conclusions are drawn and presented as follows:

1. Impurities rather than native defects dominate the defect chemistry of hBN. Due to higher formation energies and migration barriers, bare vacancy defects could be present in nonequilibrium conditions only. The common attribution of the 4.1 eV luminescence to C_N defect is ruled out.

2. Quenching of 2 eV single photon emission can be explained through Förster resonant energy transfer from red SPEs to boron vacancy complexes with hydrogen and oxygen. The proposed 2 eV SPE luminescence quenching model can be expanded for two perfectly isolated nitrogen dangling bond systems in hBN.

3. Ultraviolet single-photon emission in hBN at 4.1 eV originates in carbon dimer defect. The internal optical transition occurs between two localized p_z–type defect states, with a short radiative lifetime. The calculated key parameters for optical transition are in excellent agreement with experimental data.

Appendix

Configuration coordinate diagrams for O_N, V_B–O_N, V_B–H

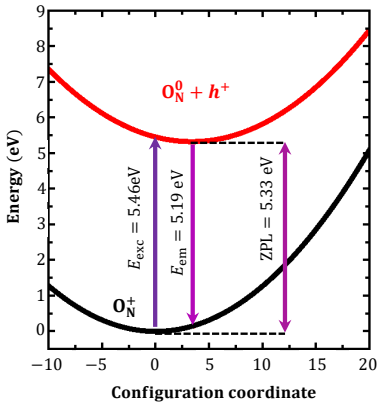

Figure 5.7. Configuration coordinate diagram for inter-defect transition involving O_N defect.

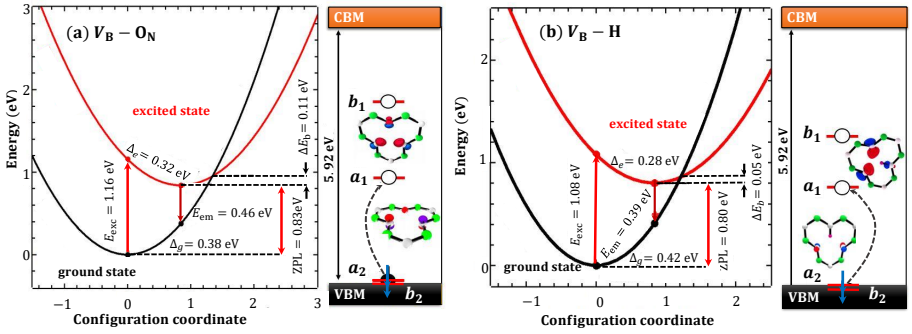

Figure 5.8. Configuration coordinate diagrams for intra-defect transitions involving the neutral boron vacancy complex with (a) oxygen and (b) hydrogen.

Configuration coordinate diagram for inter-defect transition involving the O_N defect, see Fig. 5.7. Huang-Rhys factor of O_N defect is 13.8, thus (+/0) transition will result in a broad featureless emission band centered around 5.19 eV. Configuration coordinate diagrams for intra-defect optical transitions involving the neutral boron vacancy complex with oxygen and hydrogen are shown in Fig. 5.8.

Förster radius in hBN

The critical distance between boron vacancy complexes and SPEs in hBN at which the energy transfer is half-maximal was calculated, see Fig. 5.9.

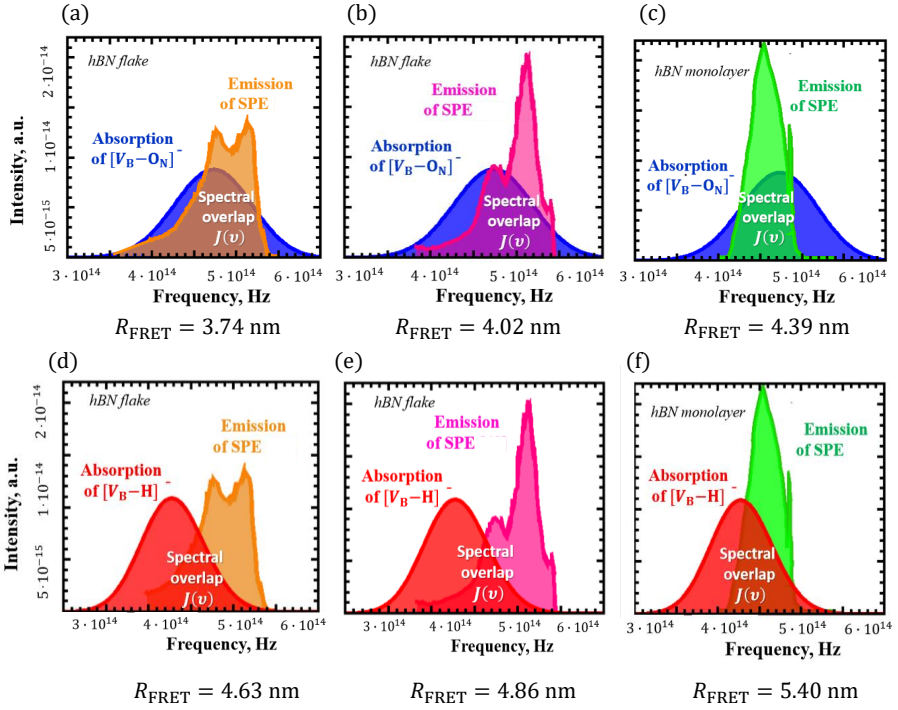

Figure 5.9. (a, b, c) Overlap between absorption of the $[V_B–O_N]-$ complex (DFT, calculated in this Thesis, blue) with emission of the SPE (experimental data adopted from (a, b) [128], (c) [231]). (d, e, f) Overlap between absorption of the $[V_B–H]-$ complex (DFT, calculated in this Thesis, red) with emission of the SPE (experimental data adopted from (d, e) [128], (f) [231]).

Bibliography

[1] I. Aharonovich, D. Englund, M. Toth, Solid-state single-photon emitters, Nature Photonics **10**, 631–641 (2016).

[2] D. Shin, F. Xu, D. Venkatraman, R. Lussana, F. Villa, F. Zappa, V. Goyal, F. Wong, J. Shapiro, Photon-efficient imaging with a single-photon camera, Nature Communications **7**, 12046 (2016).

[3] D. Cohen, R. Nigmatullin, O. Kenneth, F. Jelezko, M. Khodas, A. Retzker, Utilising NV based quantum sensing for velocimetry at the nanoscale, Scientific Reports **10**, 5298 (2020).

[4] J. L. O'Brien, Optical quantum computing, Science **318**, 1567–1570 (2007).

[5] A. Beveratos, R. Brouri, T. Gacoin, A. Villing, J.-P. Poizat, P. Grangier, Single photon quantum cryptography, Physical Review Letters **89**, 187901 (2002).

[6] E. Diamanti, H.-K. Lo, B. Qi, Z. Yuan, Practical challenges in quantum key distribution, npj Quantum Information **2**, 16025 (2016).

[7] Quantum manifesto, available at http://qurope.eu/manifesto .

[8] A. Gruber, A. Dräbenstedt, C. Tietz, F. Ludovic, J. Wrachtrup, C. Borczyskowski, Scanning confocal optical microscopy and magnetic resonance on single defect centers, Science **276**, 2012–2014 (1997).

[9] A. Grosz, M. Haji-Sheikh, S. Mukhopadhyay, *High Sensitivity Magnetometers*, volume 19 (Springer, 2016).

[10] X. Liu, M. Hersam, 2D materials for quantum information science, Nature Reviews Materials **4**, 669–684 (2019).

[11] A. J. Morfa, B. C. Gibson, M. Karg, T. J. Karle, A. D. Greentree, P. Mulvaney, S. Tomljenovic-Hanic, Single-photon emission and quantum characterization of zinc oxide defects, Nano Letters **12**, 949–954 (2012).

[12] A. Lohrmann, B. Johnson, J. Mccallum, S. Castelletto, A review on single photon sources in silicon carbide, Reports on progress in Physics **80**, 034502 (2017).

[13] Y. Zhou, Z. Wang, A. Rasmita, S. Kim, A. Berhane, Z. Bodrog, G. Adamo, A. Gali, I. Aharonovich, W.-B. Gao, Room-temperature solid state quantum emitters in the telecom range, Science Advances **4**, 1–6 (2018).

[14] Y. Xue, H. Wang, N. Xie, Q. Yang, F. Xu, B. Shen, J.-J. Shi, D. Jiang, X. Dou, T. Yu, B.-Q. Sun, Single-photon emission from point defects in aluminum nitride films, The Journal of Physical Chemistry Letters **11**, 2689–2694 (2020).

[15] I. Aharonovich, M. Toth, Quantum emitters in two dimensions, Science **358**, 170–171 (2017).

[16] S. Gupta, J.-H. Yang, B. I. Yakobson, Two-level quantum systems in two-dimensional materials for single photon emission, Nano Letters **19**, 408–414 (2019).

[17] C. Elias, P. Valvin, T. Pelini, A. Summerfield, C. Mellor, T. Cheng, L. Eaves, C. Foxon, P. Beton, S. Novikov, B. Gil, G. Cassabois, Direct band-gap crossover in epitaxial monolayer boron nitride, Nature Communications **10**, 2639 (2019).

[18] G. Cassabois, P. Valvin, B. Gil, Hexagonal boron nitride is an indirect bandgap semiconductor, Nature Photonics **10**, 262 (2016).

[19] C. Dean, A. Young, I. Meric, C. Lee, L. Wang, S. Sorgenfrei, K. Watanabe, T. Taniguchi, P. Kim, K. Shepard, J. Hone, Boron nitride substrates for high-quality graphene electronics, Nature Nanotechnology **5**, 722–6 (2010).

[20] A. K. Geim, I. V. Grigorieva, Van der Waals heterostructures, Nature **499**, 419 (2013).

[21] K. Watanabe, T. Taniguchi, K. Miya, Y. Sato, K. Nakamura, T. Niiyama, M. Taniguchi, Hexagonal boron nitride as a new ultraviolet luminescent material and its application — Fluorescence properties of hBN single-crystal powder, Diamond and Related Materials **20**, 849–852 (2011).

[22] K. Watanabe, T. Taniguchi, H. Kanda, Direct-bandgap properties and evidence for ultraviolet lasing of hexagonal boron nitride single crystal, Nature Materials **3**, 404 (2004).

[23] T. T. Tran, K. Bray, M. J. Ford, M. Toth, I. Aharonovich, Quantum emission from hexagonal boron nitride monolayers, Nature Nanotechnology **11**, 37 (2016).

[24] T. T. Tran, C. Elbadawi, D. Totonjian, C. J. Lobo, G. Grosso, H. Moon, D. R. Englund, M. J. Ford, I. Aharonovich, M. Toth, Robust multicolor single photon emission from point defects in hexagonal boron nitride, ACS Nano **10**, 7331–7338 (2016).

[25] N. R. Jungwirth, B. Calderon, Y. Ji, M. G. Spencer, M. E. Flatté, G. D. Fuchs, Temperature dependence of wavelength selectable zero-phonon emission from single defects in hexagonal boron nitride, Nano Letters **16**, 6052–6057 (2016).

[26] N. Chejanovsky, M. Rezai, F. Paolucci, Y. Kim, T. Rendler, W. Rouabeh, F. Favaro, P. Herlinger, A. Denisenko, S. Yang, I. Gerhardt, A. Finkler, J. Smet, Structural attributes and photodynamics of visible spectrum quantum emitters in hexagonal boron nitride, Nano Letters **16**, 7037–7045 (2016).

[27] L. Martínez, T. Pelini, V. Waselowski, J. Maze, B. Gil, G. Cassabois, V. Jacques, Efficient single photon emission from a high-purity hexagonal boron nitride crystal, Physical Review B **94**, 121405 (2016).

[28] A. L. Exarhos, D. A. Hopper, R. R. Grote, A. Alkauskas, L. C. Bassett, Optical signatures of quantum emitters in suspended hexagonal boron nitride, ACS Nano **11**, 3328–3336 (2017).

[29] M. Kianinia, C. Bradac, B. Sontheimer, F. Wang, T. T. Tran, M. Nguyen, S. Kim, Z.-Q. Xu, D. Jin, A. W. Schell, C. J. Lobo, I. Aharonovich, M. Toth, All-optical control and super-resolution imaging of quantum emitters in layered materials, Nature Communications **9**, 874 (2018).

[30] A. Schell, M. Svedendahl, R. Quidant, Quantum emitters in hexagonal boron nitride have spectrally tunable quantum efficiency, Advanced Materials **30**, 1704237 (2018).

[31] M. Kianinia, B. Regan, S. A. Tawfik, T. T. Tran, M. J. Ford, I. Aharonovich, M. Toth, Robust solid-state quantum system operating at 800 K, ACS Photonics **4**, 768–773 (2017).

[32] A. Gottscholl, M. Kianinia, V. Soltamov, S. Orlinskii, G. Mamin, C. Bradac, C. Kasper, K. Krambrock, A. Sperlich, M. Toth, I. Aharonovich, V. Dyakonov, Initialization and read-out of intrinsic spin defects in a van der Waals crystal at room temperature, Nature Materials **19**, 540–545 (2020).

[33] L. Jaeger, *The second quantum revolution: from entanglement to quantum computing and other super-technologies* (Springer International Publishing, 2019).

[34] H. N. M. Duong, M. A. P. Nguyen, M. Kianinia, T. Ohshima, H. Abe, K. Watanabe, T. Taniguchi, J. H. Edgar, I. Aharonovich, M. Toth, Effects of high-energy electron irradiation on quantum emitters in hexagonal boron nitride, ACS Applied Materials & Interfaces **10**, 24886–24891 (2018).

[35] S. Tawfik, S. Ali, M. Fronzi, M. Kianinia, T. Tran, C. Stampfl, I. Aharonovich, M. Toth, M. Ford, First principles investigation of defect emission from hBN, Nanoscale **9** (2017).

[36] M. Abdi, J.-P. Chou, A. Gali, M. B. Plenio, Color centers in hexagonal boron nitride monolayers: a group theory and ab-initio analysis, ACS Photonics **5**, 1967–1976 (2018).

[37] A. Sajid, J. R. Reimers, M. J. Ford, Defect states in hexagonal boron nitride: Assignments of observed properties and prediction of properties relevant to quantum computation, Physical Review B **97**, 064101 (2018).

[38] F. Wu, A. Galatas, R. Sundararaman, D. Rocca, Y. Ping, First-principles engineering of charged defects for two-dimensional quantum technologies, Physical Review Materials **1**, 071001 (2017).

[39] C. Walle, J. L. Lyons, A. Janotti, Controlling the conductivity of InN, Physica Status Solidi (a) **207**, 1024 – 1036 (2010).

[40] Q. Yan, A. Janotti, M. Scheffler, C. Van de Walle, Origins of optical absorption and emission lines in AlN, Applied Physics Letters **105**, 111104 (2014).

[41] J. L. Lyons, C. G. Van de Walle, Computationally predicted energies and properties of defects in GaN, npj Computational Materials **3**, 12 (2017).

[42] A. Jain, Y. Shin, K. Persson, Computational predictions of energy materials using density functional theory, Nature Review Materials **1**, 15004 (2016).

[43] V. N. Richard, M. Brendan, N. Regina, The top 100 papers, Nature **514**, 550–553 (2014).

[44] L. C. Bassett, A. Alkauskas, A. L. Exarhos, K.-M. C. Fu, Quantum defects by design, Nanophotonics **8**, 211 (2019).

[45] A. Alkauskas, M. Mccluskey, C. Van de Walle, Tutorial: Defects in semiconductors — combining experiment and theory, Journal of Applied Physics **119**, 181101 (2016).

[46] E. Schrödinger, An undulatory theory of the mechanics of atoms and molecules, Physical Review **28**, 1049–1070 (1926).

[47] P. Popelier, *Solving the Schrodinger equation: Has everything been tried?* (Imperial College Press, 2011).

[48] M. Born, R. Oppenheimer, Zur quantentheorie der molekeln, Annalen der Physik **389**, 457–484 (1927).

[49] D. Hartree, The wave mechanics of an atom with a non-Coulomb central field. part 2, Mathematical Proceedings of the Cambridge Philosophical Society (1928).

[50] J. C. Slater, Note on Hartree's method, Physical Review **35**, 210–211 (1930).

[51] P. Hohenberg, W. Kohn, Inhomogeneous electron gas, Physical Review **136**, 864–871 (1964).

[52] K. Burke, Perspective on density functional theory, The Journal of Chemical Physics **136**, 150901 (2012).

[53] E. Bright-Wilson, *DFT explained* (San Francisco, 1968).

[54] V. Sahni, *The Hohenberg-Kohn Theorems and Kohn-Sham Density Functional Theory* (Springer Berlin Heidelberg, 2004).

[55] W. Kohn, L. J. Sham, Self-consistent equations including exchange and correlation effects, Physical Review **140**, 1133–1138 (1965).

[56] S. Sousa, P. Fernandes, M. Ramos, General performance of density functionals, The Journal of Physical Chemistry A **111**, 10439–52 (2007).

[57] D. Rappoport, N. R. M. Crawford, F. Furche, K. Burke, *Approximate Density Functionals: Which Should I Choose?* (American Cancer Society, 2009).

[58] J. P. Perdew, K. Schmidt, Jacob's ladder of density functional approximations for the exchange-correlation energy, in *American Institute of Physics Conference Series* (2001), volume 577 of *American Institute of Physics Conference Series*, 1–20.

[59] J. Perdew, A. Ruzsinszky, J. Tao, V. Staroverov, G. Scuseria, G. Csonka, Prescription for the design and selection of density functional approximations: More constraint satisfaction with fewer fits, The Journal of Chemical Physics **123**, 62201 (2005).

[60] D. M. Ceperley, B. J. Alder, Ground state of the electron gas by a stochastic method, Physical Review Letters **45**, 566–569 (1980).

[61] C. Cramer, *Essentials of Computational Chemistry: Theories and Models* (Wiley, 2005).

[62] J. Heyd, G. E. Scuseria, M. Ernzerhof, Hybrid functionals based on a screened Coulomb potential, Journal of Chemical Physics **118**, 8207–8215 (2003).

[63] J. P. Perdew, K. Burke, M. Ernzerhof, Generalized gradient approximation made simple, Physical Review Letters **77**, 3865 (1996).

[64] M. Marsman, J. Paier, A. Stroppa, G. Kresse, Hybrid functionals applied to extended systems, Journal of Physics: Condensed Matter **20**, 064201 (2008).

[65] J. Paier, M. Marsman, K. Hummer, G. Kresse, I. C. Gerber, J. G. Ángyán, Screened hybrid density functionals applied to solids, The Journal of Chemical Physics **124**, 154709 (2006).

[66] P. Deák, B. Aradi, T. Frauenheim, E. Janzén, A. Gali, Accurate defect levels obtained from the HSE06 range-separated hybrid functional, Physical Review B **81**, 153203 (2010).

[67] C. Guet, *Atomic clusters and nanoparticles: agregats atomiques et nanoparticules* (New York Springer verlag, 2001).

[68] T. Olsen, K. Thygesen, Accurate ground state energies of solids and molecules from Time Dependent Density Functional Theory, Physical Review Letters **112**, 8 (2014).

[69] E. Robert, *Theoretical Modeling of Inorganic Nanostructures* (Springer, 2015).

[70] A. Mendez, D. Mitnik, J. Miraglia, *Advances in Quantum Chemistry*, volume 79 (2019).

[71] E. Bylaska, *Annual Reports in Computational Chemistry* (Elsevier, 2017).

[72] R. M. Martin, *Electronic structure: basic theory and practical methods* (Cambridge University Press, Cambridge, 2004).

[73] P. E. Blöchl, Projector augmented-wave method, Physical Review B **50**, 17953–17979 (1994).

[74] P. Blöchl, J. Kästner, C. Foerst, *Handbook of materials modeling. Volume 1: Methods and models* (Springer, 2005).

[75] J. C. Slater, An augmented plane wave method for the periodic potential problem, Physical Review **92**, 603–608 (1953).

[76] C. Rostgaard, The projector augmented-wave method, arXiv:0910.1921 (2009).

[77] M. Marques, N. Maitra, F. Nogueira, E. Gross, A. Rubio, *Fundamentals of Time-Dependent Density Functional Theory* (Springer-Verlag Berlin Heidelberg, 2012).

[78] G. Kresse, J. Furthmüller, Efficient iterative schemes for ab initio total-energy calculations using a plane-wave basis set, Physical Review B **54**, 11169 (1996).

[79] D. S. Sholl, J. A. Steckel, *Density Functional Theory: A Practical Introduction, DFT Calculations for Simple Solids* (John Wiley Sons, Inc., 2009).

[80] P. Wisesa, K. A. McGill, T. Mueller, Efficient generation of generalized Monkhorst-Pack grids through the use of informatics, Physical Review B **93**, 155109 (2016).

[81] H. J. Monkhorst, J. D. Pack, Special points for Brillouin-zone integrations, Physical Review B **13**, 5188–5192 (1976).

[82] R. M. Nieminen, *Topics in Applied Physics* (Springer Berlin Heidelberg, 2006).

[83] C. Freysoldt, B. Grabowski, T. Hickel, J. Neugebauer, G. Kresse, A. Janotti, C. G. Van de Walle, First-principles calculations for point defects in solids, Reviews of Modern Physics **86**, 253 (2014).

[84] M. J. Buerger, Derivative crystal structures, The Journal of Chemical Physics **15**, 1–16 (1947).

[85] C. Freysoldt, B. Grabowski, T. Hickel, J. Neugebauer, G. Kresse, A. Janotti, C. G. Van de Walle, First-principles calculations for point defects in solids, Reviews of Modern Physics **86**, 253–305.

[86] C. Dreyer, A. Alkauskas, J. L. Lyons, A. Janotti, C. Van de Walle, First-principles calculations of point defects for quantum technologies, Annual Review of Materials Research **48**, 124453 (2018).

[87] M. Leifgen, T. Schröder, F. Gädeke, R. Riemann, V. Métillon, E. Neu, C. Hepp, C. Arend, C. Becher, K. Lauritsen, O. Benson, Evaluation of nitrogen- and silicon-vacancy defect centres as single photon sources in quantum key distribution, New Journal of Physics **16**, 023021 (2014).

[88] H. Wang, Y.-M. He, T.-H. Chung, H. Hu, Y. Yu, S. Chen, X. Ding, M.-C. Chen, J. Qin, X. Yang, R.-Z. Liu, Z.-C. Duan, J.-P. Li, S. Gerhardt, K. Winkler, J. Jurkat, L.-J. Wang, N. Gregersen, Y.-H. Huo, J.-W. Pan, Towards optimal single-photon sources from polarized microcavities, Nature Photonics **13**, 770–775 (2019).

[89] H. J. Kimble, M. Dagenais, L. Mandel, Photon antibunching in resonance fluorescence, Physical Review Letters **39**, 691–695 (1977).

[90] R. Hanbury Brown, R. Twiss, A test of a new type of stellar interferometer on Sirius, Nature **178**, 1046–1048 (1956).

[91] L. Tizei, M. Kociak, *Quantum Nanooptics in the Electron Microscope* (Elsevier, 2017).

[92] M. Fox, *Quantum Optics: An Introduction*, Oxford Master Series in Physics (OUP Oxford, 2006).

[93] R. Loudon, *The Quantum Theory of Light* (Oxford University Press, 2000).

[94] M. Berthel, O. Mollet, G. Dantelle, T. Gacoin, S. Huant, A. Drezet, Photophysics of single nitrogen-vacancy centers in diamond nanocrystals, Physical Review B **91**, 035308 (2015).

[95] I. Aharonovich, S. Castelletto, D. Simpson, C.-H. Su, A. Greentree, S. Prawer, Diamond-based single-photon emitters, Reports on Progress in Physics **74**, 076501 (2011).

[96] I. Aharonovich, S. Castelletto, D. Simpson, A. Greentree, S. Prawer, Photophysics of novel diamond based single photon emitters, Physical Review A **81**, 043813 (2010).

[97] A. Beveratos, R. Brouri, J.-P. Poizat, P. Grangier, *Quantum Communication, Computing, and Measurement 3, Bunching and Antibunching from Single NV Color Centers in Diamond* (Kluwer Academic, 2000).

[98] K. Fox, S. Prawer, *Quantum Information Processing with Diamond* (Elsevier, 2014).

[99] N. V. Proscia, Z. Shotan, H. Jayakumar, P. Reddy, C. Cohen, M. Dollar, A. Alkauskas, M. Doherty, C. A. Meriles, V. M. Menon, Near-deterministic activation of room-temperature quantum emitters in hexagonal boron nitride, Optica **5**, 1128–1134 (2018).

[100] C. Blum, F. Schleifenbaum, M. Stopel, S. Peter, M. Sackrow, V. Subramaniam, A. Meixner, Room temperature excitation spectroscopy of single quantum dots, Beilstein Journal of Nanotechnology **2**, 516–24 (2011).

[101] S. Häußler, G. Thiering, A. Dietrich, N. Waasem, T. Teraji, J. Isoya, T. Iwasaki, M. Hatano, F. Jelezko, A. Gali, A. Kubanek, Photoluminescence excitation spectroscopy of SiV- and GeV-color center in diamond, New Journal of Physics **19**, 10 (2017).

[102] M. Kociak, O. Stéphan, A. Gloter, L. Zagonel, L. Tizei, M. Tencé, K. March, J. Blazit, Z. Mahfoud, A. Losquin, S. Meuret, C. Colliex, Seeing and measuring in colours: Electron microscopy and spectroscopies applied to nano-optics, Comptes Rendus Physique **15**, 5022 (2014).

[103] R. Bourrellier, S. Meuret, A. Tararan, O. Stéphan, M. Kociak, L. H. Tizei, A. Zobelli, Bright UV single photon emission at point defects in hBN, Nano Letters **16**, 4317–4321 (2016).

[104] A. Crewe, J. Wall, J. Langmore, Visibility of single atoms, Science **168**, 1338–40 (1970).

[105] O. L. Krivanek, M. F. Chisholm, V. Nicolosi, T. J. Pennycook, G. J. Corbin, N. Dellby, M. F. Murfitt, C. S. Own, Z. S. Szilagyi, M. P. Oxley, S. T. Pantelides, S. J. Pennycook, Atom-by-atom structural and chemical analysis by annular dark-field electron microscopy, Nature **464**, 571 (2010).

[106] L. Museur, A. Kanaev, Photoluminescence properties of pyrolytic boron nitride, Journal of Materials Science **44**, 2560 (2009).

[107] H. J. Kimble, M. Dagenais, L. Mandel, Photon antibunching in resonance fluorescence, Physical Review Letters **39**, 691–695 (1977).

[108] D. Higginbottom, L. Slodička, G. Araneda, L. Lachman, R. Filip, M. Hennrich, R. Blatt, Pure single photons from a trapped atom source, New Journal of Physics **18**, 93038 (2016).

[109] B. Lounis, M. Orrit, Single-photon sources, Reports on Progress in Physics **68**, 1129 (2005).

[110] D. C. Burnham, D. L. Weinberg, Observation of simultaneity in parametric production of optical photon pairs, Physical Review Letters **25**, 84–87 (1970).

[111] J. Schneeloch, S. H. Knarr, D. F. Bogorin, M. L. Levangie, C. C. Tison, R. Frank, G. A. Howland, M. L. Fanto, P. M. Alsing, Introduction to the absolute brightness and number statistics in spontaneous parametric down-conversion, Journal of Optics **21**, 043501 (2019).

[112] G. Rainò, G. Nedelcu, L. Protesescu, M. I. Bodnarchuk, M. V. Kovalenko, R. F. Mahrt, T. Stöferle, Single cesium lead halide perovskite nanocrystals at low temperature: Fast single-photon emission, reduced blinking, and exciton fine structure, ACS Nano **10**, 2485—2490 (2016).

[113] S. Pazzagli, P. Lombardi, D. Martella, M. Colautti, B. Tiribilli, F. S. Cataliotti, C. Toninelli, Self-assembled nanocrystals of polycyclic aromatic hydrocarbons show photostable single-photon emission, ACS Nano **12**, 4295–4303 (2018).

[114] P. Michler, A. Kiraz, C. Becher, W. Schoenfeld, P. Petroff, L. Zhang, E. Hu, A. Imamoglu, A quantum dot single-photon turnstile device, Science **290**, 2282–5 (2001).

[115] P. Senellart, G. Solomon, A. White, High-performance semiconductor quantum-dot single-photon sources, Nature Nanotechnology **12**, 1026–1039 (2017).

[116] S. Buckley, K. Rivoire, J. Vuckovic, Engineered quantum dot single-photon sources, Reports on Progress in Physics **75**, 126503 (2012).

[117] M. Dybiec, G. Chornokur, S. Ostapenko, A. Wolcott, J. Zhang, A. Zajac, C. Phelan, T. Sellers, D. Gerion, Photoluminescence spectroscopy of bioconjugated CdSe/ZnS quantum dots, Applied Physics Letters **90**, 263112 (2007).

[118] M. Reimer, C. Cher, The quest for a perfect single-photon source, Nature Photonics **13**, 734–736 (2019).

[119] A. M. Zaitsev, Vibronic spectra of impurity-related optical centers in diamond, Physical Review B **61**, 12909–12922 (2000).

[120] A. Zaitsev, *Optical Properties of Diamond* (Springer, 2001).

[121] A. Saha, B. Gifford, X. He, G. Ao, M. Zheng, H. Kataura, H. Htoon, S. Kilina, S. Tretiak, S. Doorn, Narrow-band single-photon emission through selective aryl functionalization of zigzag carbon nanotubes, Nature Chemistry **10**, 1089–1095 (2018).

[122] J. Klein, M. Lorke, M. Florian, F. Sigger, L. Sigl, S. Rey, J. Wierzbowski, J. Cerne, K. Müller, E. Mitterreiter, P. Zimmermann, T. Taniguchi, K. Watanabe, U. Wurstbauer, M. Kaniber, M. Knap, R. Schmidt, J. Finley, A. Holleitner, Site-selectively generated photon emitters in monolayer MoS2 via local helium ion irradiation, Nature Communications **10**, 2755 (2019).

[123] A. Dietrich, M. Bürk, E. S. Steiger, L. Antoniuk, T. T. Tran, M. Nguyen, I. Aharonovich, F. Jelezko, A. Kubanek, Observation of fourier transform limited lines in hexagonal boron nitride, Physical Review B **98**, 081414 (2018).

[124] G. Grosso, H. Moon, B. Lienhard, S. Ali, K. Efetov, M. Furchi, P. Jarillo-Herrero, M. Ford, I. Aharonovich, D. Englund, Tunable and high purity room-temperature single photon emission from atomic defects in hexagonal boron nitride, Nature Communications **8**, 705 (2017).

[125] N. Nikolay, N. Mendelson, E. Özelci, B. Sontheimer, F. Böhm, G. Kewes, M. Toth, I. Aharonovich, O. Benson, Direct measurement of quantum efficiency of single-photon emitters in hexagonal boron nitride, Optica **6**, 1084 (2019).

[126] R. J. Chang, X. Wang, S. Wang, Y. Sheng, B. Porter, H. Bhaskaran, J. H. Warner, Growth of large single-crystalline monolayer hexagonal boron nitride by oxide-assisted chemical vapor deposition, Chemistry of Materials **29**, 6252–6260 (2017).

[127] S. Kim, J. Fröch, J. Christian, M. Straw, J. Bishop, D. Totonjian, K. Watanabe, T. Taniguchi, M. Toth, I. Aharonovich, Photonic crystal cavities from hexagonal boron nitride, Nature Communications **9**, 2623 (2018).

[128] S. Choi, T. T. Tran, C. Elbadawi, C. Lobo, X. Wang, S. Juodkazis, G. Seniutinas, M. Toth, I. Aharonovich, Engineering and localization of quantum emitters in large hexagonal boron nitride layers, ACS Applied Materials & Interfaces **8**, 29642–29648 (2016).

[129] J. Ahn, Z. Xu, J. Bang, A. Llacsahuanga Allcca, Y. Chen, T. Li, Stable emission and fast optical modulation of quantum emitters in boron nitride nanotubes, Optics Letters **43**, 3778–3781 (2018).

[130] J. Ziegler, A. Blaikie, A. Fathalizadeh, D. Miller, F. S. Yasin, K. Williams, J. Mohrhardt, B. J. McMorran, A. Zettl, B. Alemán, Single-photon emitters in boron nitride nanococoons, Nano Letters **18**, 2683–2688 (2018).

[131] N. V. Proscia, Z. Shotan, H. Jayakumar, P. Reddy, C. Cohen, M. Dollar, A. Alkauskas, M. Doherty, C. A. Meriles, V. M. Menon, Near-deterministic activation of room-temperature quantum emitters in hexagonal boron nitride, Optica **5**, 1128–1134 (2018).

[132] J. Ziegler, R. Klaiss, A. Blaikie, D. Miller, V. R. Horowitz, B. J. Alemán, Deterministic quantum emitter formation in hexagonal boron nitride via controlled edge creation, Nano Letters **19**, 2121–2127 (2019).

[133] Z.-Q. Xu, C. Elbadawi, T. T. Tran, M. Kianinia, X. Li, D. Liu, T. B. Hoffman, M. Nguyen, S. Kim, J. H. Edgar, X. Wu, L. Song, S. Ali, M. Ford, M. Toth, I. Aharonovich, Single photon emission from plasma treated 2D hexagonal boron nitride, Nanoscale **10**, 7957–7965 (2018).

[134] N. Mendelson, D. Chugh, T. Cheng, A. Gottscholl, H. Long, C. Mellor, A. Zettl, V. Dyakonov, P. Beton, S. Novikov, C. Jagadish, H. Tan, M. Toth, C. Bradac, I. Aharonovich, Identifying carbon as the source of visible single photon emission from hexagonal boron nitride, arXiv:2003.00949 (2020).

[135] M. E. Turiansky, A. Alkauskas, L. C. Bassett, C. G. Van de Walle, Dangling bonds in hexagonal boron nitride as single-photon emitters, Physical Review Letters **123**, 127401 (2019).

[136] N. Mendelson, Z.-Q. Xu, T. T. Tran, M. Kianinia, J. Scott, C. Bradac, I. Aharonovich, M. Toth, Engineering and tuning of quantum emitters in few-layer hexagonal boron nitride, ACS Nano **13**, 3132–3140 (2019).

[137] L. Hoddeson, E. Braun, J. Teichmann, S. Weart, Z. Wang, Out of the crystal maze: Chapters from the history of solid-state physics, American Journal of Physics **61**, 121 (1993).

[138] L. Li, Y. Chen, Atomically thin boron nitride: Unique properties and applications, Advanced Functional Materials **26**, 2594–2608 (2016).

[139] K. K. Kim, A. Hsu, X. Jia, S. M. Kim, Y. Shi, M. Hofmann, D. Nezich, J. F. Rodriguez-Nieva, M. Dresselhaus, T. Palacios, J. Kong, Synthesis of monolayer hexagonal boron nitride on Cu foil using chemical vapor deposition, Nano Letters **12**, 161–166 (2011).

[140] Y. Shi, C. Hamsen, X. Jia, K. K. Kim, A. Reina, M. Hofmann, A. L. Hsu, K. Zhang, H. Li, Z.-Y. Juang, et al., Synthesis of few-layer hexagonal boron nitride thin film by chemical vapor deposition, Nano letters **10**, 4134–4139 (2010).

[141] L. Song, L. Ci, H. Lu, P. B. Sorokin, C. Jin, J. Ni, A. G. Kvashnin, D. G. Kvashnin, J. Lou, B. I. Yakobson, et al., Large scale growth and characterization of atomic hexagonal boron nitride layers, Nano letters **10**, 3209–3215 (2010).

[142] M. Šiškins, C. Mullan, S.-K. Son, J. Yin, K. Watanabe, T. Taniguchi, D. Ghazaryan, K. Novoselov, A. Mishchenko, High-temperature electronic devices enabled by hBN-encapsulated graphene, Applied Physics Letters **114**, 123104 (2019).

[143] K. Watanabe, T. Taniguchi, T. Niiyama, K. Miya, M. Taniguchi, Far-ultraviolet plane-emission handheld device based on hexagonal boron nitride, Nature photonics **3**, 591 (2009).

[144] A. Lukomskii, V. Shipilo, L. Gameza, Luminescence properties of graphite-like boron nitride, Journal of Applied Spectroscopy **57**, 607–610 (1992).

[145] H. Morkoç, *Handbook of Nitride Semiconductors and Devices: Electronic and Optical Processes in Nitrides, Volume 2* (Wiley-VCH Verlag GmbH, 2008).

[146] B. He, W. Zhang, Y. Zhiqiang, Y. Chong, Y. Yang, Q. Ye, X. Pan, J. A. Zapien, I. Bello, S. Lee, I. Gerhards, H. Zutz, H. Hofsäss, P-type conduction in beryllium-implanted hexagonal boron nitride films, Applied Physics Letters **95**, 252106 (2009).

[147] R. Dahal, J. Li, S. Majety, B. Pantha, X. Cao, J.-Y. Lin, H. Jiang, Epitaxially grown semiconducting hexagonal boron nitride as a deep ultraviolet photonic material, Applied Physics Letters **98**, 211110 (2011).

[148] L. Weston, D. Wickramaratne, C. Van de Walle, Hole polarons and p-type doping in boron nitride polymorphs, Physical Review B **96**, 100102 (2017).

[149] M. Reshchikov, H. Morkoç, Luminescence properties of defects in GaN, Journal of Applied Physics **97**, 061301 (2005).

[150] T. T. Tran, C. Zachreson, A. M. Berhane, K. Bray, R. G. Sandstrom, L. H. Li, T. Taniguchi, K. Watanabe, I. Aharonovich, M. Toth, Quantum emission from defects in single-crystalline hexagonal boron nitride, Physical Review Applied **5**, 034005 (2016).

[151] A. Katzir, J. Suss, A. Zunger, A. Halperin, Point defects in hexagonal boron nitride. I. EPR, thermoluminescence, and thermally-stimulated-current measurements, Physical Review B **11**, 2370 (1975).

[152] M. G. Silly, P. Jaffrennou, J. Barjon, J.-S. Lauret, F. Ducastelle, A. Loiseau, E. Obraztsova, B. Attal-Tretout, E. Rosencher, Luminescence properties of hexagonal boron nitride: Cathodoluminescence and photoluminescence spectroscopy measurements, Physical Review B **75**, 085205 (2007).

[153] L. Museur, D. Anglos, J.-P. Petitet, J.-P. Michel, A. V. Kanaev, Photoluminescence of hexagonal boron nitride: effect of surface oxidation under UV-laser irradiation, Journal of Luminescence **127**, 595–600 (2007).

[154] X. Du, J. Li, J. Lin, H. Jiang, The origin of deep-level impurity transitions in hexagonal boron nitride, Applied Physics Letters **106**, 021110 (2015).

[155] T. Q. P. Vuong, G. Cassabois, P. Valvin, A. Ouerghi, Y. Chassagneux, C. Voisin, B. Gil, Phonon-photon mapping in a color center in hexagonal boron nitride, Physical Review Letters **117**, 097402 (2016).

[156] A. Zunger, A. Katzir, Point defects in hexagonal boron nitride. ii. Theoretical studies, Physical review B **11**, 2378 (1975).

[157] W. Orellana, H. Chacham, Stability of native defects in hexagonal and cubic boron nitride, Physical Review B **63**, 125205 (2001).

[158] S. Azevedo, J. Kaschny, C. de Castilho, F. Mota, Theoretical investigation of native defects in a boron nitride monolayer, Nanotechnology **23**, 17055–17061 (2012).

[159] B. Huang, H. Lee, Defect and impurity properties of hexagonal boron nitride: A first-principles calculation, Physical Review B **86**, 245406 (2012).

[160] G. Cheng, Y. Zhang, L. Yan, H. Huang, Q. Huang, Y. Song, Y. Chen, Z. Tang, A paramagnetic neutral CBVN center in hexagonal boron nitride monolayer for spin qubit application, Computational Materials Science **129**, 247–251 (2017).

[161] J. Heyd, G. E. Scuseria, M. Ernzerhof, Erratum: Hybrid functionals based on a screened Coulomb potential, The Journal of Chemical Physics **124**, 219906 (2006).

[162] P. Moses, M. Miao, Q. Yan, C. Van de Walle, Hybrid functional investigations of band gaps and band alignments for AlN, GaN, InN, and InGaN, The Journal of Chemical Physics **134**, 084703 (2011).

[163] A. Grimme, E. Krieg, A consistent and accurate ab-initio parametrization of density functional dispersion correction (DFT-D) for the 94 elements H-Pu, The Journal of Chemical Physics **132**, 154104 (2010).

[164] P. E. Blöchl, Projector augmented-wave method, Physical Review B **50**, 17953 (1994).

[165] G. Kresse, J. Furthmüller, Efficient iterative schemes for ab initio total-energy calculations using a plane-wave basis set, Physical Review B **54**, 11169–11186 (1996).

[166] C. G. Van de Walle, J. Neugebauer, First-principles calculations for defects and impurities: Applications to III-nitrides, Journal of Applied Physics **95**, 3851–3879 (2004).

[167] C. Freysoldt, J. Neugebauer, C. G. Van de Walle, Fully ab-initio finite-size corrections for charged-defect supercell calculations, Physical Review Letters **102**, 016402 (2009).

[168] C. Freysoldt, J. Neugebauer, C. Walle, Electrostatic interactions between charged defects in supercells, Physica Status Solidi B **248**, 1067–1076 (2011).

[169] I. Tomaszkiewicz, The enthalphy of formation of hexagonal boron nitride, Polish Journal of Chemistry **76**, 891 (2002).

[170] H.-P. Komsa, T. T. Rantala, A. Pasquarello, Finite-size supercell correction schemes for charged defect calculations, Physical Review B **86**, 045112 (2012).

[171] Y. Gu, M. Zheng, Y. Liu, Z. Xu, Low-temperature synthesis and growth of hexagonal boron-nitride in a lithium bromide melt, Journal of the American Ceramic Society **90**, 1589–1591 (2007).

[172] L. Museur, G. Brasse, A. Pierret, S. Maine, A. Attal Tretout, F. Ducastelle, A. Loiseau, J. Barjon, K. Watanabe, T. Taniguchi, A. Kanaev, Exciton optical transitions in a hexagonal boron nitride single crystal, Physica Status Solidi Rapid Research Letter **5**, 214–216 (2011).

[173] D. Wickramaratne, L. Weston, C. G. Van de Walle, Monolayer to bulk properties of hexagonal boron nitride, The Journal of Physical Chemistry C **122**, 25524–25529 (2018).

[174] B. Arnaud, S. Lebègue, P. Rabiller, M. Alouani, Huge excitonic effects in layered hexagonal boron nitride, Physical Review Letters **96**, 026402 (2006).

[175] Y. Band, Y. Avishai, *Quantum Mechanics with Applications to Nanotechnology and Information Science* (Academic Press, 2013).

[176] C. Attaccalite, M. Bockstedte, A. Marini, A. Rubio, L. Wirtz, Coupling of excitons and defect states in boron-nitride nanostructures, Physical Review B **83**, 144115 (2011).

[177] B. Janesko, T. Henderson, G. Scuseria, Screened hybrid density functionals for solid-state chemistry and physics, Physical Chemistry Chemical Physics **11**, 443–54 (2009).

[178] A. Zobelli, C. P. Ewels, A. Gloter, G. Seifert, Vacancy migration in hexagonal boron nitride, Physical Review B **75**, 094104 (2007).

[179] G. H. Vineyard, Frequency factors and isotope effects in solid state rate processes, Journal of Physics and Chemistry of Solids **3**, 121–127 (1957).

[180] R. Geick, C. H. Perry, G. Rupprecht, Normal modes in hexagonal boron nitride, Physical Review **146**, 543–547 (1966).

[181] A. Janotti, C. G. Van de Walle, Native point defects in ZnO, Physical Review B **76**, 165202 (2007).

[182] B. Uberuaga, H. Jonsson, A climbing image nudged elastic band method for finding saddle points and minimum energy paths, The Journal of Chemical Physics **113**, 9901–9904 (2000).

[183] G. Henkelman, H. Jónsson, Improved tangent estimate in the nudged elastic band method for finding minimum energy paths and saddle points, The Journal of Chemical Physics **113**, 9978 (2000).

[184] C. Jin, F. Lin, K. Suenaga, S. Iijima, Fabrication of a freestanding boron nitride single layer and its defect assignments, Physical Review Letters **102**, 195505 (2009).

[185] L.-C. Yin, H.-M. Cheng, R. Saito, Triangle defect states of hexagonal boron nitride atomic layer: Density functional theory calculations, Physical Review B **81**, 153407 (2010).

[186] J. Kotakoski, O. Lehtinen, C. Jin, K. Suenaga, A. Krasheninnikov, Electron knock-on damage in hexagonal boron nitride monolayers, Physical Review B **82**, 113404 (2010).

[187] N. Alem, R. Erni, C. Kisielowski, M. Rossell, W. Gannett, A. Zettl, Atomically thin hexagonal boron nitride probed by ultrahigh-resolution transmission electron microscopy, Physical Review B **80**, 155425 (2009).

[188] A. Krasheninnikov, P. Lehtinen, A. Foster, R. Nieminen, Bending the rules: Contrasting vacancy energetics and migration in graphite and carbon nanotubes, Chemical Physics Letters **418**, 132–136 (2006).

[189] L. Gordon, J. L. Lyons, A. Janotti, C. G. Van de Walle, Hybrid functional calculations of DX centers in AlN and GaN, Physical Review B **89**, 085204 (2014).

[190] J. L. Lyons, A. Janotti, C. G. Van de Walle, Effects of carbon on the electrical and optical properties of InN, GaN, and AlN, Physical Review B **89**, 035204 (2014).

[191] M. Straßburg, J. Senawiratne, N. Dietz, U. Haboeck, A. Hoffmann, V. Noveski, R. Dalmau, R. Schlesser, Z. Sitar, The growth and optical properties of large, high-quality AlN single crystals, Journal of Applied Physics **96**, 5870–5876 (2004).

[192] A. Ishibashi, H. Takeishi, M. Mannoh, Y. Yabuuchi, Y. Ban, Residual impurities in GaN/Al2O3 grown by metalorganic vapor phase epitaxy, Journal of Electronic Materials **25**, 799 (1996).

[193] T. Taniguchi, K. Watanabe, Synthesis of high-purity boron nitride single crystals under high pressure by using Ba-BN solvent, Journal of Crystal Growth **303**, 525–529 (2007).

[194] R. Peter, I. Kavre Piltaver, L. Li, Y. Chen, L.-J. Fan, Y.-W. Yang, Decoration of nitrogen vacancies by oxygen atoms in boron nitride nanotubes, Physical Chemistry Chemical Physics **12**, 15349–53 (2010).

[195] C. G. Van de Walle, J. Neugebauer, Hydrogen in semiconductors, Annual Review of Materials Research **36**, 179–198 (2006).

[196] C. Dreyer, J. L. Lyons, A. Janotti, C. Van de Walle, Band alignments and polarization properties of BN polymorphs, Applied Physics Express **7**, 031001 (2014).

[197] C. G. Van de Walle, Interactions of hydrogen with native defects in GaN, Physical Review B **56**, 10020–10023 (1997).

[198] L. Museur, E. Feldbach, A. Kanaev, Defect-related photoluminescence of hexagonal boron nitride, Physical Review B **78**, 155204 (2008).

[199] G. Cassabois, P. Valvin, B. Gil, Intervalley scattering in hexagonal boron nitride, Physical Review B **93**, 035207 (2016).

[200] X. Du, M. R. Uddin, J. Li, J.-Y. Lin, H. Jiang, Layer number dependent optical properties of multilayer hexagonal BN epilayers, Applied Physics Letters **110**, 092102 (2017).

[201] N. R. Jungwirth, G. D. Fuchs, Optical absorption and emission mechanisms of single defects in hexagonal boron nitride, Physical Review Letters **119**, 057401 (2017).

[202] N. L. McDougall, J. G. Partridge, R. J. Nicholls, S. P. Russo, D. G. McCulloch, Influence of point defects on the near edge structure of hexagonal boron nitride, Physical Review B **96**, 144106 (2017).

[203] A. M. Stoneham, *Theory of Defects in Solids: Electronic Structure of Defects in Insulators and Semiconductors* (Oxford University Press, 1975).

[204] K. Huang, A. Rhys, *Proceedings of the Royal Society A: Theory of light absorption and non-radiative transitions in F-centres*, volume 204 (The Royal Society, 1950).

[205] R. O. Jones, O. Gunnarsson, The density functional formalism, its applications and prospects, Reviews of Modern Physics **61**, 689 (1989).

[206] J. F. Janak, Proof that $\frac{\partial e}{\partial n_i} = \epsilon$ in density-functional theory, Physical Review B **18**, 7165–7168 (1978).

[207] J. C. Slater, J. C. Phillips, Quantum theory of molecules and solids Vol. 4: The self-consistent field for molecules and solids, Physics Today **27**, 49 (1974).

[208] V. Ivady, I. Abrikosov, A. Gali, First principles calculation of spin-related quantities for point defect qubit research, npj Computational Materials **4**, 76 (2018).

[209] A. Alkauskas, P. Deak, J. Neugebauer, A. Pasquarello, C. Walle, *Advanced Calculations for Defects in Materials: Electronic Structure Methods* (Wiley Verlag GmbH, 2011).

[210] A. Alkauskas, C. E. Dreyer, J. L. Lyons, C. G. Van de Walle, Role of excited states in Shockley-Read-Hall recombination in wide-band-gap semiconductors, Physical Review B **93**, 201304 (2016).

[211] A. Alkauskas, M. D. McCluskey, C. G. Van de Walle, Tutorial: Defects in semiconductors — combining experiment and theory, Journal of Applied Physics **119**, 181101 (2016).

[212] G. Cappellini, G. Satta, M. Palummo, G. Onida, Optical properties of BN in cubic and layered hexagonal phases, Physical Review B **64**, 035104 (2001).

[213] T.-L. Wee, Y.-K. Tzeng, C.-C. Han, H.-C. Chang, W. Fann, J.-H. Hsu, K.-M. Chen, Y.-C. Yu, Two-photon excited fluorescence of nitrogen-vacancy centers in proton-irradiated type Ib diamond, The Journal of Physical Chemistry A **111**, 9379–9386 (2007).

[214] J. Tisler, R. Reuter, A. Lämmle, F. Jelezko, G. Balasubramanian, P. R. Hemmer, F. Reinhard, J. Wrachtrup, Highly efficient FRET from a single nitrogen-vacancy center in nanodiamonds to a single organic molecule, ACS Nano **5**, 7893–7898 (2011).

[215] Y.-T. Wang, W. Liu, Z.-P. Li, S. Yu, K. Zhijin, Y. Meng, J.-S. Tang, C.-F. Li, G.-C. Guo, A bubble-induced ultrastable and robust single-photon emitter in hexagonal boron nitride, arXiv:1906.00493 (2019).

[216] T. Korona, M. Chojecki, Exploring point defects in hexagonal boron-nitrogen monolayers, International Journal of Quantum Chemistry **119**, 25925 (2019).

[217] S. Larach, R. E. Shrader, Multiband luminescence in boron nitride, Physical Review **104**, 68 (1956).

[218] V. Solozhenko, A. Lazarenko, J.-P. Petitet, A. Kanaev, Bandgap energy of graphite-like hexagonal boron nitride, Journal of Physics and Chemistry of Solids **62**, 1331–1334 (2001).

[219] K. Era, F. Minami, T. Kuzuba, Fast luminescence from carbon-related defects of hexagonal boron nitride, Journal of Luminescence **24**, 71–74 (1981).

[220] A. Vokhmintsev, I. Weinstein, D. Zamyatin, Electron-phonon interactions in subband excited photoluminescence of hexagonal boron nitride, Journal of Luminescence **208**, 363–370 (2019).

[221] S. Meuret, L. H. G. Tizei, T. Cazimajou, R. Bourrellier, H. C. Chang, F. Treussart, M. Kociak, Photon bunching in cathodoluminescence, Physical Review Letters **114**, 197401 (2015).

[222] M. R. Uddin, J. Li, J. Y. Lin, H. X. Jiang, Probing carbon impurities in hexagonal boron nitride epilayers, Applied Physics Letters **110**, 182107 (2017).

[223] T. Ziegler, A. Rauk, E. Baerends, On the calculation of multiplet energies by the Hartree-Fock-Slater method, Theoretical Chemistry Accounts **43**, 261–271 (1977).

[224] U. von Barth, Local-density theory of multiplet structure, Physical Review A **20**, 1693–1703 (1979).

[225] M. Lannoo, G. A. Baraff, M. Schlüter, Self-consistent second-order perturbation treatment of multiplet structures using local-density theory, Physical Review B **24**, 943–954 (1981).

[226] H. Ehrenreich, D. Turnbull, F. Seitz, *Solid State Physics*, volume 38 (Academic Press, 1984).

[227] A. Alkauskas, J. L. Lyons, D. Steiauf, C. G. Van de Walle, First-principles calculations of luminescence spectrum line shapes for defects in semiconductors: the example of GaN and ZnO, Physical Review Letters **109**, 267401 (2012).

[228] T. J. Penfold, E. Gindensperger, C. Daniel, C. M. Marian, Spin-vibronic mechanism for intersystem crossing, Chemical Reviews **118**, 6975–7025 (2018).

[229] M. Tinkham, *Group theory and quantum mechanics* (Dover, 2003).

[230] A. L. Exarhos, D. A. Hopper, R. N. Patel, M. W. Doherty, L. C. Bassett, Magnetic-field-dependent quantum emission in hexagonal boron nitride at room temperature, Nature Communications **10**, 222 (2019).

[231] J. Feng, H. Deschout, S. Caneva, S. Hofmann, I. Lončarić, P. Lazić, A. Radenovic, Imaging of optically active defects with nanometer resolution, Nano Letters **18**, 1739–1744 (2018).

Notes

Notes

Vilnius University Press
Saulėtekio al. 9, LT-10222 Vilnius
e-mail: info@leidykla.vu.lt,
www.leidykla.vu.lt
Print run copies 25